

NAVAL POSTGRADUATE SCHOOL MONTEREY, CALIFORNIA



THESIS

**POWER RECOVERY OF RADIATION DAMAGED MOCVD
GROWN INDIUM PHOSPHIDE ON SILICON SOLAR
CELLS THROUGH ARGON-ION LASER ANNEALING**

by

Lynn L. Boyer IV

June , 1996

Thesis Advisor:

Sherif Michael

Approved for public release; distribution unlimited.

Thesis
B7933

DUDLEY KNOX LIBRARY
NAVAL POSTGRADUATE SCHOOL
MONTEREY CA 93943-5101

REPORT DOCUMENTATION PAGE

Form Approved OMB No. 0704-0188

Public reporting burden for this collection of information is estimated to average 1 hour per response, including the time for reviewing instruction, searching existing data sources, gathering and maintaining the data needed, and completing and reviewing the collection of information. Send comments regarding this burden estimate or any other aspect of this collection of information, including suggestions for reducing this burden, to Washington Headquarters Services, Directorate for Information Operations and Reports, 1215 Jefferson Davis Highway, Suite 1204, Arlington, VA 22202-4302, and to the Office of Management and Budget, Paperwork Reduction Project (0704-0188) Washington DC 20503.

1. AGENCY USE ONLY (Leave blank)	2. REPORT DATE June 1996	3. REPORT TYPE AND DATES COVERED Master's Thesis	
4. TITLE AND SUBTITLE: POWER RECOVERY OF RADIATION DAMAGED MOCVD GROWN INDIUM PHOSPHIDE ON SILICON SOLAR CELLS THROUGH ARGON-ION LASER ANNEALING		5. FUNDING NUMBERS	
6. AUTHOR(S) Boyer IV, Lynn L.			
7. PERFORMING ORGANIZATION NAME(S) AND ADDRESS(ES) Naval Postgraduate School Monterey CA 93943-5000		8. PERFORMING ORGANIZATION REPORT NUMBER	
9. SPONSORING/MONITORING AGENCY NAME(S) AND ADDRESS(ES)		10. SPONSORING/MONITORING AGENCY REPORT NUMBER	
11. SUPPLEMENTARY NOTES The views expressed in this thesis are those of the author and do not reflect the official policy or position of the Department of Defense or the U.S. Government.			
12a. DISTRIBUTION/AVAILABILITY STATEMENT Approved for public release; distribution is unlimited.		12b. DISTRIBUTION CODE	
13. ABSTRACT (maximum 200 words) This thesis reports the results of a laser annealing technique used to remove defect sites from radiation damaged indium phosphide on silicon MOCVD grown solar cells. This involves the illumination of damaged solar cells with a continuous wave laser to produce a large forward-biased current. The InP/Si cells were irradiated with 1 MeV electrons to a given fluence, and tested for degradation. Light from an argon laser was used to illuminate four cells with an irradiance of 2.5 W/cm ² , producing a current density 3 to 5 times larger than AM0 conditions. Cells were annealed at 19°C with the laser and at 25°C under AM0 conditions. Annealing under laser illumination of n/p-type cells resulted in recovery of 48%. P/n type cells lost 4 to 12% of the assumed degradation. Annealing under AM0 conditions resulted in power recovery of 70% in n/p type cells. P/n-type cells recovered approximately 16% of lost power. Results indicate that significant power recovery results from the annealing of defects within n/p type InP/Si solar cells.			
14. SUBJECT TERMS Indium Phosphide, Solar Cells, Annealing, Lasers			15. NUMBER OF PAGES 148
			16. PRICE CODE
17. SECURITY CLASSIFICATION OF REPORT Unclassified	18. SECURITY CLASSIFICATION OF THIS PAGE Unclassified	19. SECURITY CLASSIFICATION OF ABSTRACT Unclassified	20. LIMITATION OF ABSTRACT UL

NSN 7540-01-280-5500

Standard Form 298 (Rev. 2-89)
Prescribed by ANSI Std. Z39-18 298-102

Approved for public release; distribution unlimited.

**POWER RECOVERY OF RADIATION DAMAGED MOCVD GROWN INDIUM
PHOSPHIDE ON SILICON SOLAR CELLS THROUGH ARGON-ION LASER
ANNEALING**

Lynn L. Boyer IV
Lieutenant, United States Navy
B.E., Vanderbilt University, 1989

Submitted in partial fulfillment
of the requirements for the degree of

MASTER OF SCIENCE IN ELECTRICAL ENGINEERING

from the

**NAVAL POSTGRADUATE SCHOOL
June 1996**

ABSTRACT

This thesis reports the results of a laser annealing technique used to remove defect sites from radiation damaged indium phosphide on silicon MOCVD grown solar cells. This involves the illumination of damaged solar cells with a continuous wave laser to produce a large forward-biased current. The InP/Si cells were irradiated with 1 MeV electrons to a given fluence, and tested for degradation. Light from an argon laser was used to illuminate four cells with an irradiance of 2.5 W/cm², producing a current density 3 to 5 times larger than AM0 conditions. Cells were annealed at 19°C with the laser and at 25°C under AM0 conditions. Annealing under laser illumination of n/p-type cells resulted in recovery of 48%. P/n type cells lost 4 to 12% of the assumed degradation. Annealing under AM0 conditions resulted in power recovery of 70% in n/p type cells. P/n-type cells recovered approximately 16% of lost power. Results indicate that significant power recovery results from the annealing of defects within n/p type InP/Si solar cells.

TABLE OF CONTENTS

I. INTRODUCTION	1
II. SOLAR CELLS	5
A. SEMICONDUCTOR THEORY	5
B. SOLAR CELL DIODE CHARACTERISTICS	12
1. P/N Junction and Diffusion Current	12
2. Drift Current	13
3. Diode Dark Current	13
C. ILLUMINATED SOLAR CELL CHARACTERISTICS	15
1. Bandgap Energy	15
2. Spectral Response	16
3. Photogenerated Current	18
D. SOLAR CELL PARAMETERS	21
III. SPACE ENVIRONMENT AND RADIATION EFFECTS	25
A. SOLAR WIND	25
B. RADIATION DAMAGE MECHANISMS	29
1. Inelastic Collisions with Atomic Electrons	29
2. Elastic Collisions with Atomic Nuclei	29
3. Inelastic Collisions with Atomic Nuclei	29
C. IONIZATION AND DISPLACEMENT DAMAGE	30
IV. ANNEALING AND LASER ILLUMINATION	35
A. THERMAL ANNEALING	35
B. MINORITY CARRIER INJECTION ANNEALING	36
1. Forward Bias Current Injection	37
2. Photoinjection Annealing	38
C. LASERS	39
V. INDIUM PHOSPHIDE (INP) SOLAR CELLS	41
A. InP HISTORY	41
B. INP/SI SOLAR CELLS	44
VI. EXPERIMENTAL PROCEDURES AND RESULTS	45
A. EQUIPMENT SETUP	45
1. Solar Simulator	48
2. Measurement Meters	49
3. Instrument Control	50
4. Test Stand	50
B. TEST PLAN	52
C. RESULTS	55
VII. CONCLUSIONS	59

APPENDIX A. SILICON REFERENCE CELL DATA SHEET	61
APPENDIX B. SOLAR CELL DATA PLOTS	63
LIST OF REFERENCES	129
INITIAL DISTRIBUTION LIST	133

LIST OF FIGURES

Figure 2.1 Zincblende Crystalline Structure Common to Many Semiconductors Including InP. [Ref. 8: p. 7]	6
Figure 2.2 Simplified Energy Band Diagram for a Crystal. [After Ref. 24: p. 14]	8
Figure 2.3 Energy Bands Diagrams for a) an Insulator, b) a Semiconductor, and c) a Conductor. [After Ref. 4: p. 815]	9
Figure 2.4 Energy Bands with the Introduction of a) Donor Impurities and b) Acceptor Impurities. [After Ref. 7: p. 29]	10
Figure 2.5 Charge Depletion Region in p/n Junction. [Ref. 8: p. 12]	12
Figure 2.6 Solar Cell Dark IV Curve for InP/Si n/p Cell #1 Used in This Research. ...	14
Figure 2.7 Incident Light on a Solar Cell Creates Electrons Hole Pairs, Which Are Separated by Potential Barrier, Creating a Voltage That Drives a Current Through an Electrical Circuit. [Ref. 14: p. 5]	16
Figure 2.8 Solar Spectrum Above and Below the Earth's Atmosphere and the 5900 K Black Body Curve.	17
Figure 2.9 Photogenerated current separated by Depletion Region. [Ref. 8: p. 13]	18
Figure 2.10 Cross Section and Top Views of a Solar Cell. [Ref. 12: p. 26]	19
Figure 2.11 Light and Dark IV Measurements for a n/p InP on Si Solar Cell. The Light IV Curve Pulls the Dark Down. [After Ref. 12: p. 32]	20
Figure 2.12 Normal Light IV Curve with Cell Parameters Shown.	21
Figure 3.1 Cross Section of the Earth's Magnetosphere. [Ref. 22:p. 1424]	26
Figure 3.2 Inner and Outer Electron Radiation Belts. [Ref. 1: p. 200]	27
Figure 3.3 Proton Density Distribution in the Van Allen Belts. [Ref. 1: p 201]	28
Figure 3.4 Crystal Damage Displacement: Closely Spaced Interstitials and Vacancies, or Frenkel Pairs. [Ref. 8: p. 35, Ref. 16: p. 181]	32
Figure 3.5 Four Recombination/Generation Processes Affecting Solar Cell	

Output: a) Electron/Hole Trapping, b) Recombination, c) Generation, and d) Compensation. [Ref. 12: p. 14]	33
Figure 4.1 Recombination and Energy Release at the Defect Site [Ref. 24: p. 36] . . .	37
Figure 5.1 Normalized Efficiency of Illuminated InP, Dark InP, Si, and GaAs Solar Cells [Ref. 30: p. 43]	43
Figure 6.1 Block Diagram of Test Equipment Including the Solar Simulator, Test Cell, Reference Cell, Power Supply, Meters, and PC.	46
Figure 6.2 Experimental Setup Showing the Solar Simulator, Kiethley Picoammeter, and the Cell Test Stand.	47
Figure 6.3 Xenon Arc Lamp and the Sun's Spectrum at AM0 Conditions [Ref. 3: p. 2-6]	48
Figure 6.4 Solar Cell Biasing and Four-Point Measurement Diagram.	49
Figure 6.5 Test Stand Showing Reference Cell and Test Cell, Micromanipulators and Probes, Cooling Tubes and Temperature Sensors.	51
Figure 6.6 Argon-Ion Laser with Fiber-Optic Cable Attached.	53
Figure 6.7 InP/Si Test Cell Under Argon-Ion Laser Illumination.	54

LIST OF TABLES

Table 3.1 Solar Wind Characteristics at 1 AU from the Sun. [Ref. 2: p. 3-1]	26
Table 3.2 Electron-Hole Pair Generation Energies Required for Si, InP, GaAs. [Ref. 19: p. II-17]	30
Table 5.1 InP Solar Cell General Characteristics. [Ref. 23: p. 2]	42
Table 6.1 Silicon Reference Cell AM0 Output Parameters.	49
Table 6.2 BOL Average Parameter Values for n/p and p/n Type InP/Si Solar Cells. .	52
Table 6.4 Percentage of Cell Degradation from BOL Baseline Due to a 1 MeV Electron Fluence of $5 \times 10^{15} \text{ e-/cm}^2$	56
Table 6.5 Percentage of Cell Parameter Recovery from the Degradated Level in Inp/Si Solar Cells Tested in the Solar Simulator.	56
Table 6.6 Assumed Cell Degradation From BOL Baseline Based on Similar Cells Tested in the Solar Simulator.	57
Table 6.7 Cell Recovery for Laser illuminated Test Cells from an Assumed Degradation Baseline.	58

ACKNOWLEDGEMENT

I would like to thank my thesis advisor Sherif Michael for his assistance in making this thesis possible.

A very special thanks to Dr. Rob Walters of the Naval Research Laboratory Washington D.C. for providing the solar cells used in this research. His dedication, time and professionalism were crucial to the understanding of several difficult concepts.

A grateful thanks to Dan Sakoda and Ron Phelps of the Space System Engineering Lab for all their computer and thesis assistance.

To my wife Beth: thanks for putting up with all the long hours. You make it all worth it.

I. INTRODUCTION

Since the beginnings of the space program over four decades ago, solar cells have powered most of the spacecraft launched into earth orbit. Their high power to weight ratio and durability have made solar cells preferable for satellites electrical power systems. Solar cells have powered a variety of spacecraft, including communications, military, weather, and navigation satellites. Wide mission applications lead to a variety of orbits and differing environments. A major drawback to using solar cells for the electrical power system is radiation degradation in the space environment. Particularly harsh orbits can cause the solar array output power to significantly degrade over mission life. Typical array design compensates for these losses by adding extra cells to meet mission life requirements. Various ongoing research seeks to extend the solar array, and subsequently, spacecraft lifetime.

Silicon solar cells compose the bulk of on-orbit satellite solar panels. In recent years, Gallium Arsenide (GaAs) solar cells have replaced silicon as the preferred solar cell material in many applications. Specifically, superior radiation resistance characteristics of GaAs results in longer array and mission life in high radiation environments. Indium phosphide (InP) solar cells exhibit higher radiation tolerance than GaAs solar cells. This research investigates some radiation resistance properties of Metal Oxide Chemical Vapor Deposition (MOCVD) grown n/p and p/n InP solar cells.

For most solar powered spacecraft, mission life and average power requirements determine array size. Solar arrays must supply sufficient power throughout the life of the spacecraft and at End of Life (EOL) to allow the satellite to accomplish its mission. Solar cell on-orbit degradation requires array oversizing to meet EOL power requirements. Mission requirements determine power requirements and typically remain constant over mission life. Oversized arrays affect excess power at the Beginning of Life (BOL) of a satellite. Excess power dissipates as heat. Large oversized arrays can have a significant

impact on the spacecraft's thermal design. Smaller arrays are more desirable [Ref 1: p. 394-396].

The solar array designer balances mass, area, cost, and risk to design an array. A long and proven history has made silicon arrays the least expensive and most reliable solar power system. Unfortunately, they are larger and less efficient than GaAs and InP arrays. The newer GaAs arrays are gradually replacing silicon as their proven flight time increases. InP arrays are extremely expensive and have minimal flight time. Thus, InP arrays carry a high degree of risk [Ref. 1: p. 396].

Spacecraft power requirements have gone from tens of watts at the beginning of the space program to hundreds of kilowatts. The space station *Freedom* is estimated to require 300 kW of electrical power before the end of its mission life. Solar array size corresponds directly to solar cell parameters such as efficiency and power output. As power requirements increase, array size must also increase. Larger arrays are costly and heavy. Launch configuration develops into a significant consideration as array size increases. When launching spacecraft, cost is directly proportional to weight. The larger and heavier a spacecraft, the more expensive to lift it into orbit. Smaller arrays are typically lighter and easier to configure for launch. Array configuration is a significant design consideration. Launch vehicle selection seriously influences the cost of a spacecraft mission. Interior space limitations on the launch vehicle can require folding the solar arrays many times. Depending upon the mission and expected degradation, array size can grow to 30%-40% of EOL required minimum size.

The NAVSTAR Global Positioning System (GPS) is in a 55° degree orbit at an altitude of 20,200 km [Ref. 20: p. 13][Ref. 27: p. 1-2]. Because this orbit is in the heart of the radiation belts, significant radiation degradation quickly results. A similar orbit of 20,372 km at 60° accumulates damage equivalent fluence from electrons of $5.26 \times 10^{13} \text{ e/cm}^2\text{-yr}$ and from protons $2.19 \times 10^{11} \text{ e/cm}^2\text{-yr}$ for a total fluence of $5.28 \times 10^{13} \text{ e/cm}^2\text{-yr}$. For the silicon solar cells used in GPS, this translates to a 9% degradation per year. Seven years in this environment reduces the array output to

approximately 78% of BOL capabilities [Ref. 20: p. 13-14][Ref. 28: p. 554].

Solar cells placed in the space environment will degrade. One possible solution to oversizing the arrays is on-orbit annealing. Annealing allows some power recovery in radiation-damaged solar cells. Lasers can be used to anneal solar cells under certain conditions. The potential exists for a laser to anneal an on-orbit satellite. If this could be accomplished practically, lower launch weights, simplified power conditioning, and longer mission lives could result [Ref. 13: p. 1].

Silicon solar cells are the most common type of solar cells used to power spacecraft. GaAs solar cells have also been used with a high degree of success to power spacecraft and often are superior to silicon due to their increased radiation resistance. InP solar cells, while in the experimental phase, provide better radiation resistance than GaAs and possibly better annealing characteristics; however, InP has high material cost and a brittle structure. Volume production would lower InP material costs, and manufacturing the InP solar cell on a silicon substrate would solve the brittleness problem. Silicon provides structural support and is less expensive to produce. This thesis examines some radiation and annealing characteristics of InP solar cells grown on a silicon substrate. Both n/p and p/n cell types are radiation damaged and annealed with an argon-ion laser.

Chapter II discusses the basic physics of solar cells. Chapter III describes the space radiation environment. Chapter IV discusses solar cell annealing, power recovery, and the laser used in this research, while Chapter V describes the InP on silicon cells used in this research. Chapter VI explains the experimental setup, test plan, and results. Finally, Chapter VII presents the conclusions. Data plots for all solar cells can be found in Appendix B.

II. SOLAR CELLS

This section presents some basic physics required to understand solar cell operation. A review of semiconductors, the p/n junction, and diode characteristics are presented. Silicon is used as an example material to illustrate some ideas. Next, various aspects of solar cell operation including bandgap energy, cell characteristics, current-voltage plots, solar spectrum, and cell parameters are covered.

A. SEMICONDUCTOR THEORY

Semiconductors are solid crystalline materials characterized by electrical conductivity less than good conductors but greater than insulators. Silicon and germanium are both examples of semiconductors and have four valence, or outer shell, electrons. Group IV materials on the periodic table of elements are semiconductors. To fill their outer shell of electrons to the preferred number of eight electrons, semiconductor atoms will share their valence electrons with other atoms. When an atom shares its valence electrons with another atom, covalent bonds are formed. Silicon, for example, shares its outer four valence electrons with four other silicon atoms and forms a crystal structure.

During manufacturing, covalent bond formation between silicon atoms results in the development of a crystal structure. The potential required to remove a valence electron is much less than that required to remove any of the other electrons. Because of the low potential required, valence electrons can break the covalent bond and become free to move about the crystal. Light, thermal, or radiation sources can supply the required energy to break the covalent bond. At 300 K for example, approximately 1.5×10^{10} free electrons are moving about one cubic centimeter of pure silicon. These free electrons are

called intrinsic electrons or intrinsic charge carriers. An examination of the thermal characteristics of pure semiconductors reveals an interesting material property: As the temperature increases, the number of intrinsic charge carriers increases, and the material becomes a better conductor. This contrasts with a good conductor such as copper, which becomes less conductive as the temperature increases.

Group IV elements are not the only elements that can behave as semiconductors. Group III and Group V elements can combine to give similar semiconductor properties. Indium, a Group III element has three electrons in its valence band, while phosphorus has five electrons in its valence band. InP forms a crystalline structure that satisfies the atoms need to fill the valence band to eight electrons. Most Group III-V compounds, including InP, form the Zincblende crystal lattice structure. Figure 2.1 shows the Zincblende crystal structure and the bonds between the atoms.

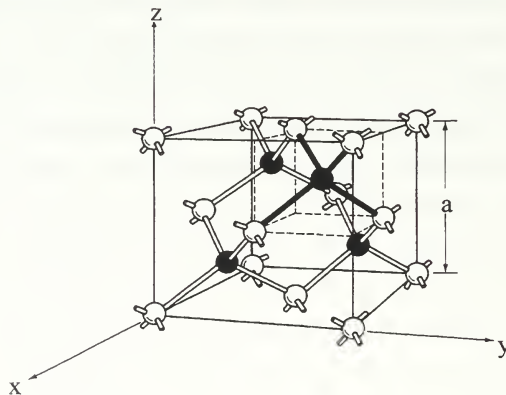


Figure 2.1 Zincblende Crystalline Structure Common to Many Semiconductors Including InP. [Ref. 8: p. 7]

When an electron breaks its covalent bond, it leaves behind a hole in the crystal lattice structure. Holes are considered positively charged due to the absence of the negative electron which neutralizes the positive charge of the proton in the nucleus. Electrons wandering the crystal can recombine with holes to complete the covalent bonds. The process of an electron recombining with a hole is called recombination. Recombination is an important charge carrier loss mechanism and will be discussed later. Because the semiconductor material is electrically neutral, the number of holes equals the number of free electrons.

Electron band theory explains the behavior and theoretical operation of semiconductors. Electrons in a particular atom can only occupy discrete energy states. Energy levels vary from the ground state to higher ones called excited states [Ref 4: p. 813]. In a crystal, the electron of an atom is affected by the potential of all the atoms in the crystal. The potential interaction causes discrete energy levels to differ significantly from those of an isolated atom. Outer shell electrons can be considered in one of two possible states: the ground state for the outer electron shell is called the valence band, and the excited state is the conduction band. Electrons cannot exist in the forbidden energy gap separating the two bands.

Most crystal structures have complex energy band structures [Ref. 6: p. 19]. For the purposes of this discussion, the simplified energy band diagram shown in Figure 2.2 will suffice.

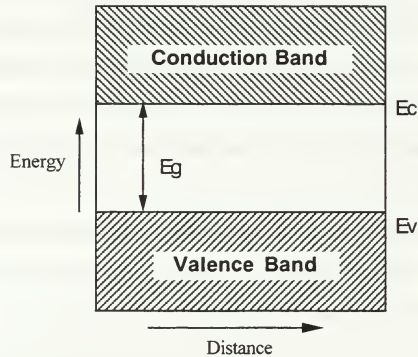


Figure 2.2 Simplified Energy Band Diagram for a Crystal. [After Ref. 24: p. 14]

Electrons need to acquire a minimum amount of energy in order to cross the forbidden energy gap, E_g , from the valence band to the conduction band. Similarly, electrons give up energy to drop down from the conduction band to the valence band. Light, thermal, or radiation sources can supply the required energy for electrons to transition between bands [Ref. 4: p. 813-815]. Figure 2.3 illustrates the relative energy levels between the conduction valence bands for an insulator, semiconductor, and a conductor.

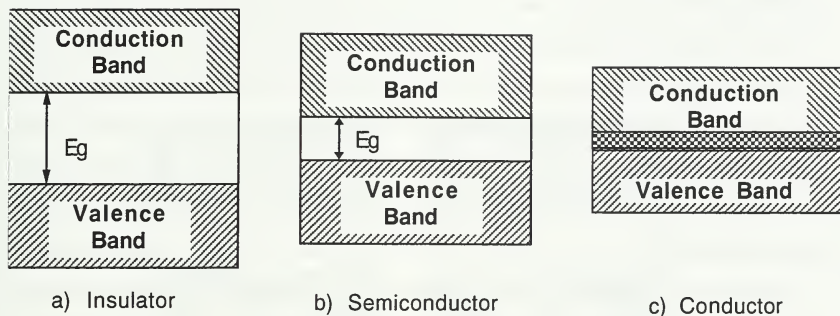


Figure 2.3 Energy Bands Diagrams for a) an Insulator, b) a Semiconductor, and c) a Conductor. [After Ref. 4: p. 815]

In a conductor, the valence band and conduction bands are close together or overlapping. For an insulator, the valence band and conduction band are far apart, and a significant amount of energy is required for an electron to bridge the gap. Semiconductors lie between the two extremes of conductors and insulators.

Semiconductor crystals become p-type or n-type materials by adding impurity atoms, called dopants, to the crystalline structure. Adding pentavalent dopants (materials with five electrons in their outer shell) creates n-type material. Dopants that add electrons are called donors. Four of the dopant atom's valence electrons form the covalent bonds of the crystal. The fifth electron is extra and loosely bound to the dopant atom. The extra electron requires little additional energy to transition to the conduction band and freely move about the crystal. The electron, while free to move around the crystal, leaves a positive space charge at the stationary site of the dopant atom. Considered as a whole,

the semiconductor is electrically neutral. This method of doping reduces the energy required for donor electrons to move freely about the crystal. Figure 2.4 shows the changes to the energy band structure for n-type and p-type material.

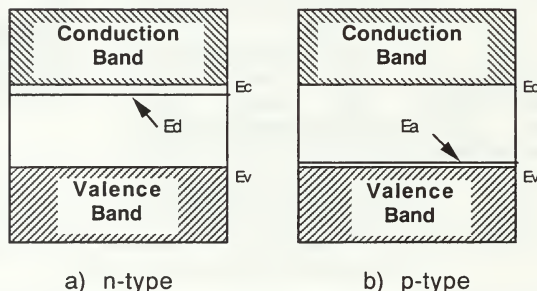


Figure 2.4 Energy Bands with the Introduction of a) Donor Impurities and b) Acceptor Impurities. [After Ref. 7: p. 29]

The addition of dopant atoms from a trivalent material with three valence electrons, creates p-type material. The three valence electrons of the dopant atoms form the covalent bonds of the crystal. Where there would normally be a fourth covalent bond, a hole exists. Free electrons in the crystal may combine with the hole and complete the covalent bond which also introduce a negative stationary charge. As with n-type material, the doped semiconductor is electrically neutral. Impurities added to create p-type material are called acceptors.

The addition of impurity atoms to create n-type or p-type material lessens the effect of the forbidden energy gap of an undoped semiconductor. Electrons in doped semiconductors have less potential to overcome the transition between the valence and conduction bands. Dopants add charge carriers to the semiconductor—an extremely important effect. Charge carrier concentration significantly affects solar cell performance.

As mentioned above, semiconductor conductivity exhibits a proportional temperature dependency. As the temperature increases, the conductivity of a semiconductor increases. At any temperature above absolute zero, sufficient energy exists to break some covalent bonds and ionize electrons to the conduction band where they are free to move about the crystal. The absence of the electrons leaves a hole at the broken bond site. Electrons from neighboring covalent bonds may fill the hole, but in doing so leave a hole at their origin. Thus, holes can propagate through the crystal lattice. Electrons and holes have mobility associated with them. Random motion defines hole and electron mobility. Eventually, holes and electrons will meet and recombine. The recombination rate is proportional to the concentrations of free holes and free electrons. Electron and hole concentrations depend on the ionization rates. At thermal equilibrium, the ionization rate equals the recombination rate, and a constant concentration of charge carriers exists.

The dopant process as mentioned above, increases the concentration of one type of charge carrier. The creation of n-type material increases the concentration of electrons. Because electrons are more populous in n-type material, they are termed the majority charge carriers. Holes become the minority charge carrier. A similar reasoning for p-type material defines holes as the majority charge carriers and electrons as the minority charge carriers [Ref. 8: p. 9-11].

Small impurity concentrations are often used to dope silicon. At 300 K, one free electron exists per 10^{12} Si atoms. A typical n-type donor concentration of 1 in 10^7 atoms increases the majority charge carrier population by a factor of 10^5 for silicon ($10^{12}/10^7=10^5$). This large increase shows how majority charge carrier concentration depends on the number of dopant atoms. The temperature contribution to majority charge carrier concentration is small. Minority charge concentration, however, remains a function of temperature.

B. SOLAR CELL DIODE CHARACTERISTICS

The absence of light causes solar cells to behave as diodes. The joining of p-type material with n-type material creates a p-n junction known as a diode. A diode becomes a solar cell by perforating the n-side or p-side metal contact and shining a light on the diode. The dark current-voltage (IV) measurement characterizes some basic physical parameters of a diode/solar cell. A solar cell dark IV measurement records the dark diode current as a function of diode terminal voltage.

1. P/N Junction and Diffusion Current

When the two types of semiconductor materials are brought together, electrons from the n-type material will diffuse to the p-type material where they recombine with holes in the p-type material. Similarly, holes from the p-type material diffuse to the n-type material and recombine with electrons. The diffusion of charge carriers across the junction creates a diffusion current. The diffusion of charge carriers leaves a charge depletion region at the junction. Figure 2.5 illustrates the charge depletion region of a p/n junction.

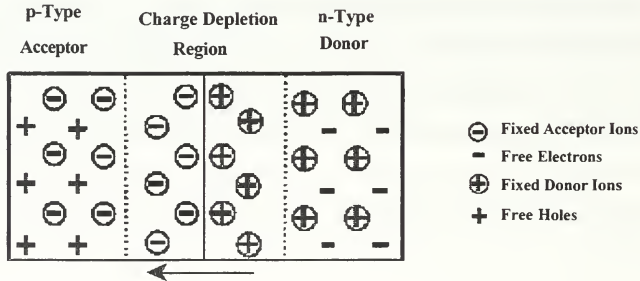


Figure 2.5 Charge Depletion Region in p/n Junction. [Ref. 8: p. 12]

The charge depletion region creates an electrical potential in the opposite direction of the diffusion current. The diffusion current decreases as the electrical potential increases. The diffusion current defines an important parameter used in the complete dark diode equation presented later.

2. Drift Current

The drift current is another important constituent of the dark diode current. Minority charge carriers on both sides of the p/n junction will drift randomly throughout their respective crystal structures. Random n-type hole interaction with the depletion region electric field will cause the hole to quickly sweep across the junction. Electrons in the p-type material may interact with the depletion region electric field and quickly transition to the n-type side of the junction. The two currents added compose the drift current. The drift current acts in the opposite direction of the diffusion current. Unlike the diffusion current, the drift current is independent of the magnitude of the depletion region electrical field. Macroscopically, under open circuit conditions, the drift current is equal and opposite to the diffusion current [Ref 14: p. 7].

3. Diode Dark Current

The total dark diode current is a combination of diffusion current, recombination current, and shunt current. An equation for the p/n junction dark current is given in Equation 2.1

$$I(V) = I_{01} \left(e^{\frac{qV}{kT}} - 1 \right) + I_{02} \frac{\left(e^{\frac{qV}{kT}} - 1 \right)}{e^{\frac{qV}{2kT}} + \cosh\left(\frac{E_t - E_i}{kT}\right)} + \frac{V}{R_{sh}} \quad (2.1)$$

where $I_{01} = q \left(\frac{p_n D_p}{L_p} + \frac{n_p D_n}{L_n} \right)$

and $I_{02} = \frac{qAW}{2} N_t V_{th} \sigma_i$

$I(V)$ is the dark diode current as a function of terminal voltage, V . On the right side, the

first term is the diffusion current; the second term is the recombination current. The term V/R_{sh} represents the shunt current. Reference 12 contains a complete derivation of Equation 2.1. Basically, the first term describes the current due to minority charge carrier drift across the junction. The second term adds the effect of recombination and generation of minority charge carriers due to different loss and gain mechanisms; the shunt current term models diode behavior at small biases. Dark IV curves can be approximated by manipulating the coefficients of Equation 2.1. Final coefficient values provide information about key cell performance parameters including diffusion current, recombination current, shunt resistance, and minority carrier lifetimes [Ref. 12: p. 23]. Equation 2.1 can be fitted to dark IV data curves such as the one shown in Figure 2.6.

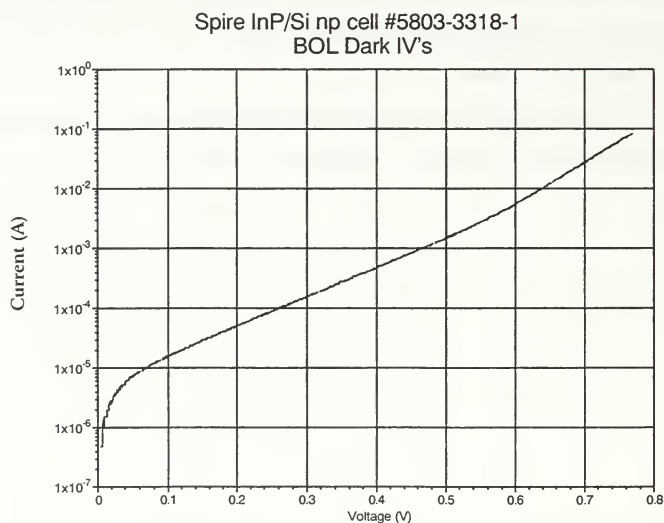


Figure 2.6 Solar Cell Dark IV Curve for InP/Si n/p Cell #1 Used in This Research.

C. ILLUMINATED SOLAR CELL CHARACTERISTICS

Solar cells generate useful electric power when illuminated by a light source. This subsection discusses solar cell bandgap energy and the solar spectrum just outside the Earth's atmosphere. An equation for the photogenerated current is also presented.

1. Bandgap Energy

Solar cells are solid states devices designed to convert sunlight into electrical energy through a process known as the photovoltaic effect. Solar cells are generally classified by material type such as silicon, GaAs, and InP. Each material has a unique bandgap energy associated with it.

Solar cell characteristics are driven from an important characteristic called the bandgap energy. As previously mentioned, the bandgap energy, E_g defines the minimum amount of energy required to free an electron from the outer valence band of an atom. Freeing an electron from the outer valence band creates an electron-hole pair. Electrons in solar cells could receive the required bandgap energy if they are bombarded by photons from sunlight. Photon energy E_p , relates to the frequency of light according to Equation 2.2 [Ref. 9: p. 6].

$$E_p = h \times \nu = h \times \left(\frac{c}{\lambda} \right) = \frac{1.24}{\lambda} \quad (2.2)$$

Where $h \times \nu$ is energy in electron volts, h is Plank's constant, ν is frequency of the light wave, c is the speed of light, and λ is the light wavelength in micrometers. If the energy of the incoming photon is greater than the bandgap energy, $E_p > E_g$, and the photon strikes a valence electron, the electron will absorb the photon energy. The added energy raises the electron from the valence to the conduction band. Once in the conduction band, the electron can move freely through the crystal lattice structure. When the electron leaves the valence band, it leaves behind a positively charged hole. The absorption of the

photon energy creates an electron-hole pair. Multiple interactions between photons and electrons generate the charge carriers in the solar cell. Only photons with energy greater than the band gap energy will create an electron-hole pair. Photons with energy less than E_g are normally dissipated as heat. Photons with more energy than the bandgap energy will generate an electron-hole pair, and the excess energy will be dissipated as heat. Figure 2.7 shows a simplified diagram of a solar cell and the light photon interactions.

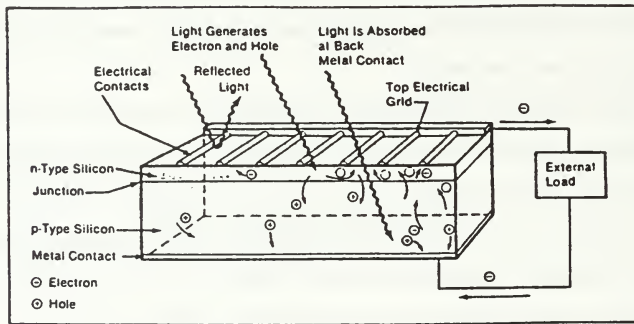


Figure 2.7 Incident Light on a Solar Cell Creates Electrons Hole Pairs, Which Are Separated by Potential Barrier, Creating a Voltage That Drives a Current Through an Electrical Circuit. [Ref. 14: p. 5]

The indium phosphide cells used in this research have a band gap energy of 1.34 eV at 300 K. From Equation 2.2, a bandgap of 1.34 eV equates to a light wavelength of 925 nm. Therefore, light with a wavelength less than or equal to 925 nm will provide enough energy to generate an electron-hole pair.

2. Spectral Response

Sunlight power density near the Earth and outside the Earth's atmosphere, is

called Air Mass Zero, or AM0. AM0 is a common standard used to measure the response of solar cells used in earth orbiting spacecraft. The Earth's atmosphere has a large filtering effect on solar irradiance. Figure 2.8 shows solar irradiance above and below the Earth's atmosphere. Significant absorption bands in the atmosphere attenuate portions of the solar spectrum. To test solar cells, solar simulators approximate AM0 conditions in the laboratory. The sun's power output at AM0 closely resembles a 5900 K black body curve as shown in Figure 2.8.

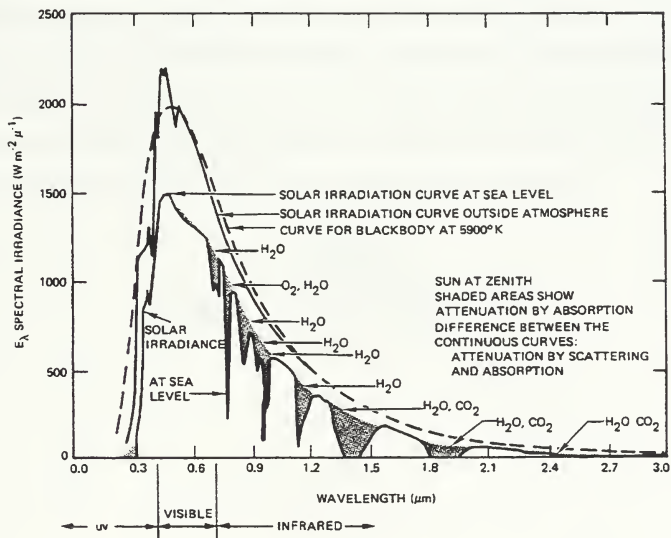


Figure 2.8 Solar Spectrum Above and Below the Earth's Atmosphere and the 5900 K Black Body Curve.

3. Photogenerated Current

A solar cell is created by replacing the flat metal contact on one side of a diode with a metal grid [Ref. 12: p. 25]. The metal grid allows photons to pass through and strike the semiconductor. The solar cell type is determined by which semiconductor material is illuminated by sunlight. In an n/p type solar cell, the metal grid is on the n-side. Conversely, in a p/n type solar cell the metal grid is on the p-side. Incident photons cause the production of electron-hole pairs in the p-type and n-type material of a solar cell. Minority charge carrier migration from the electron-hole pair produces the photogenerated current of the solar cell. Combining the photogenerated current with the dark diode current gives the total output current of the cell.

Photogenerated minority charge carriers occurring in the depletion region will quickly be swept across the junction and produce useful current. Carriers generated in the neutral portion of the cell will diffuse randomly through the cell. Diffusion ends when the carriers reach the cell surface, the junction, or recombine. Charge carriers reaching the junction compose most of the photogenerated current. Figure 2.9 shows a photon striking a solar cell and the diffusion of the minority charge carrier to the junction.

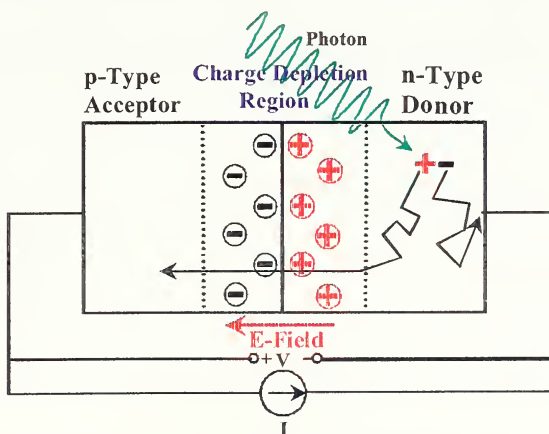


Figure 2.9 Photogenerated current separated by Depletion Region. [Ref. 8: p. 13]

Those minority charge carriers reaching the end of the cell are lost to surface effects. A back surface field added to the base reduces the loss of charge carriers to surface effects at the base interface. A back surface field is composed of a heavily doped material. This material creates an electric field that repels minority charge carriers from the base surface toward the junction. Figure 2.10 shows a top and cross sectional view of an n/p solar cell.

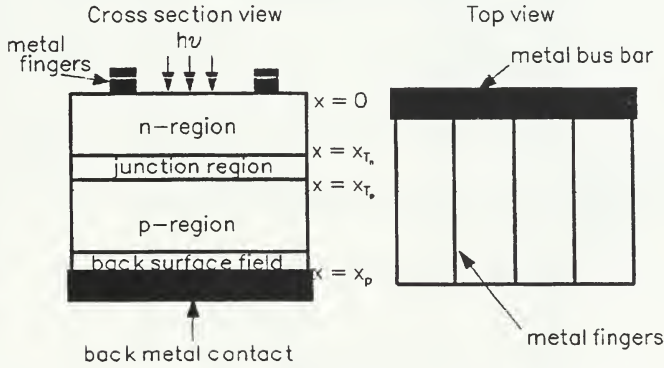


Figure 2.10 Cross Section and Top Views of a Solar Cell. [Ref. 12: p. 26]

The back surface field is shown in the cell cross section, while the metal contact grid is shown in the cell top view [Ref. 12: p. 26].

The addition of the photogenerated current term to the dark diode current, Equation 2.1, results in Equation 2.3:

$$I(V) = -I_{ph} + I_{01} \left(e^{\frac{qV}{kT}} - 1 \right) + I_{02} \frac{\left(e^{\frac{qV}{kT}} - 1 \right)}{e^{\frac{qV}{2kT}} + \cosh\left(\frac{E_t - E_i}{kT}\right)} + \frac{V}{R_{sh}} \quad (2.3)$$

Where I_{ph} is the photogenerated current and the other terms are as previously described

[Ref. 12: p. 31]. The photogenerated current opposes the dark diode current and pulls the cell output current into the negative quadrant. Figure 2.11 shows a dark IV and light IV measurement on a linear current scale.

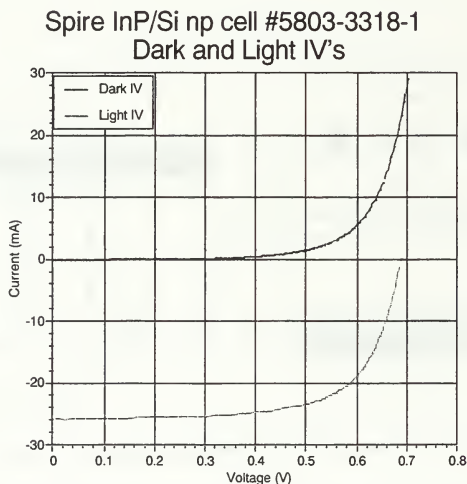


Figure 2.11 Light and Dark IV Measurements for a n/p InP on Si Solar Cell. The Light IV Curve Pulls the Dark Down. [After Ref. 12: p. 32]

In the photovoltaic community, the common convention is to place the light IV curve in the first quadrant as shown in Figure 2.12. This is due to the fact that the direction of the generated current is opposite to the direction of the current in conventional electric circuits employing diodes.

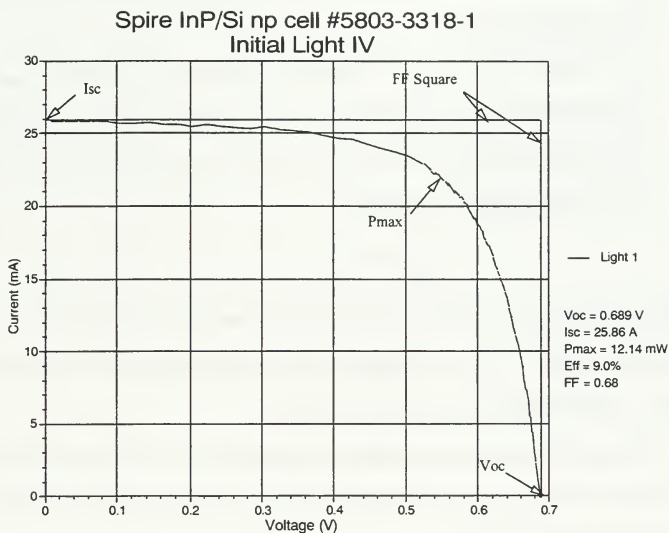


Figure 2.12 Normal Light IV Curve with Cell Parameters Shown.

D. SOLAR CELL PARAMETERS

Solar cells are generally characterized by an illuminated current-voltage (IV) curve. An IV curve for a solar cell is generated by varying the voltage across the terminals from zero volts to the open circuit voltage (V_{oc}). Examination of the resulting light IV curve

shown in Figure 2.12 reveals the following important cell parameters:

1. Open circuit voltage, V_{oc} : Voltage across the cell terminals when cell output current is zero.
2. Short circuit current, I_{sc} : current output of the cell when the voltage across the cell terminals is zero.
3. Maximum Power, P_{max} : The maximum output power of the cell. P_{max} is the point on the IV curve where the corner of the largest rectangle that can be drawn inside the curve intersects with the IV curve. P_{max} occurs on the knee of the curve. P_{max} is calculated by Equation 2.4:

$$P_{MAX} = V_M \times I_M \quad (2.4)$$

Where V_M and I_M are the voltage and current at the maximum power point. To compute P_{max} experimentally, I and V are multiplied for each point along the IV curve and the resulting maximum value is P_{max} [Ref. 12: p. 35].

Two other parameters are useful when discussing solar cells. Fill Factor (FF) and cell efficiency both describe the ability of the cell to convert sunlight to electricity. FF is determined from Equation 2.5:

$$FF = \frac{P_{MAX}}{V_{OC} \times I_{SC}} \quad (2.5)$$

FF is a measurement of the squareness of the IV curve. A rectangular IV curve would have a FF of one. Typical FF for the cells in this research are 0.6 to 0.7. Efficiency measures the capability of the solar cell to convert the incoming light energy at AM0 to electrical energy. Efficiency (η) is calculated by the following equation:

$$\eta = \frac{P_{MAX}}{P_{in}} \times 100 = \frac{P_{MAX}}{135.3 \text{mW/cm}^2 \times \text{cell area in cm}^2} \times 100 \quad (2.6)$$

where P_{in} is the incident power of sunlight at AM0. All cells used in this research are 1 cm² cells. As such, 135.3 mW/cm² is used for input power throughout this thesis.

III. SPACE ENVIRONMENT AND RADIATION EFFECTS

Many satellites orbiting the Earth use solar cells arranged in panels to supply electrical power. Four decades of experience in space has made the space environment near the Earth well understood. Solar cell longevity and performance directly relate to the space and radiation environment. The space milieu is an unusually harsh environment and contains many sources of damaging radiation. Radiation is the primary source of degradation of solar cell parameters. The space radiation environment consists of various types of radiation including electrons, protons, gamma rays, and alpha particles. Due to their low fluxes, gamma and alpha particles are smaller sources of damage than protons or electrons. This thesis neglects gamma and alpha effects because they are insignificantly small.

Many factors in the space environment dictate the radiation dose that solar cells are exposed to. Factors such as spacecraft altitude, magnetic latitude, solar activity, and mission longevity influence the radiation degradation of solar cells. The spacecraft's mission dictates orbit, altitude, and latitude. Mission requirements may cause it to pass through radiation belts of varying intensity.

A. SOLAR WIND

The spacecraft's orbit has the largest impact on the amount of radiation a spacecraft experiences during its lifetime. Orbital factors such as altitude and inclination define the satellite's path through the radiation environment. The space environment outside the Earth's atmosphere is a complex and dynamic system. The sun continuously emits energetic particles such as electrons and positive ions. Charged particles emitted from the sun form the solar wind. Characteristics of the solar wind at the Earth's orbit are summarized in Table 3.1 [Ref. 2: p. 3–1].

	Minimum Values	Average Values	Maximum Values
Flux (10^8 ions/cm ² sec)	1.0	3.0	10
Velocity (km/sec)	300	468	700
Density (ions/cm ³)	3.2	6.5	20
Electron Temperature (K)	90,000	140,000	2×10^5
Proton Temperature (K)	10,000	50,000	3×10^5
Magnetic Field Strength (nT)	2.2	6.6	10

Table 3.1 Solar Wind Characteristics at 1 AU from the Sun. [Ref. 2: p. 3-1]

The solar wind impinges on the daylight side of the Earth's magnetic field. Figure 3.1 shows the Earth's magnetosphere and the effects of the solar wind.

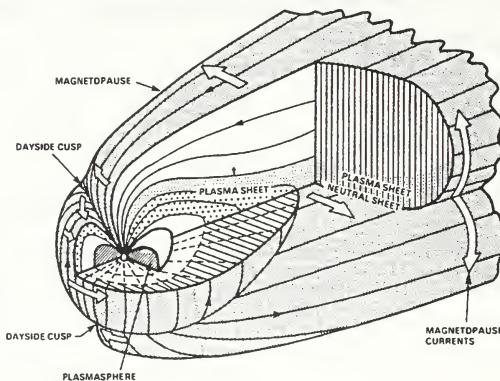


Figure 3.1 Cross Section of the Earth's Magnetosphere. [Ref. 22:p. 1424]

On the daylight side of the Earth, the solar wind compresses the magnetosphere, while on the dark side, it expands the magnetosphere. As Table 3.1 shows, the characteristic values of the solar wind can change markedly. Events such as solar flares and sun spot activity cause the values to change. The degree of compression of the magnetosphere is dependent upon the sun's activity. Charged particles from the solar wind below a critical energy become trapped in the Earth's magnetic field. Because sun activity varies, the number of particles trapped from the solar wind also varies.

The radiation belts surrounding the Earth are known collectively as the Van Allen radiation belts. The Van Allen belts contain charged particles from the solar wind. The particles are trapped by the Earth's magnetic field. Electrons and protons compose most of the charged particles in the Van Allen belts. Figure 3.2 shows electron distribution in the Van Allen belts.

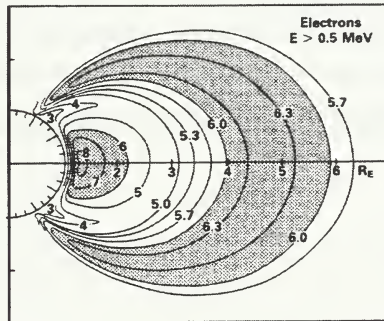


Figure 3.2 Inner and Outer Electron Radiation Belts. [Ref. 1: p. 200]

As Figure 3.2 shows, the electrons favor two main regions around the Earth. The inner Van Allen belt extends from 1.2 Earth radii, R_E , to approximately 2.2 R_E . The main

concentration of radiation in the outer Van Allen belt extends from approximately $4-6 R_E$ [Ref. 1. p. 200]. To a lesser extent, the outer Van Allen belt extends to $11 R_E$ [Ref 10: p. 5-34]. Protons are the other main constituent charged particle in the Van Allen belts. Figure 3.3 shows proton distribution in the Van Allen belts. The radiation belts tend to follow the magnetic lines of force and form a torus-like shape about the Earth.

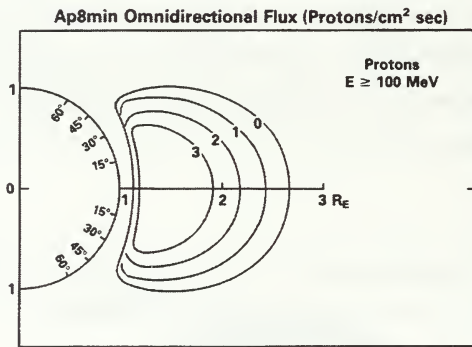


Figure 3.3 Proton Density Distribution in the Van Allen Belts. [Ref. 1: p 201]

Protons and electrons compose most of the radiation damage mechanisms. The high flux of either particle will lead to higher radiation dosages. The majority of radiation to an orbiting spacecraft occurs in the Van Allen belts. Protons and electrons both constitute the inner radiation belt while mainly electrons make up the outer belt. Low Earth Orbit (LEO) satellites are subjected to electron and proton damage, whereas Geosynchronous Earth Orbit (GEO) satellites experience electron radiation. Highly elliptical orbit (HEO) satellites experience both radiation belts.

Electron and proton radiation occurs across a broad spectrum of energies. Most radiation measurements are done with respect to 1 MeV electrons.

B. RADIATION DAMAGE MECHANISMS

Radiation damage effects are extremely complex and depend on the incident particles mass, charge, and energy. Damage occurs to spacecraft and solar cells through a variety of mechanisms. The various charged particles interact with materials via the following processes [Ref. 3: Ch. 3]:

1. Inelastic Collisions with Atomic Electrons

Incoming charged particles collide with bound electrons of the target material. The incident particle transfers energy to orbiting electrons on its way through the material. The incoming charged particle may be of sufficient energy to cause multiple collisions. Each collision causes the particle to give up some energy. Orbiting electrons on the receiving end of a collision undergo a transition to an excited state where the electron may be unbound and free to move about the crystal lattice. Otherwise, the electron will remain bound in an excited state until it releases the energy as a photon, phonon (lattice vibration), or heat. This process is the primary means by which incoming charged particles deposit energy in a material.

2. Elastic Collisions with Atomic Nuclei

Incident charged particles may strike an atomic nucleus or have coulombic interactions with the nucleus through Rutherford scattering. In either case, enough energy may be transferred to the atom to displace it from its lattice position. High enough energy can cause the displaced atom to displace several neighbor atoms from their lattice positions.

3. Inelastic Collisions with Atomic Nuclei

In this general process, a highly energetic proton collides with an atomic nucleus leaving the nucleus in an excited state. The excited or activated nucleus emits nucleons

causing the nucleus to recoil. The recoiling nucleus displaces from the lattice position and displaces neighboring atoms from their lattice positions in the material.

C. IONIZATION AND DISPLACEMENT DAMAGE

The above interactions cause two general types of damage to solar cells: ionization and displacement [Ref. 15: p. 149]. Ionization creates charge centers in some solar cell materials that adversely impact cell performance. Some ionization interactions result in electron-hole production. This benefit is small compared to the long term damage. Displacement damage is a far more significant effect. Displacement damage causes defects in the crystalline structure of the material. Each damage effect will be discussed briefly.

Ionization occurs when an incident particle adds energy to the orbital electrons of an atom and strips the electrons away. Typically, ionization adds enough energy to valence electrons to transport them into the conduction band. Table 3.2 contains electron-hole pair required energy levels for ionization and photon generation.

Material	E_b (eV) Bandgap Energy Photo Excitation @ 300 K	E_p (eV) Ionizing Radiation Electron-hole Pair Production	Density (g/cm ³)	Electron-hole Pair Density generated/rad, g ⁰ (pairs/cm ³)
Si	1.1	3.6	2.328	4×10^{13}
InP	1.34	4.38	4.787	6.8×10^{13}
GaAs	1.42	4.8	5.32	7×10^{13}

Table 3.2 Electron-Hole Pair Generation Energies Required for Si, InP, GaAs.
[Ref. 19: p. II-17]

Ionization has a significant effect on other materials comprising a solar cell, especially the coverglass. Long term effects form dark color centers in the coverglass. Discoloration acts as an optical filter that inhibits photon passage through the coverglass to the solar cell. A reduction of incident photon flux decreases solar cell output. Ionization electrons can be trapped by impurities in the crystal structure and develop into stable charge centers. These charge centers cause the discoloration of the coverglass [Ref. 3: p. 3-3].

Silicon dioxide, often used as a surface coating and dielectric material, adversely reacts to long term ionization. Long term ionization in silicon dioxide causes trapped charge centers to be formed. These charge centers can cause channeling in transistors, increased threshold voltages, and increased leakage currents in the solar cell [Ref. 3: p. 3-6]. Ionization slightly benefits a solar cell by creating electron hole pairs. Significantly higher energy electrons are required for ionization to create an electron-hole pair than for photons. Electron-hole pair production by ionization impacts majority and minority carrier concentrations in the cell. Ionization pair-production will slightly increase the output of the cell.

Displacement damage is the physical movement of an atom from its normal crystal lattice position. The displacement probability depends upon incident particle energy and impact geometry. Elastic and inelastic collisions with atomic nucleus are the primary mechanisms of displacement. The displaced atom leaves a vacancy and creates a defect in the crystal. The displaced atom leaves its lattice location with a certain amount of energy called the recoil energy. A recoiling nucleus with a large amount of recoil energy can displace other atoms in the lattice. The recoil energy depends upon the amount of energy transferred from the incident particle at collision. For the 1 MeV electron irradiation used in this research, recoil energy is low enough that only the original nucleus is displaced [Ref. 12: p. 36-37].

Displaced atoms that find semi-stable positions in the crystal are called interstitials. Interstitials and vacancies remaining in close proximity form Frenkel pairs as shown in Figure 3.4.

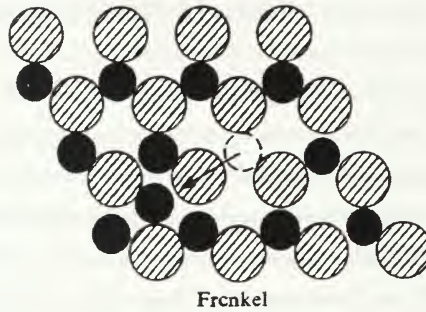


Figure 3.4 Crystal Damage Displacement: Closely Spaced Interstitials and Vacancies, or Frenkel Pairs. [Ref. 8: p. 35, Ref. 16: p. 181]

Long term exposure can cause displacement centers to grow until significant defects occur throughout the crystal [Ref. 3: p. 3–6]. Defects in the crystal create additional energy states in the energy gap. Defects sites can act as recombination centers resulting in a decrease in minority charge carrier lifetimes. A decrease in minority carrier lifetime means less chance the minority charge carrier will make it to the junction and become part of the photogenerated current [Ref. 15: p. 157]. In general, any disturbance to the lattice structure adds energy levels to the energy band structure of the crystal. Radiation induced defects add crystal disturbances and energy band levels. These defects reduce solar cell

electrical properties via a variety of mechanisms [Ref. 21: p. 1446]. Figure 3.5 reveals four of the primary mechanisms that affect solar cell output. The four mechanisms shown in Figure 3.5, electron/hole trapping, recombination, generation, and compensation result from defect disturbances of the energy band structure. All four mechanisms affect minority carrier lifetime and solar cell output.

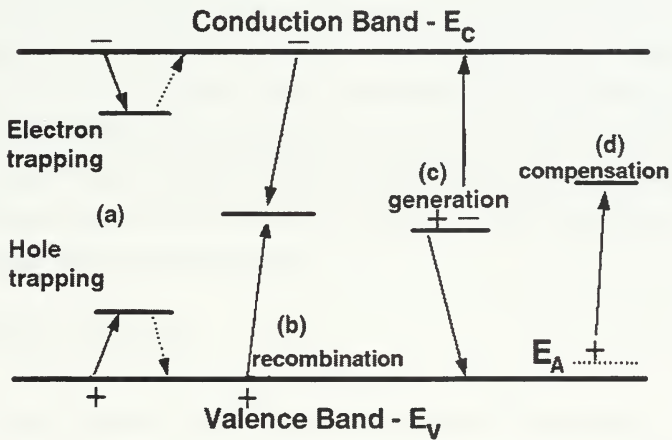


Figure 3.5 Four Recombination/Generation Processes Affecting Solar Cell Output:
a) Electron/Hole Trapping, b) Recombination, c) Generation, and d) Compensation.
[Ref. 12: p. 14]

IV. ANNEALING AND LASER ILLUMINATION

Annealing is a process commonly used in the metals industry to remove defects and strengthen metals. As applied to solar cells, annealing refers to the removal or reduction of defect sites in the crystal lattice. Two methods of annealing are common to solar cells: thermal annealing and minority carrier injection annealing. Chapter III discusses the radiation environment and how damaged occurs to the solar cell crystal lattice structure. For annealing to be effective, displaced atoms must move to satisfactory lattice positions. Both types of annealing raise the energy level in the cell allowing substrate electrons to become excited and return to the vacancies in the crystal lattice structure [Ref. 16: p. 1178]. Defect reduction increases minority carrier lifetime. This results in an increase in all cell output parameters. Minority carrier injection annealing is the main research topic of this thesis. Annealing in solar cells can occur from sunlight and from other sources such as a laser. This chapter discusses two types of annealing and how a laser can be used to anneal solar cells.

A. THERMAL ANNEALING

Thermal annealing is the most common and simplest method of annealing materials. The simple addition of heat raises the energy level of the crystal and increases the mobility of trapped defects. The higher the temperature, the more active the crystal and the better the annealing effects. Several methods of thermal annealing exist. The three most common methods as applied to solar cells include post-annealing, periodic thermal annealing, and continuous annealing. Post-annealing entails raising an irradiated solar cells temperature for a fixed amount of time. Periodic thermal annealing involves irradiation at room temperature and isothermally annealing at a specified temperature for a fixed amount of time. This process can be repeated many times. Continuous, or in-situ

annealing, is the annealing of the solar cell while irradiation occurs [Ref. 9: p. 23] [Ref. 16: p. 1178].

Thermal annealing has three major drawbacks. First, significant results require high temperatures. High temperatures can cause dopant impurity atoms at the p/n junction to migrate causing a reduction in the effectiveness of the junction [Ref. 18: p. 46]. Second, above 190°C, the lead-tin solder used in solar cell contacts begins to melt [Ref. 17: p. 161]. Realistic annealing of an on-orbit solar array would have to be accomplished at a temperature less than 190°C to ensure no array damage. Finally, it is difficult to raise the temperature of an on-orbit array to an annealing temperature. Raising array temperature, in general, requires electrical power. As a rule, spacecraft do not have significant amounts of spare electricity. Extra power requires larger heavier arrays and significantly increases mission cost.

B. MINORITY CARRIER INJECTION ANNEALING

Minority carrier injection annealing introduces large forward biased currents through the solar cell. The large current causes charge carriers to recombine with traps and charge carriers of the opposite sign. Recombination releases a small energy in the form of photons, phonons, or heat. Phonons are lattice vibrations that travel through a crystal in much the same way as acoustics waves through the ocean. High recombination rate increases the number of phonons. Phonons tend to distort the energy band structure of the crystal. The distortion may be enough to release trapped charged particles and restore portions of the crystal lattice [Ref. 8: p. 56]. Figure 4.1 provides a schematic representation of recombination and energy release. At defect site, recombination vibrates the lattice and releases some heat. Both effects anneal the cell. Minority carrier injection annealing avoids the high temperature requirements of thermal annealing. Significant power recovery has been demonstrated in GaAs and InP solar cells using injection annealing at significantly lower temperatures than thermal annealing [Ref. 16: p. 1178].

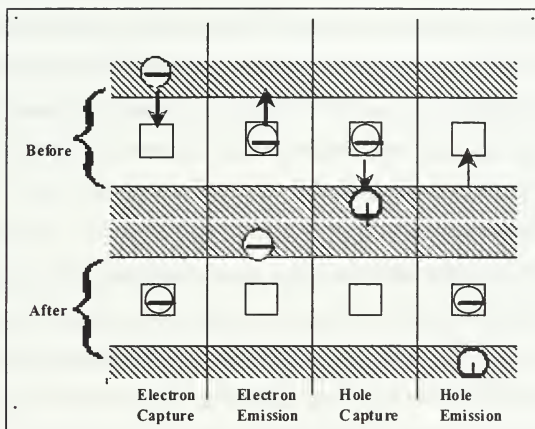


Figure 4.1 Recombination and Energy Release at the Defect Site [Ref. 24: p. 36]

Minority Carrier Injection Annealing generally occurs via two methods: 1. Forward Bias Current Injection, and 2. Photoinjection.

1. Forward Bias Current Injection

An external voltage source applies a forward bias to the cell. The forward bias forces a current through the cell. Since a solar cell is simply a special type of diode, application of the forward bias will result in a current through the cell. As discussed above, the large current induced in the cell will increase the concentration of minority charge carriers. Recombination between charge carriers at defects sites will anneal the crystal structure. Because the cell contains some resistance, heat will be generated by the

current and the cell temperature will increase. Adding heat at the defect sites can only enhance the annealing effect. This annealing method has been shown at the Naval Postgraduate School to successfully induce some power recovery in solar cells [Ref. 18: p. 68][Ref. 20: p. 45].

This annealing method requires an external voltage source to generate the forward bias and induced current. The large bias and current requirements are difficult to fulfill with the typical spacecraft power budget. The solar array requirements would increase, defeating the original purpose of using smaller arrays. This annealing technique precludes array usage for the annealing duration.

2. Photoinjection Annealing

Photoinjection annealing generates a large current employing an intense light source as opposed to a forward bias. Light sources vary from broad spectrums such as the sun to monochromatic laser light. Laser light energy wavelength must provide sufficient photon energy to overcome the bandgap energy of the solar cell. Lasers efficiently added minority charge carriers, current, and heat to anneal the solar cell. As a result, lasers are ideally suited to this annealing technique. Adding heat may provide a beneficial effect for this annealing technique. Photoinjection annealing can occur under any illumination condition and cause some annealing in InP solar cells under irradiation. As will be shown later, InP solar cells under illumination can anneal while they are being irradiated.

Laser photoinjection annealing has induced power recovery in radiation damaged GaAs solar cells [Ref. 9: p. 57]. These GaAs cells were irradiated to an equivalent 1 MeV fluence of approximately $1 \times 10^{15} \text{ e-/cm}^2$. A 500 mW continuous wave argon laser (wavelength 475-514 nm) was used to illuminate the cells at 90°C for an average of 16 hours. Roughly 15% of the cells' lost power was recovered.

C. LASERS

This research uses Spectra-Lab's Model-146 8-watt continuous wave argon-ion laser to provide the concentrated light source for photoinjection annealing. As shown earlier, light with wavelength less than 925 nm provides sufficient photon energy to generate electron-hole pairs. Photon energy at wavelengths greater than the bandgap cutoff energy provide no useful energy to the creation of the photogenerated current and have the detrimental effect of heating the solar cell. The Model-146 laser operates in multimode and produces light wavelengths in the range of 454.5-528.7 nanometers. The laser was operated in mode TEM_{01} . Laser annealing uses the much higher efficiency of the solar cell under laser light to produce a large current density in the solar cell. Laser light in this wavelength produces current directly from minority charge carrier production. The high current density should increase the annealing effects.

Laser and the use of photoinjection annealing provide an attractive alternative to forward biasing annealing techniques. The Strategic Defense Initiative (SDI) resulted in significant research in the area of lasers. Powerful ground-based lasers may eventually have the capability of illuminating an orbiting spacecraft solar array [Ref. 29: p. 3]. On-orbit annealing of solar cells would allow smaller, more compact, and cheaper solar arrays for future satellites to be launched into orbit.

Various ground-based laser concepts are in the developmental stage. One type of laser being researched is the Fission-Activated Laser CONcept (FALCON) Reactor Pumped Laser (RPL). This nuclear powered laser is envisioned to have high power, a self contained power unit, and the potential for shipboard installation. A second type of laser is the Mid-Infrared Advanced Chemical Laser (MIRACL). This is a powerful chemical laser that works in the mid-IR range. While its wavelength is too long for solar applications, frequency doublers exist that could bring the laser output wavelength into the realm of solar cells. Lastly, the Free Electron Laser (FEL) has received significant attention. Its low power requirements and tuneable output make it unique among its

peers. The previous laser concepts were presented as an indication of the potential laser applications of the future. Powerful ground-based lasers will exist in the near future. Their potential application for spacecraft solar cells is one application.

Laser illumination of GEO spacecraft raise the possibility of reducing on-board electrical storage requirements. GEO spacecraft experience up to 90 minutes of eclipse time for some orbits. The electrical storage system required to power the spacecraft during eclipse can weight up to 10% of the spacecraft weight. Some of the powerful lasers mentioned could illuminated the solar arrays during the eclipse period and reduce or eliminate the electrical storage requirements [Ref. 29: p. 3].

V. INDIUM PHOSPHIDE (INP) SOLAR CELLS

As discussed in Chapter III, the radiation environment degrades solar cell output, thus requiring arrays to be oversized at BOL. Gallium Arsenide is slowly replacing silicon as the preferred solar cell material for high radiation environments. High radiation resistant solar cells provide many benefits to a spacecraft program including smaller arrays and longer mission life. InP solar cells possess higher radiation resistance than GaAs.

This chapter briefly discusses the InP solar cell history and the advantages and disadvantages of InP over other types of cells. The cells used in this research are also presented.

A. InP HISTORY

InP is a Group III-V combination semiconductor with a zincblende crystal structure. Table 5.1 gives some material properties of InP.

Crystal Structure	Zincblende
Lattice Constant	5.869 Å
Density	4.787 g/cm ³
Melting Point	1330-1335 K
Dielectric Constant	12.35 x need epsilon
Band-gap	1.34 eV at 300 K
Electron Affinity	4.38 eV
Temperature Dependence of Band-gap	-4.6x10 ⁻⁴ eV/K
Electron Mobility	3-5x10 ³ cm ² /Vs @ 300 K
Hole Mobility	80-150 cm ² /Vs @ 300 K
Electron Diffusion Length	1μ m @ 300 K
Hole Diffusion Length	1.6μ m @ 300 K
Electron Effective Mass	0.05–0.07 m _e
Hole Effective Mass	0.4–0.8 m _e
Surface Recombination Velocity	(n-type) 10 ³ –2x10 ⁴ cm/s
Surface Recombination Velocity	(p-type) 1.5x10 ⁵ cm/s
Intrinsic Carrier Concentration	6x10 ⁶ –2x10 ⁷ cm ⁻³

Table 5.1 InP Solar Cell General Characteristics. [Ref. 23: p. 2]

Yamaguchi et al. of Nippon Telegraph and Telephone Co. (NTT) manufactured the first diffuse junction InP solar cells in 1983 [Ref. 25][Ref. 26: p. 1]. Experiments showed diffuse junction InP cells were more resistant to Co-60 γ-ray radiation than silicon or GaAs. A more significant result is shown in Figure 5.1.

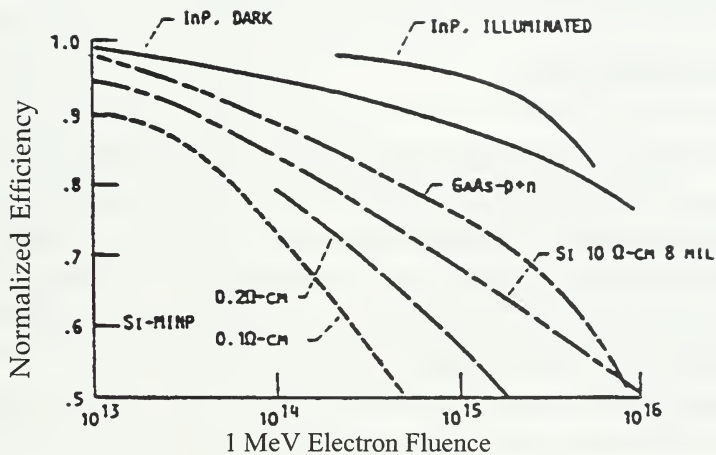


Figure 5.1 Normalized Efficiency of Illuminated InP, Dark InP, Si, and GaAs Solar Cells [Ref. 30: p. 43]

InP irradiated while under illumination shows less degradation for a given fluence level of 1 MeV electrons. The cells demonstrated optical-injection annealing of defect levels in the solar cell. Defect recovery resulted in longer minority carrier lifetime and a corresponding recovery of I_{sc} . The damaged rate almost equaled the recovery rate. The data suggested that for some orbits InP solar cell would scarcely degrade. Average cell efficiency was around 16%. The development MOCVD grown homojunction InP cells produced AM0 efficiencies on the order of 18-19%. In 1988, Naval Research Laboratory (NRL)

Washington D.C. commenced a major research effort on InP solar cells. MOCVD Shallow Homojunction (SHJ) InP cells were produced under contract by Spire Corporation. NRL conducted extensive research and demonstrated that InP cells with high efficiencies can have high radiation resistance [Ref. 12: p. 73-77].

B. INP/SI SOLAR CELLS

While InP has demonstrated excellent radiation resistance capabilities, its high brittleness raises some question about spacecraft utility. Space mission are extremely expensive, and only the most reliable hardware is lifted into space. GaAs solar cells have been shown to be more efficient and radiation resistant than silicon for over 20 years. Only now are GaAs cells preferred for some applications than silicon. In an effort to mitigate InP's inherit brittleness, heterojunction epitaxial InP cells have been manufactured. Heterojunction epitaxial means the InP cell is grown on a silicon substrate instead of an InP substrate. Since silicon is less brittle than InP, it provides needed structural support to the InP junction. A silicon substrate will reduce manufacturing material costs. InP is a difficult and expensive material to produce. Silicon is much cheaper and easier to produce.

The cells used in this research were manufactured by Spire Corporation under contract to NRL. The cells were epitaxially grown using metalorganic chemical vapor deposition technology (MOCVD). This type of cell growth makes an abrupt junction transition from n-type to p-type or vice versa.

VI. EXPERIMENTAL PROCEDURES AND RESULTS

The purpose of this thesis was to explore differences between the annealing characteristics of n/p and p/n MOCVD grown InP on silicon solar cells. Ten InP/Si solar cells were irradiated to a fluence level of $5 \times 10^{15} \text{ e/cm}^2$ with 1 MeV electrons. After irradiation, the cells were isolated from light sources to the maximum extent practicable. Half the irradiated cells were n/p type while the other half were p/n type. Two n/p type and one p/n type cells were annealed using the solar simulator while performing illuminated IV measurements. The solar simulator illuminated IV measurement verified and established the irradiation damage done to the solar cells. Two of each type cells were illuminated and annealed with a continuous wave 8-watt argon-ion laser. Illuminated IV measurements were then performed on the laser illuminated cells. This research intended to compare the annealing effects of AM0 sunlight with that of the 8-watt argon-ion laser. Sunlight from the solar simulator provides some annealing of the cells. The cell is more efficient under laser illumination and may increase the annealing effects through photoinjection annealing. Also, the differences between the two types of cells is noted in this chapter. For this research, illuminated and dark IV measurements were used to characterize the solar cell performance parameters. This chapter describes the equipment setup, test procedures, and the test plan used to test these cells. Results are also presented.

A. EQUIPMENT SETUP

To generate dark and illuminated IV measurements, cells are placed in a test stand and connected to measurement equipment. Micromanipulator probes establish electrical

contact between the solar cell touch pad and the measurement equipment. Dark IV measurements require a controlled power supply to vary voltage from 0 V to slightly greater than V_{oc} of the solar cell. For a dark measurement to be effective, the solar cell must be isolated from all external sources of light. Light IV measurements require a similar setup with a light source establishing AM0 conditions onto the cell.

A block diagram of the test equipment is shown in Figure 6.1. The solar simulator setup is shown in Figure 6.2. An HP-6626A programmable power supply maintains and varies voltage across the cell and is controlled by a personal computer. The power supply is configured such that channels 1 and 2 outputs are connected to the reference cell, and channels 3 and 4 outputs are connected to the current cell under test.

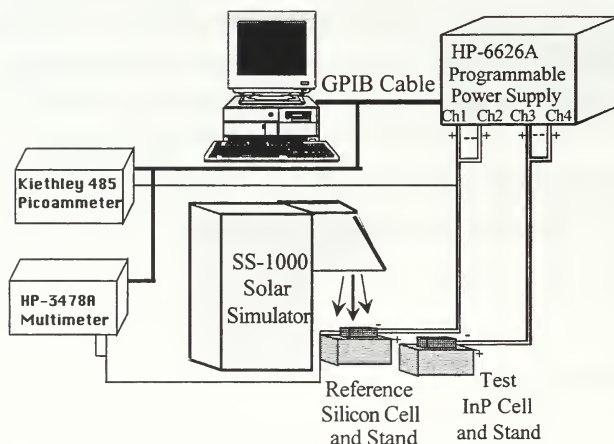


Figure 6.1 Block Diagram of Test Equipment Including the Solar Simulator, Test Cell, Reference Cell, Power Supply, Meters, and PC.

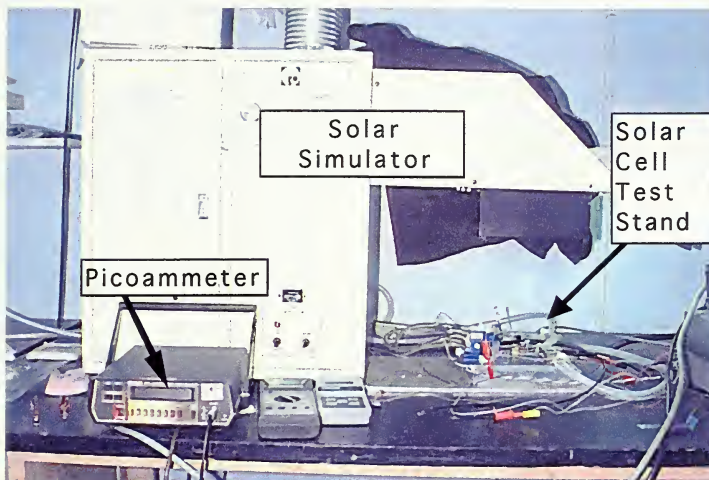


Figure 6.2 Experimental Setup Showing the Solar Simulator, Kiethley Picoammeter, and the Cell Test Stand.

An HP-3478A Multimeter was used to measure cell voltage for all testing. Illuminated IV currents were read from the power supply current output. A Kiethley 485 picoammeter was used to record currents smaller than the minimum capability of the programmable power supply. The picoammeter had an upper limit of 2 mA. The dark IV measurements are typically in the range of tens of milliamps. Dark IV measurements were constructed

from two separate measurements. Smaller currents (<2 mA) were recorded with the picoammeter while higher currents were recorded with the power supply. The two instrument outputs overlapped and were combined into a single graph.

1. Solar Simulator

All Illuminated IV measurements were done at AM0 conditions using Optical Radiation Corporation’s Solar Simulator 1000 at 25°C. The solar simulator uses a xenon arc bulb to generate an AM0 spectrum closely approximating the output of the sun as shown in Figure 6.3.

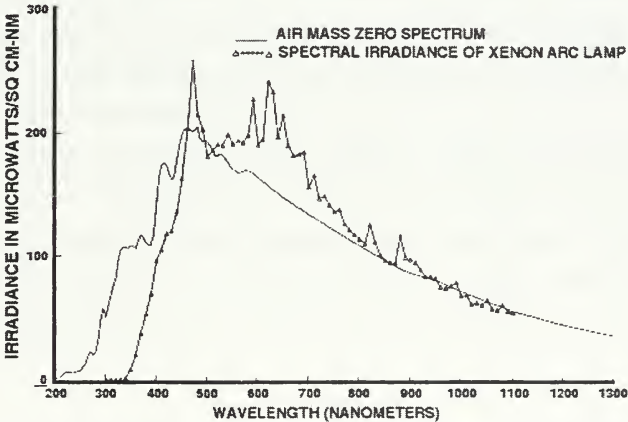


Figure 6.3 Xenon Arc Lamp and the Sun’s Spectrum at AM0 Conditions
[Ref. 3: p. 2-6]

The solar simulator output can fluctuate due to temperature changes in the bulb as the

system heats up. After a short warmup period, AM0 conditions were established by varying the output of the solar simulator. AM0 conditions were verified by performing a reference cell check with a silicon reference cell. The silicon reference cell has a known AM0 output with parameters shown in Table 6.1.

Cell Size (cm ²)	I _{sc} (mA)	V _{oc} (Volts)	P _{max} (mW)
7.68	338.264	0.6063	161.411

Table 6.1 Silicon Reference Cell AM0 Output Parameters.

The output of the solar simulator was varied until I_{sc} matched AM0 conditions in Table 6.4. Reference cell I_{sc} and temperature were checked before and after each measurement. This practice ensured a consistent AM0 output of the solar simulator. Multiple data runs on the same cell confirmed uniform reproducible and repeatable AM0 conditions.

2. Measurement Meters

The HP-6626A programmable power supply was integral to this research. The power supply would vary voltage from 0 V to V_{oc} in millivolt increments and report test cell current and voltage. Due to power supply limitations, the test circuit was biased to 4V on each side of the solar cell. The power supply tends to become unstable around 0 V when using millivolt steps. Figure 6.4 shows the power supply biasing circuit.

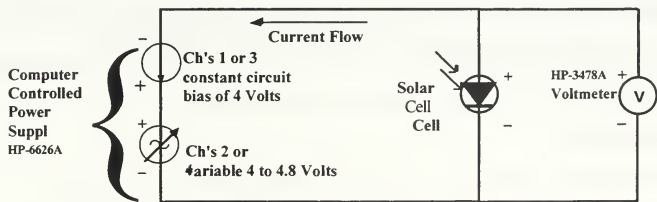


Figure 6.4 Solar Cell Biasing and Four-Point Measurement Diagram.

The power supply could only measure current accurately to the microamp range. Dark IV measurements require a minimum range of picoamps to fully utilize the data. To satisfy this requirement the picoammeter was placed inline with the power supply for dark IV measurements. Voltage readings were recorded using an HP-3478A multimeter in a four-point measurement configuration. The four-point measurement configuration shown in Figure 6.4 has separate voltage and current sensing leads. Voltage is sensed with the voltmeter on the right side of the diagram while current is sensed by the power supply on the left side of the diagram. The four-point method is superior to the two-point method where current and voltage are measured using two leads. An example of the two-point method occurs when the voltmeter is taken out of the circuit in Figure 6.4. The power supply has the capability and can be used to sense both current and voltage. In the two-point method, current flow causes voltage drops across resistance in the leads. This drop can significantly affect voltage readings. With a four-point method, current flows through one wire while voltage is sensed on the other. Current flow in one lead does not affect the voltage sensed in the other.

3. Instrument Control

Instrument control and programming was accomplished using an 80486-based personal computer (PC) running LabView™ Version 3.0. LabView™ is a graphical programming interface that allows the control and execution of measurement instruments using virtual instruments. Virtual instruments are simply computer representations of the instruments used for a particular measurement. LabView™ uses instrument drivers to control instruments via a General Purpose Interface Bus (GPIB). GPIB is a standard device language used to control one or more instruments via a single cable. The PC controls the instruments using LabView™ through the GPIB interface. PC control allows quick execution of repetitive voltage-current measurement steps.

4. Test Stand

The reference and test cells are mounted to cooling blocks under the solar simulator. The reference cell is permanently mounted while the test cell is mounted with

silver paint. Silver paint ensures good electrical conductivity between the test cell and the cooling block. Both the reference cell and test cell are maintained at $25 \pm 1^\circ\text{C}$ by a water bath running through the brass mounting stands. A thermocouple is mounted to the top of each stand to verify temperature. The solar cell touch pads are too small to attach leads. To make electrical contact with the top of the cell, micromanipulators were used to position fine metal probes on the touch pads. The bottom cell terminal connects to the power supply and instruments through the brass mounting stand. Figure 6.5 shows the test stand setup including the two micromanipulators probing a test cell.

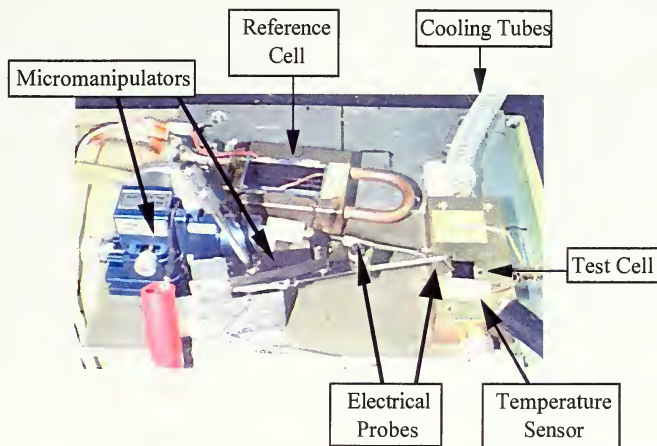


Figure 6.5 Test Stand Showing Reference Cell and Test Cell, Micromanipulators and Probes, Cooling Tubes and Temperature Sensors.

B. TEST PLAN

Illuminated and dark IV measurements were carried out on ten cells to establish individual cell performance baselines. Irradiation and annealing effects were measured and referenced to the baseline. Multiple measurements were carried out on each cell to verify initial performance characteristics. BOL characteristics for all ten cell are graphed and tabulated in Appendix B. Table 6.2 summarizes average parameter values for each cell type. Cell identification nomenclature conforms to those used by NRL and Spire Corporation.

Cell Type	I_{sc} (mA)	V_{oc} (Volts)	P_{max} (mW)	Eff (%)	FF
n/p	25.94	0.699	12.7	9.4%	0.700
p/n	20.20	0.724	10.7	7.9%	0.729

Table 6.2 BOL Average Parameter Values for n/p and p/n Type InP/Si Solar Cells.

Following initial measurements, the cells were sent to the Jet Propulsion Laboratory (JPL) in Pasadena, California for irradiation. Cells were irradiated with 1 MeV electrons to a fluence level of 5×10^{15} e-/cm² using the JPL's Dynamitron linear accelerator. This fluence level was estimated to degrade the cells by approximately 10%. This degradation level was selected to ensure an adequate margin from the baseline for annealing effects to be visible. During irradiation and throughout the remainder of the test plan, cell exposure to light sources was minimized to prevent inadvertent annealing.

Upon return from JPL, two n/p type cells and one p/n type cell were measured under AM0 conditions using the solar simulator. The simulator was allowed to heat up with the shutter closed until the test cell was mounted. Multiple illuminated IV measurements were conducted on each cell, and the results graphed. Dark IV's were conducted at the conclusion of the light IV measurements.

Two of each cell types were illuminated by the argon-ion laser shown in Figure 6.6. The laser beam was guided to the test stand via fiber-optic cable. The test stand, fiber-optic cable, and a laser illuminated test cell are shown in Figure 6.7.

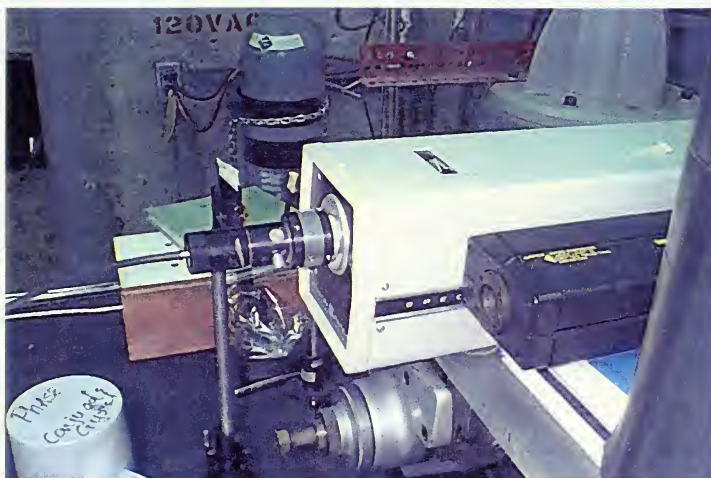


Figure 6.6 Argon-Ion Laser with Fiber-Optic Cable Attached.

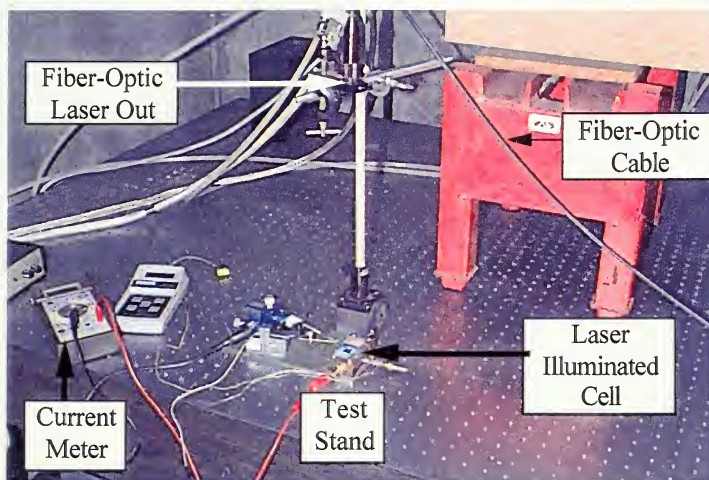


Figure 6.7 InP/Si Test Cell Under Argon-Ion Laser Illumination.

Laser beam diameter was expanded to a 1 cm diameter by adjusting the vertical distance of the fiber-optic cable to the test cell. Laser power at the test cell was determined to be 2.5 watts/cm² using a light power meter. Two of each cell type were subjected to laser illumination. The test cell was short circuited through an ammeter and temperature was recorded before and after the test. The first cell was illuminated until I_{sc} steadied in about 12 seconds. The second cell was illuminated for 124 seconds to ensure adequate time for annealing to occur. Temperature for all four laser tests remained 19.6°C. Table 6.5 summarizes the laser experiment for each cell.

Cell Number	P_i (W)	Time (s)	T (°C)	I_{sc_0} (mA)	I_{sc_f} (mA)
Spire InP/Si np cell #5803-3318-6	2.5	12	19.6	60	70
Spire InP/Si np cell #5803-3318-4	2.5	124	19.6	60	70
Spire InP/Si pn cell #5803-3324-5	2.5	12	19.2	50	70
Spire InP/Si pn cell #5803-3324-6	2.5	124	19.2	40	70

Table 6.3 Laser Experiment Test Cell Summary.

In all laser experiments, I_{sc} rose from its initial value to final value in the first ten seconds. After illumination with the laser, cells were again isolated from external sources of light. Following laser annealing, test cells were placed under the solar simulator and light IV measurements were conducted. A final set of dark IV measurements was conducted after the illuminated IV measurements.

C. RESULTS

BOL characteristics for all cells are tabulated and graphed in Appendix B. An initial degradation level was established by testing Initial illuminated IV measurements for n/p cells 1 and 3 and p/n cell 3 established the following degradation levels shown in Table 6.4.

Cell Name	I_{sc}	V_{oc}	P_{max}	Eff	FF
Spire InP/Si np cell #5803-3318-1	4.2%	4.7%	10.7%	10.7%	2.2%
Spire InP/Si np cell #5803-3318-3	6.6%	5.1%	13.0%	13.0%	2.0%
Average n/p cell parameters	5.4%	4.9%	11.9%	11.9%	2.1%
Spire InP/Si pn cell #5803-3324-3	10.0%	1.3%	12.8%	12.8%	1.9%

Table 6.4 Percentage of Cell Degradation from BOL Baseline Due to a 1 MeV Electron Fluence of $5 \times 10^{15} \text{ e-/cm}^2$.

Due to the fact that InP/Si solar cells anneal under AM0 conditions, multiple IV measurements induced recovery of the cells output following the annealing processes. Multiple illuminated IV measurements were performed on the cells in Table 6.4. All performance parameters experienced some recovery. Table 6.5 lists the percentage of degradation recovered for cells tested in the solar simulator.

Cell Name	I_{sc}	V_{oc}	P_{max}	Eff	FF
Spire InP/Si np cell #5803-3318-1	103%	33%	72%	72%	104%
Spire InP/Si np cell #5803-3318-3	92%	19%	67%	67%	113%
Spire InP/Si pn cell #5803-3324-3	17%	14%	16%	16%	17%

Table 6.5 Percentage of Cell Parameter Recovery from the Degradated Level in Inp/Si Solar Cells Tested in the Solar Simulator.

The data in Table 6.5 shows complete recovery of I_{sc} in n/p cell 1, and almost complete recovery in n/p cell 2. V_{oc} increased for both n/p cells. The high recovery of I_{sc} had a

corresponding effect on P_{max} . P_{max} recovered to three quarters of its original value for the n/p cells. P/n cell three did not exhibit the large recovery shown in the n/p type cells. The p/n cell recovered, but only about 15% of it's original performance parameter values. Irradiation caused the FF parameter for all cells to decrease only by a small amount. Because of the small decrease, a small recovery can appear to be significant. For the n/p cells above, FF increased to over 100% of it's initial degradation.

The above degradations percentages were assumed to represent the degradation of the InP/Si solar cells to be annealed by the laser. This is a reasonable assumption as the solar cells are of the same type and material, and were irradiated simultaneously to the same total dose. Assumed degradation baselines are listed in Table 6.6.

Cell Name	I_{sc} (mA)	V_{oc} (Volts)	P_{max} (mW)	Eff (%)	FF
Spire InP/Si np cell #5803-3318-4	24.54	0.67	11.5	8.5%	0.693
Spire InP/Si np cell #5803-3318-6	24.15	0.66	11.0	8.1%	0.686
Spire InP/Si pn cell #5803-3324-5	18.04	0.72	9.4	6.9%	0.722
Spire InP/Si pn cell #5803-3324-6	18.63	0.71	9.5	7.0%	0.716

Table 6.6 Assumed Cell Degradation From BOL Baseline Based on Similar Cells Tested in the Solar Simulator.

Using the assumed degradation levels from Table 6.6, percent recovery was calculated for the laser illuminated cells. Table 6.7 shows the recovery percentages.

Cell Name	I_{sc}	V_{oc}	P_{max}	Eff	FF
Spire InP/Si np cell #5803-3318-4	51%	2%	49%	49%	171%
Spire InP/Si np cell #5803-3318-6	70%	5%	46%	46%	92%
Spire InP/Si pn cell #5803-3324-5	-10%	-51%	-12%	-12%	9%
Spire InP/Si pn cell #5803-3324-6	-6%	-18%	-4%	-4%	20%

Table 6.7 Cell Recovery for Laser illuminated Test Cells from an Assumed Degradation Baseline.

The results show significant improvement in the n/p type cells. The p/n type cells showed a reduction in performance from the assumed baseline. Neither cell type exposed to laser illumination performed as well as using the solar simulator. The results of the laser annealing process could not be accurately verified due to imprecise determination of the degradation level. The actual degradation level of the laser illuminated cells is not known.

VII. CONCLUSIONS

This research intended to show the annealing effects of a continuous wave argon-ion laser on InP/Si solar cells. The degradation and annealing properties of both n/p and p/n type cells were investigated. Solar cell performance was characterized by illuminated and dark current-voltage (IV) plots. All illuminated IV measurements were done at AM0 conditions to allow direct comparison between cell types.

Five n/p and p/n InP/Si cells were characterized using illuminated and dark IV measurements. The initial measurements served as a baseline for all subsequent measurements. The ten cells were irradiated with 1 MeV electrons to a fluence level of $5 \times 10^{15} \text{ e}^-/\text{cm}^2$. After irradiation, two n/p cells and one p/n cell were tested in the solar simulator to establish the degraded cell performance parameters. Irradiation caused degradation of approximately 12% of initial P_{max} values. In addition to establishing degraded values, numerous illuminated IV measurements were performed to examine the annealing effects of the solar simulator. The n/p cells showed excellent recovery of I_{sc} ($\approx 100\%$), partial recovery of V_{oc} ($\approx 33\%$), and good recovery of P_{max} ($\approx 76\%$). The n/p cell type exhibited better annealing characteristics under the solar simulator than the p/n type cells. The p/n cells showed approximately 15% recovery in all parameters.

Two of each type cells were illuminated by an argon-ion laser with an irradiance of approximately $2.5 \text{ W}/\text{cm}^2$. One of each cell type was illuminated for 12 seconds while the second was illuminated for 124 seconds. After illumination by the laser the cells were tested in the solar simulator to determine performance parameters. Multiple illuminated IV measurements were performed to verify annealing by the laser. As with the solar simulator, the n/p cells recovered more than the p/n type cells. The n/p type cells recovered 60% of I_{sc} , 4% of V_{oc} , and 48% of P_{max} . The p/n type cells showed no recovery under the laser annealing. Laser illumination duration was a significant factor in

performance parameter recovery of the n/p type cells. Cell 4 n/p was illuminated for 124 seconds and showed no annealing of I_{sc} under multiple illuminated IV measurements. In contrast, cell 4 n/p I_{sc} shows improvement with successive measurements in the solar simulator.

The data shows photoinjection annealing has the largest effect on I_{sc} for these types of solar cells. V_{oc} exhibits less recovery for all cells as compared to I_{sc} . The combination of excellent I_{sc} recovery coupled with poor V_{oc} recovery results in some recovery of P_{max} .

In conclusion, this research verified that InP/Si solar cells irradiated to a fluence level of 5×10^{15} , anneal under AM0 sunlight. Both n/p and p/n cell types exhibit some recovery of performance parameters. Solar cell annealing with an argon-ion laser results in some power recovery of the performance parameters. The research also found that n/p type cells exhibited power recovery, while p/n type cells did not. Further research should repeat the experiment with cells degraded to a higher fluence. The 10% degradation level used in this research did not provide adequate margin to accurately verify the degradation and the recovery of the laser annealed cells. Solar cells in follow on experiments should be irradiated to a total dose that would cause at least 20% degradation. Degradation should be estimated by a quickly illuminating the cells in the solar simulator and capturing I_{sc} and V_{oc} . A quick measurement of these two parameters would provide a significant amount of degradation information while minimizing solar simulator annealing effects.

APPENDIX A. SILICON REFERENCE CELL DATA SHEET

SILICON
K6700A
SOLAR CELLS

S P E C T R O D A T A

TYPICAL ELECTRICAL PARAMETERS*

$J_{sc} = 42.5$ Milliamperes/cm²
 $J_{mp} = 39.6$ Milliamperes/cm²
 $V_{mp} = 0.500$ Volts
 $P_{mp} = 19.8$ Milliwatts/cm²
 $V_{oc} = 0.605$ Volts
 $CH = 0.77$
 Efficiency 14.6% Minimum Average
 *AMO Sunlight (135.3 mw/cm², 28°C)

RADIATION DEGRADATION*

PARAMETER	1x10 ¹³	1x10 ¹⁴	1x10 ¹⁵	1x10 ¹⁶
I_{sc}/I_{sc0}	0.97	0.95	0.86	0.75
I_{mp}/I_{mp0}	0.96	0.94	0.84	0.72
V_{mp}/V_{mp0}	0.94	0.92	0.83	0.74
V_{oc}/V_{oc0}	0.94	0.92	0.84	0.76
P_{mp}/P_{mp0}	0.90	0.85	0.71	0.53

*Fluence e/cm^2 1 MeV Electrons

THERMAL PROPERTIES

Solar Absorptance = 0.78 (CMX)
 Solar Absorptance = 0.77 (Fused Silica)
 Emittance (Normal) = 0.85 (CMX)
 Emittance (Normal) = 0.81 (Fused Silica)

WEIGHT

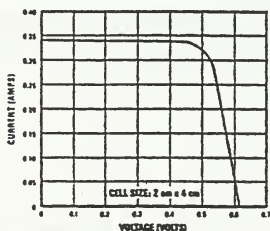
55 Milligrams/cm² (Bare)

TEMPERATURE COEFFICIENTS

$I_{sc} = +22.0$ Microamperes/cm²/°C
 $V_{mp} = -2.15$ Millivolts/°C
 $V_{oc} = -1.98$ Millivolts/°C

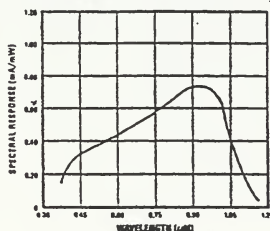
APPLICATION NOTES

TYPICAL I-V CHARACTERISTIC CURVE*



*AMO Sunlight (135.3 mw/cm², 28°C)

SPECTRAL RESPONSE



SPECTROLAB, INC.

Subsidiary of Hughes Aircraft Company

12500 Gladstone Avenue
 Sylmar, California 91342-5373
 TELEPHONE: (818) 365-4871
 TWX: 910-498-1750
 TELECOPIER: (818) 361-5102
 TLX: 182841 SPECTILUM SYLM

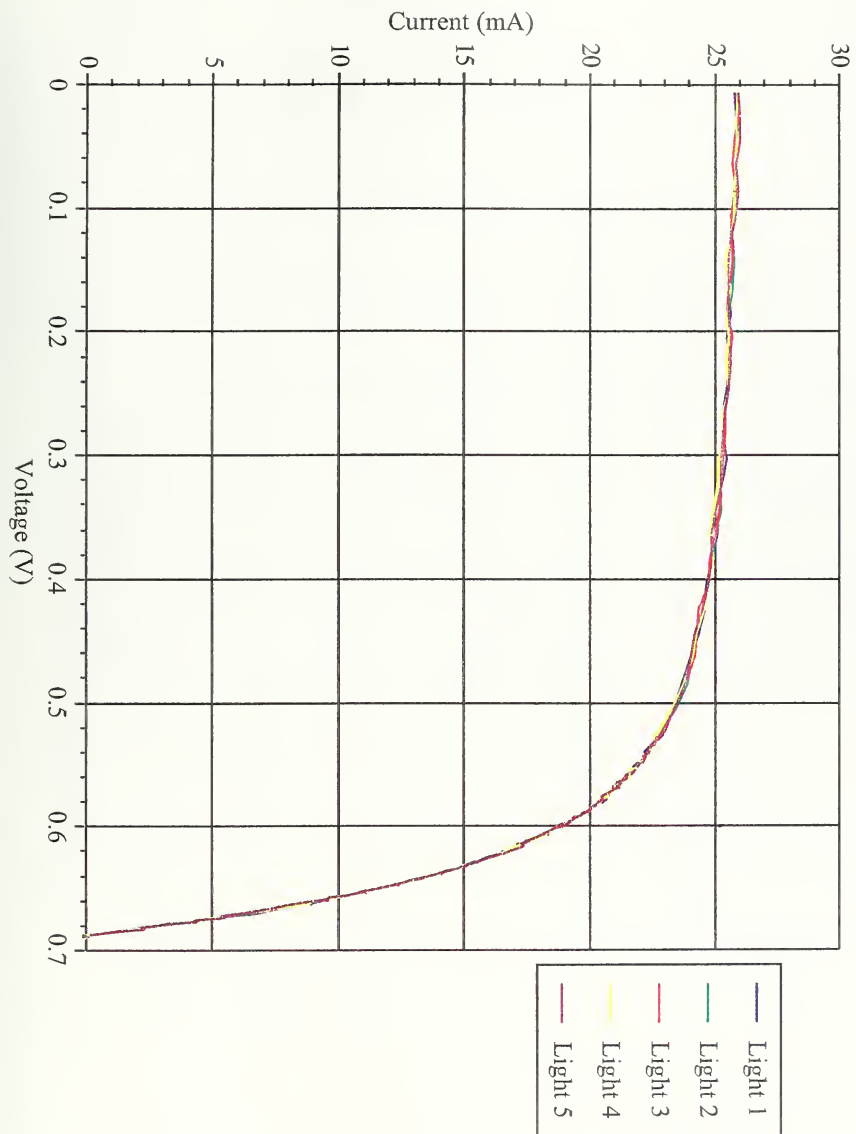
APPENDIX B. SOLAR CELL DATA PLOTS

This appendix contains tables and graphs for all data taken during the course of this research. BOL characteristics for ten cells are listed below. Three of the ten irradiated cells did not have annealing experiments performed on them. Their BOL characteristics are presented for information purposes. Each cell has three BOL graphs. The first graph contains all illuminated IV data runs. The second graph contains all dark IV data runs. The third graph contains a single illuminated IV measurement representative of the BOL characteristics of that cell. Performance parameters are also listed on the third graph.

Cell Number	I_{sc} (mA)	V_{oc} (V)	P_{max} (mW)	Eff (%)	FF
Spire InP/Si np cell #5803-3318-1	25.86	0.689	12.14	9.0	0.68
Spire InP/Si np cell #5803-3318-3	25.77	0.702	12.86	9.6	0.71
Spire InP/Si np cell #5803-3318-7	26.00	0.708	13.04	9.6	0.71
Spire InP/Si np cell #5803-3318-6	25.58	0.694	12.44	9.2	0.70
Spire InP/Si np cell #5803-3318-7	26.00	0.703	13.04	9.6	0.70
Spire InP/Si pn cell #5803-3324-3	20.09	0.722	10.16	7.5	0.70
Spire InP/Si pn cell #5803-3324-4	19.85	0.729	10.62	7.8	0.73
Spire InP/Si pn cell #5803-3324-5	20.05	0.727	10.73	7.9	0.74
Spire InP/Si pn cell #5803-3324-6	20.70	0.721	10.89	8.0	0.73
Spire InP/Si pn cell #5803-3324-7	20.29	0.723	10.70	7.9	0.73

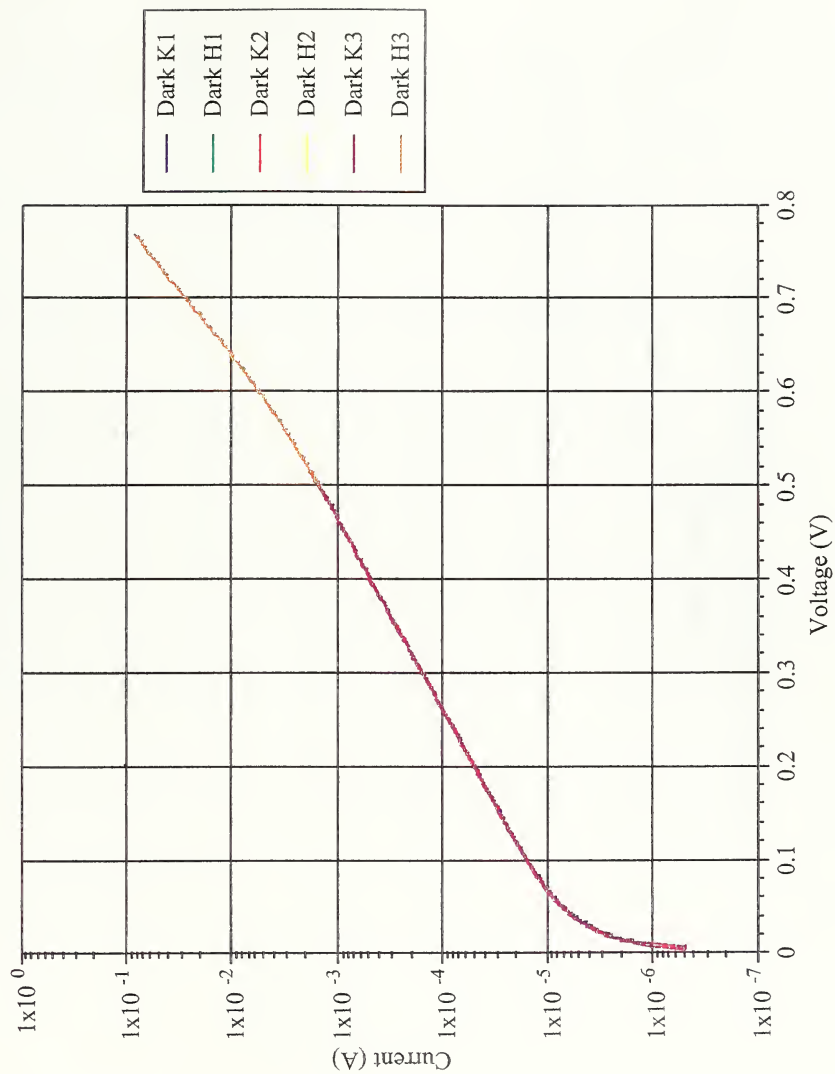
BOL Characteristics for InP/Si Solar Cells Used in This Research.

Spire InP/Si np cell #5803-3318-1 BOL Light I-V's

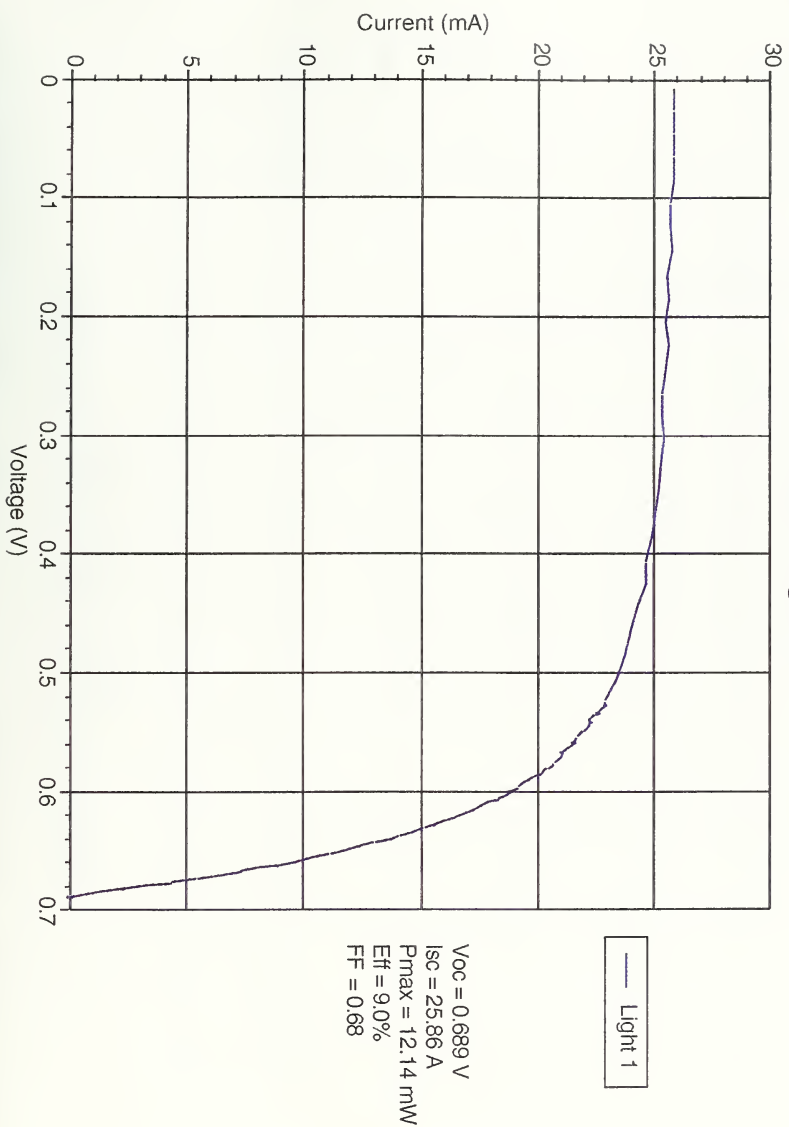


Spire InP/Si np cell #5803-3318-1

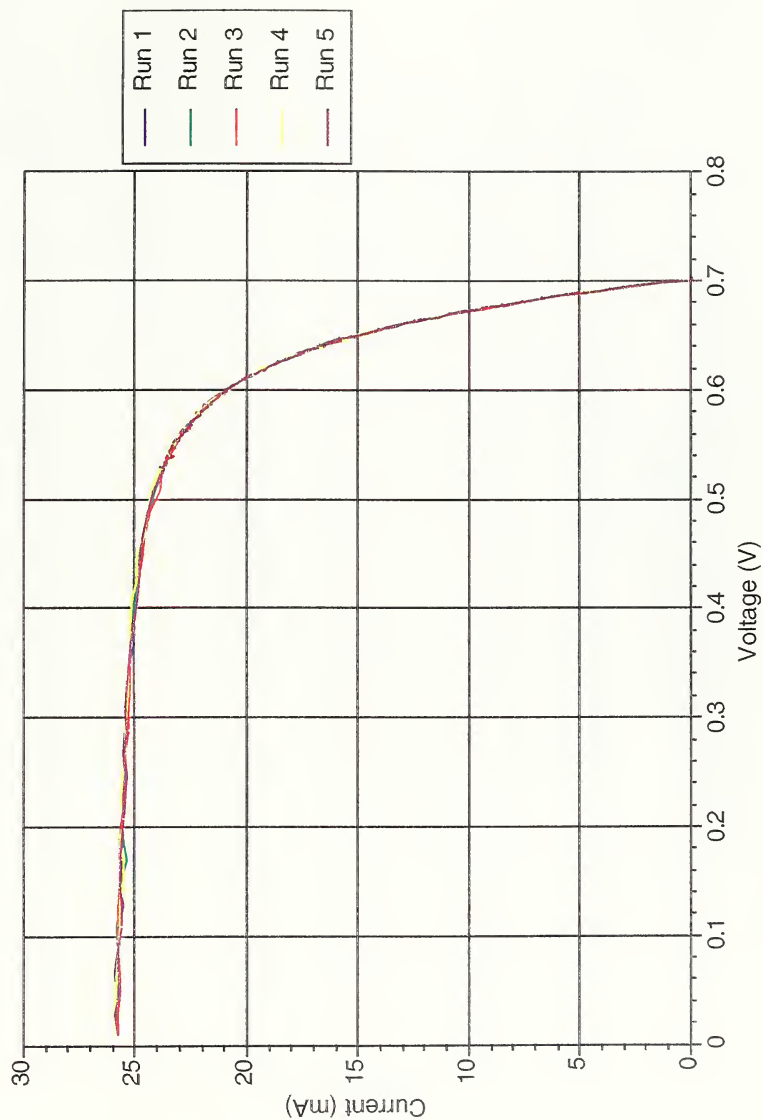
BOL Dark IV's



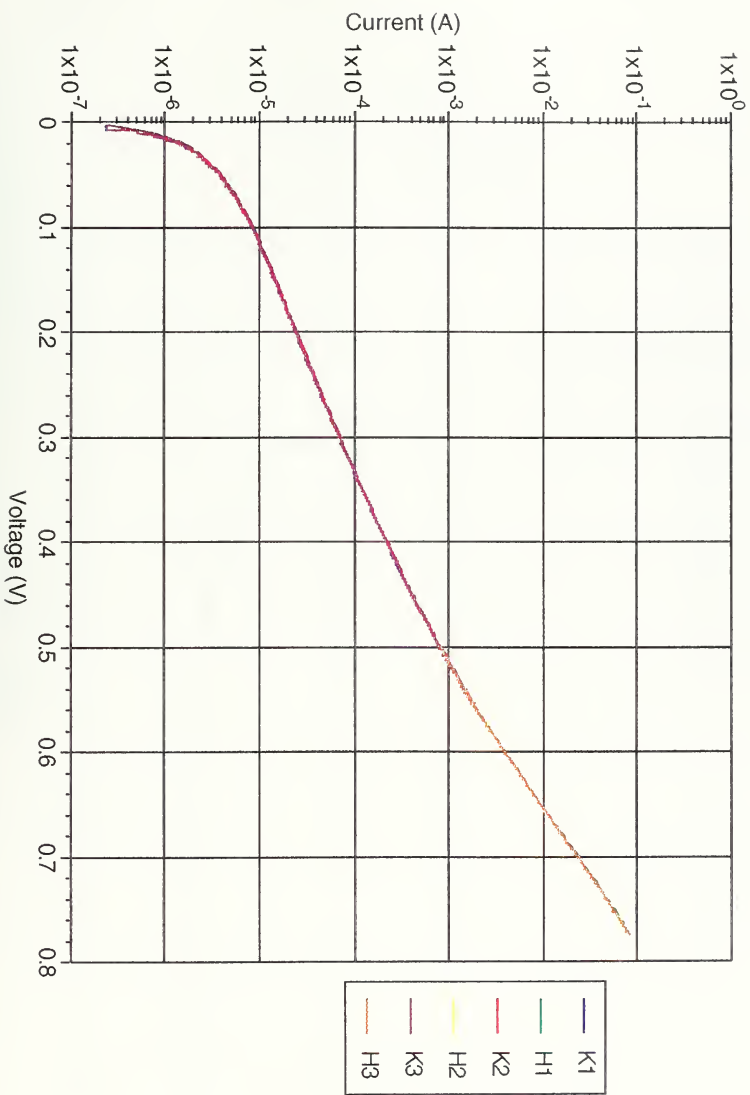
Spire InP/Si np cell #5803-3318-1 Initial Light IV



Spire InP/Si np cell #5803-3318-3 BOL Light I-V's

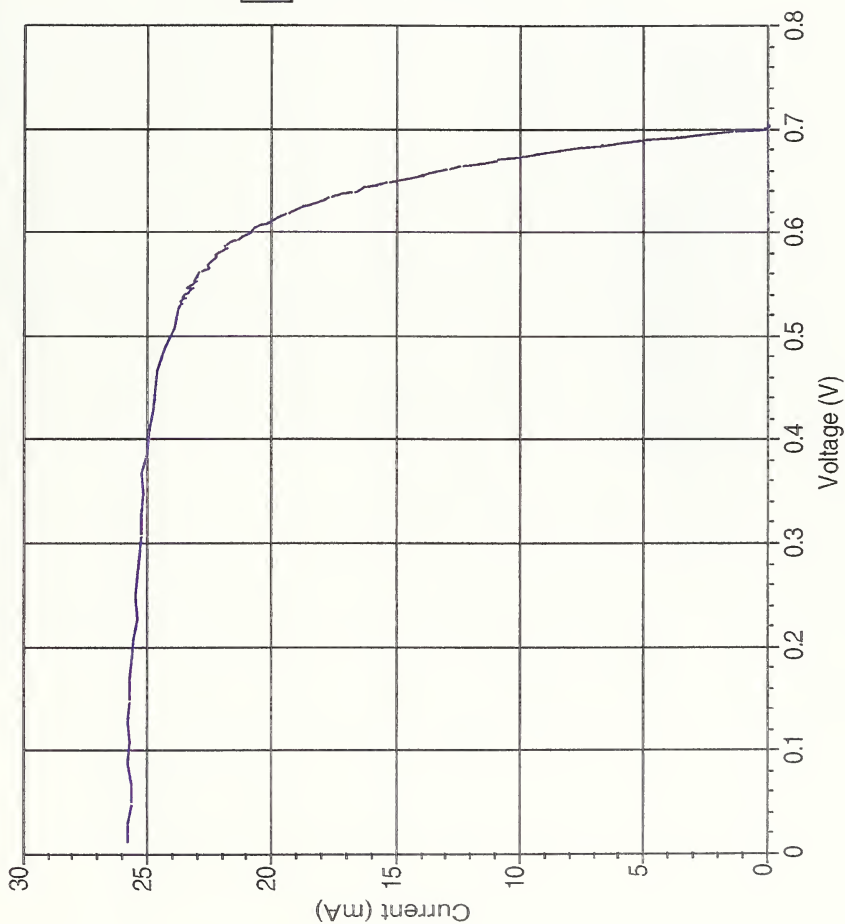


Spire InP/Si np cell #5803-3318-3 BOL Dark I-V's

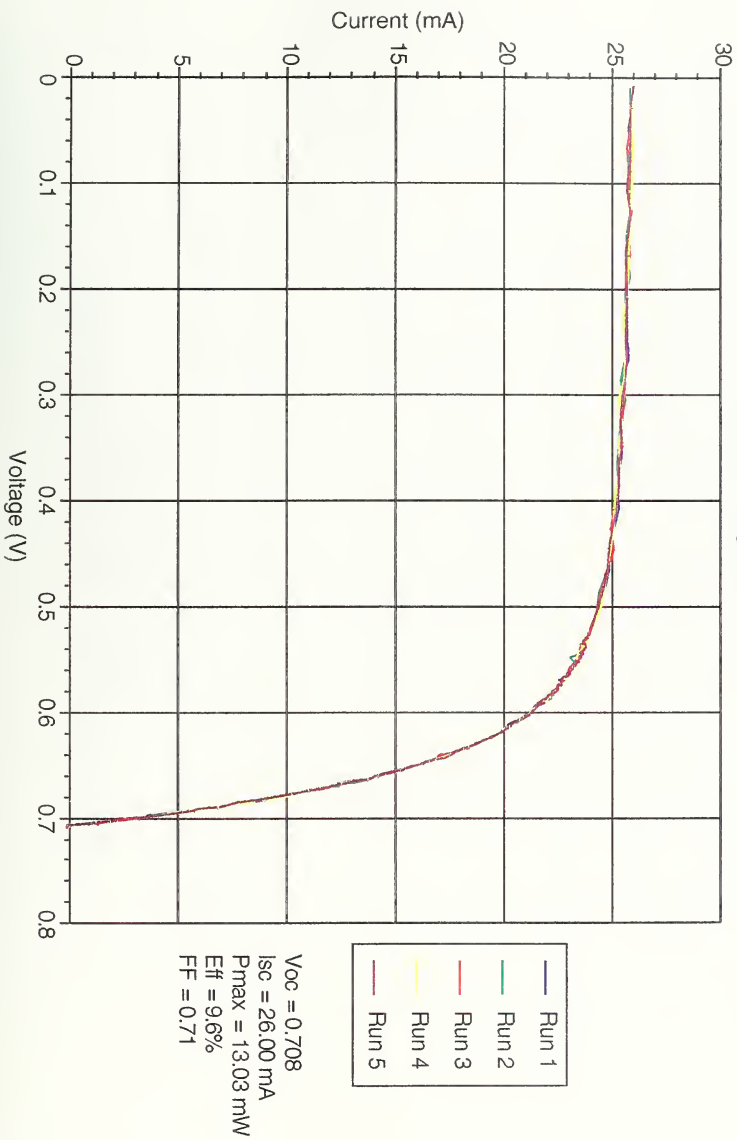


Spire InP/Si np cell #5803-3318-3

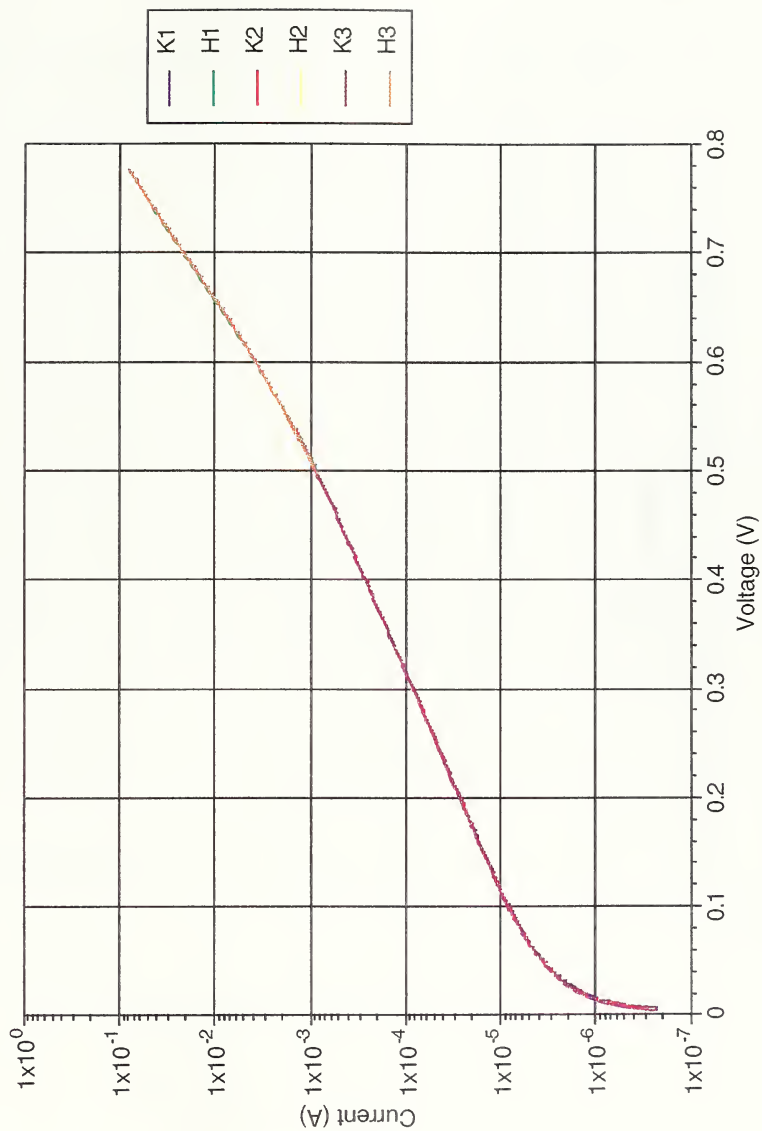
Initial Light IV



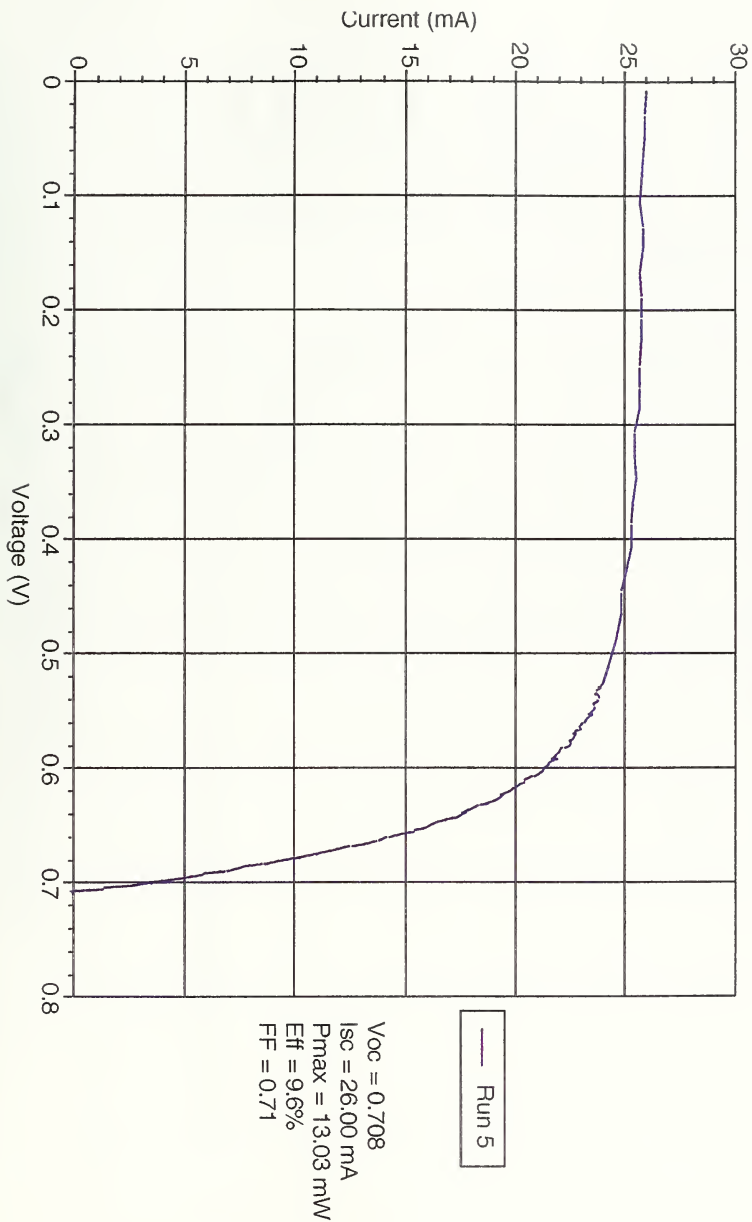
Spire InP/Si np cell #5803-3318-4 BOL Light I-V's



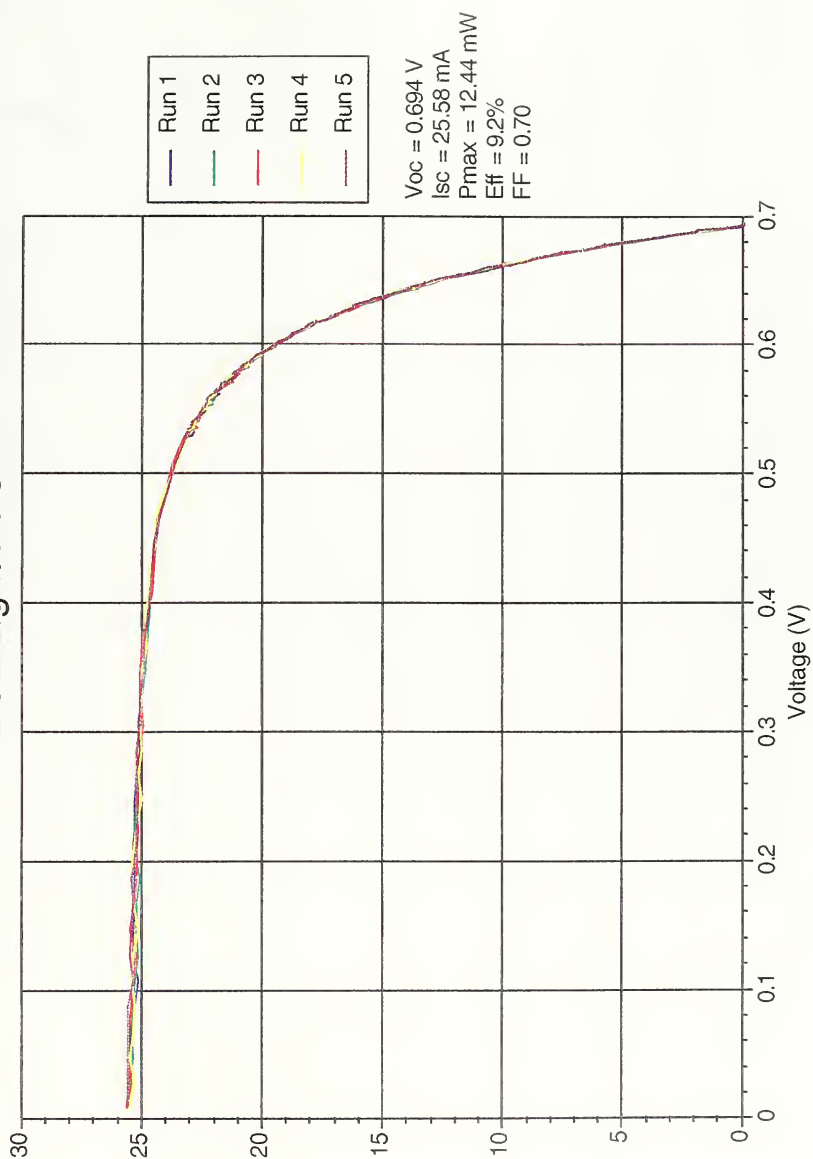
Spire InP/Si np cell #5803-3318-4 BOL Dark IV's



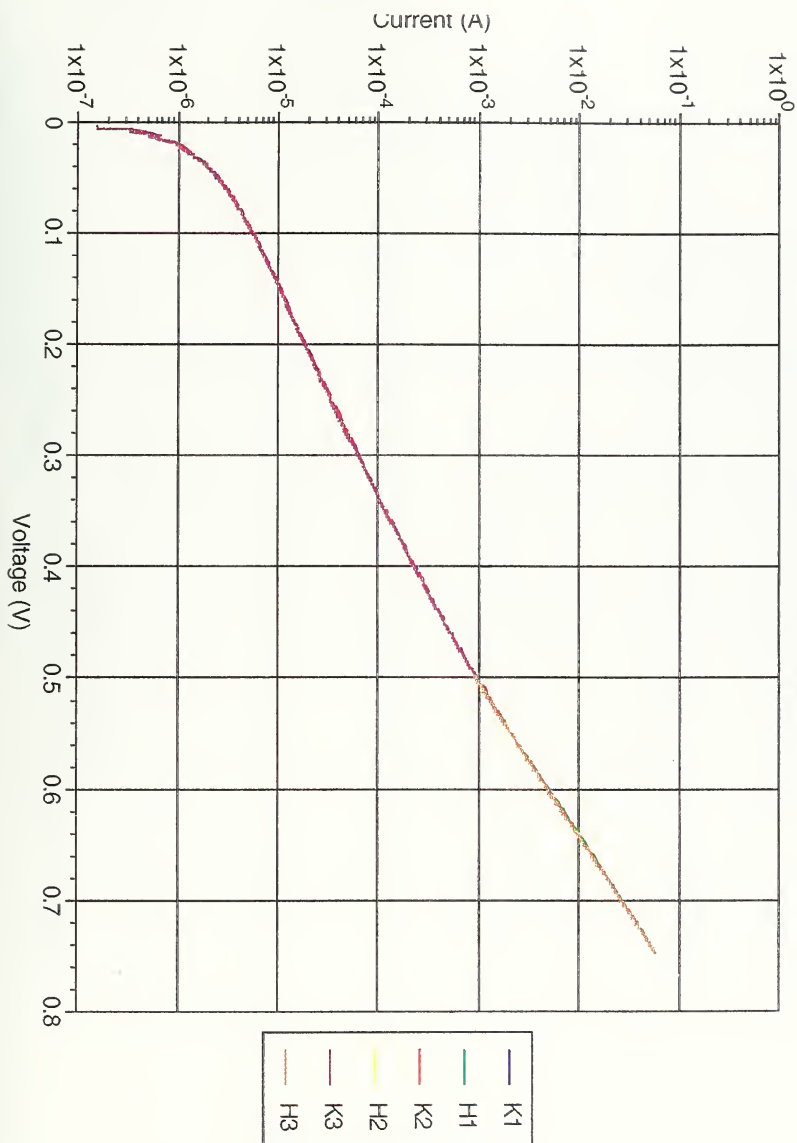
Spire InP/Si np cell #5803-3318-4 Initial Light IV



Spire InP/Si np cell #5803-3318-6 BOL Light I-V's

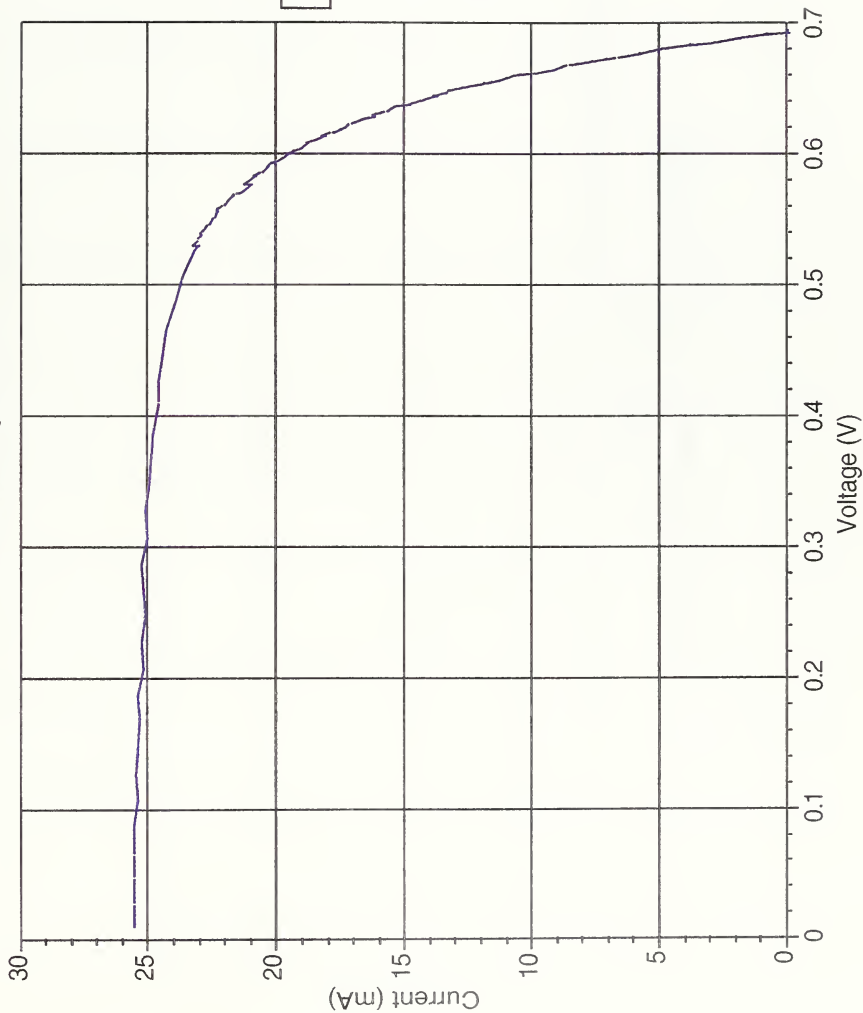


Spire InP/Si np cell #5803-3318-6 BOL Dark IV's

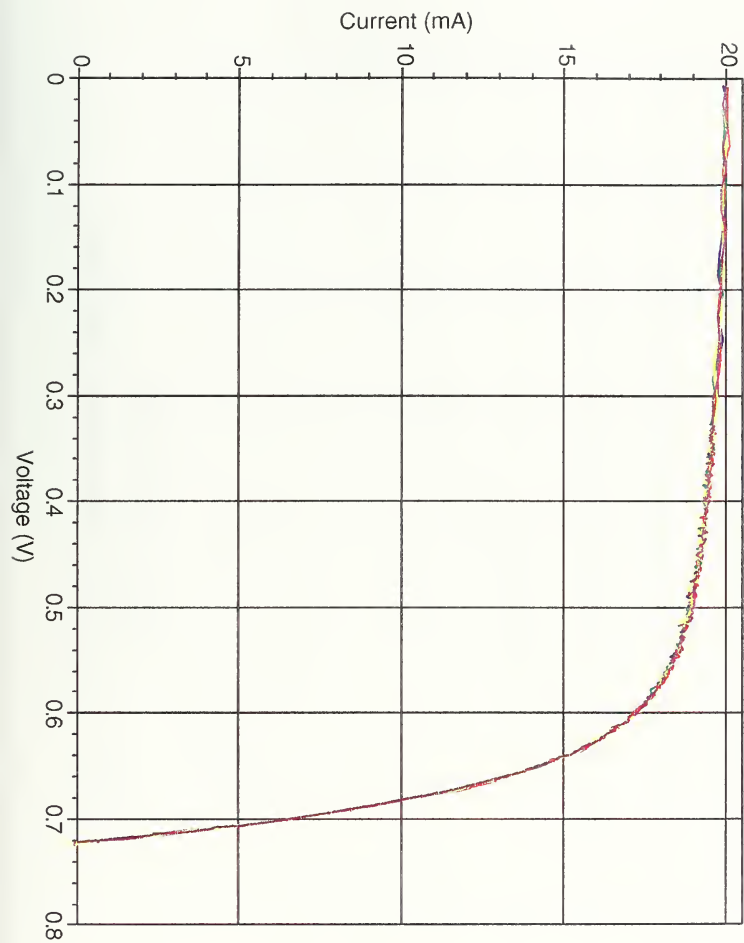


Spire InP/Si np cell #5803-3318-6

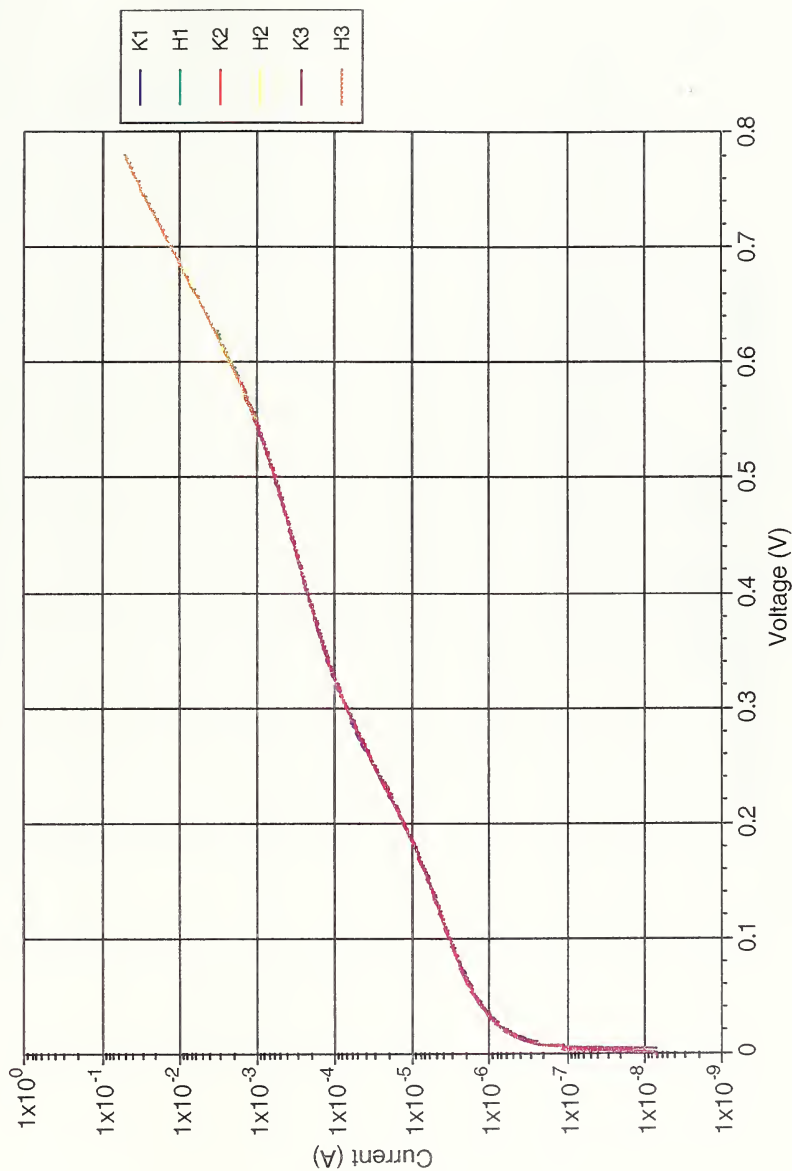
Initial Light IV



Spire InP/Si pn cell #5803-3324-3 BOL Light I-V's

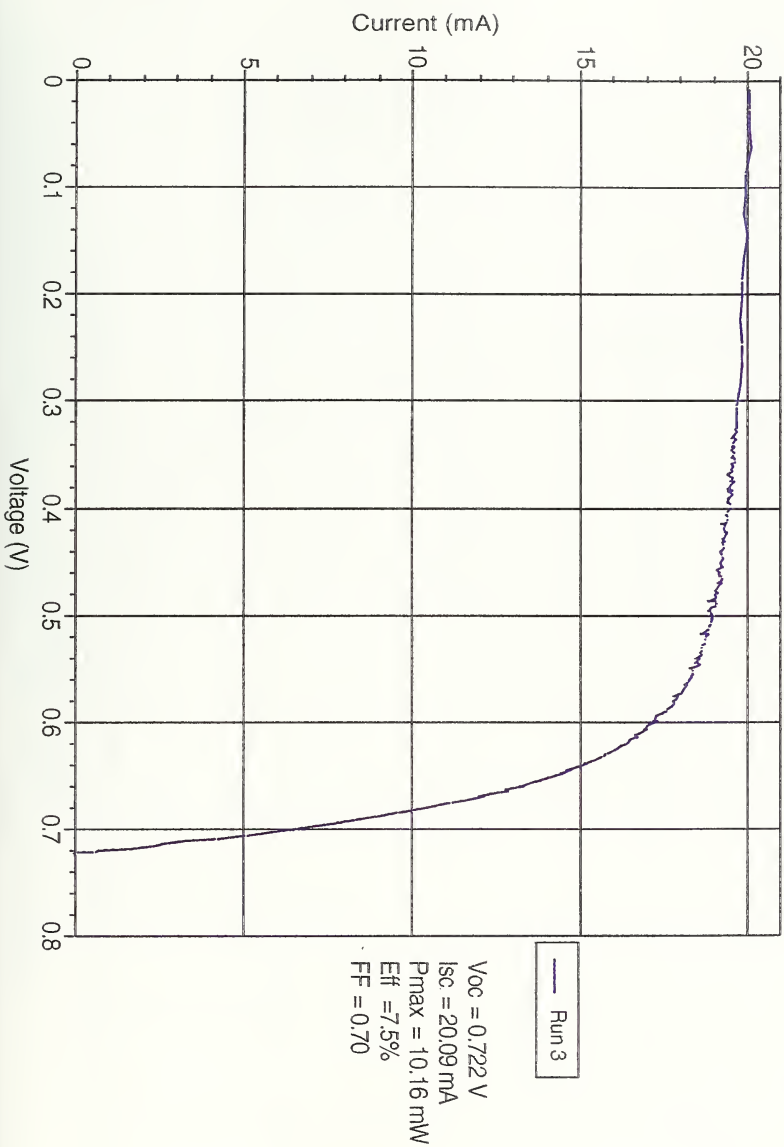


Spire InP/Si pn cell #5803-3324-3 BOL Dark IV's

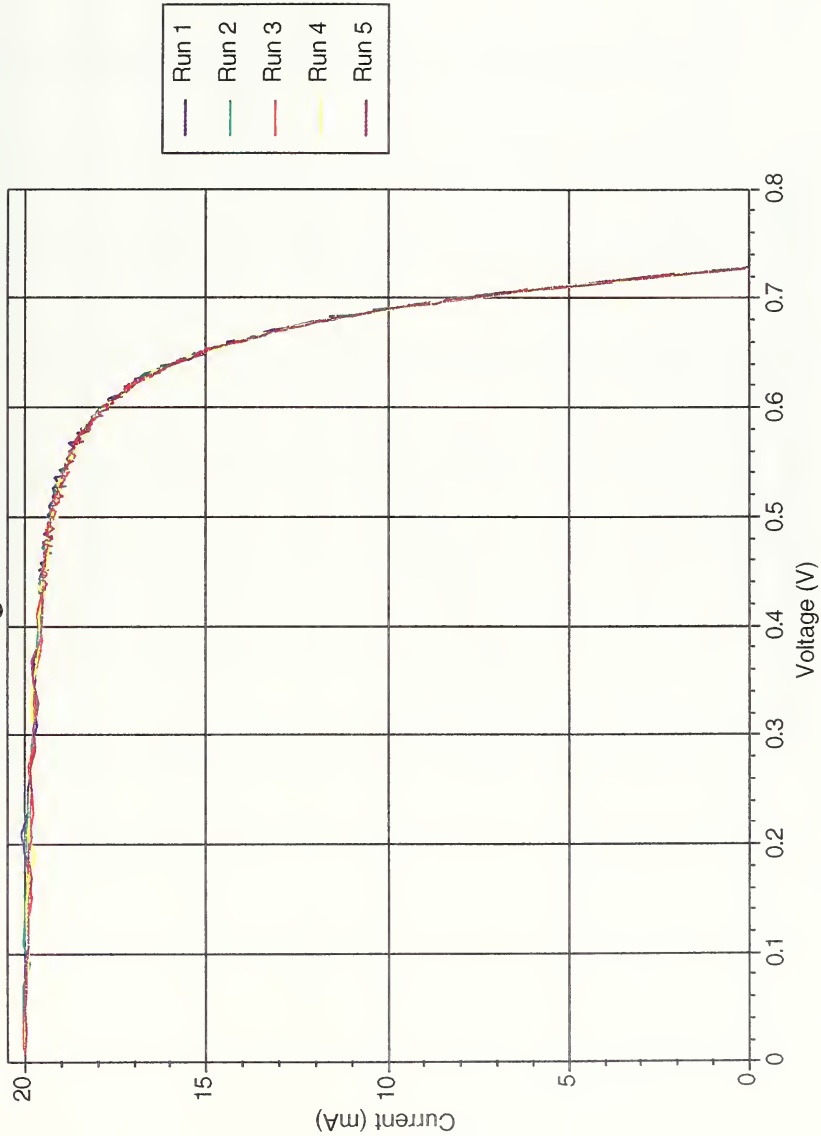


Spire InP/Si pn cell #5803-3324-3

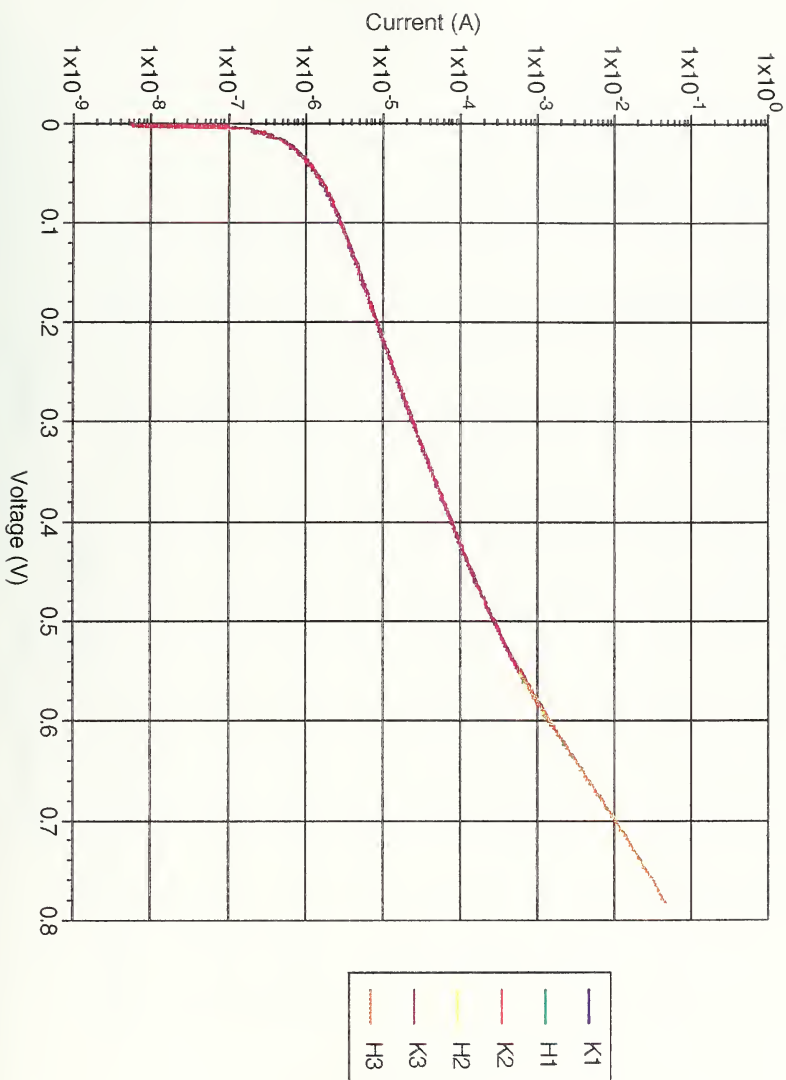
Initial Light IV



Spire InP/Si pn cell #5803-3324-5
BOL Light I-V's

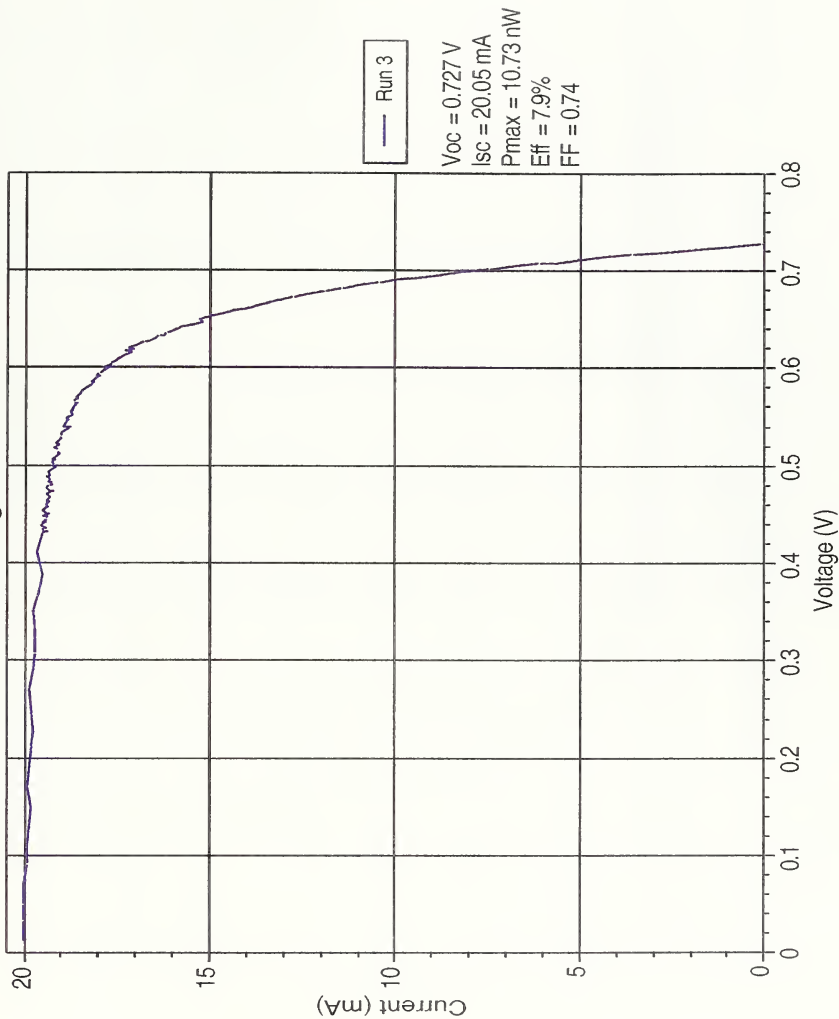


Spire InP/Si pn cell #5803-3324-5 BOL Dark IV's

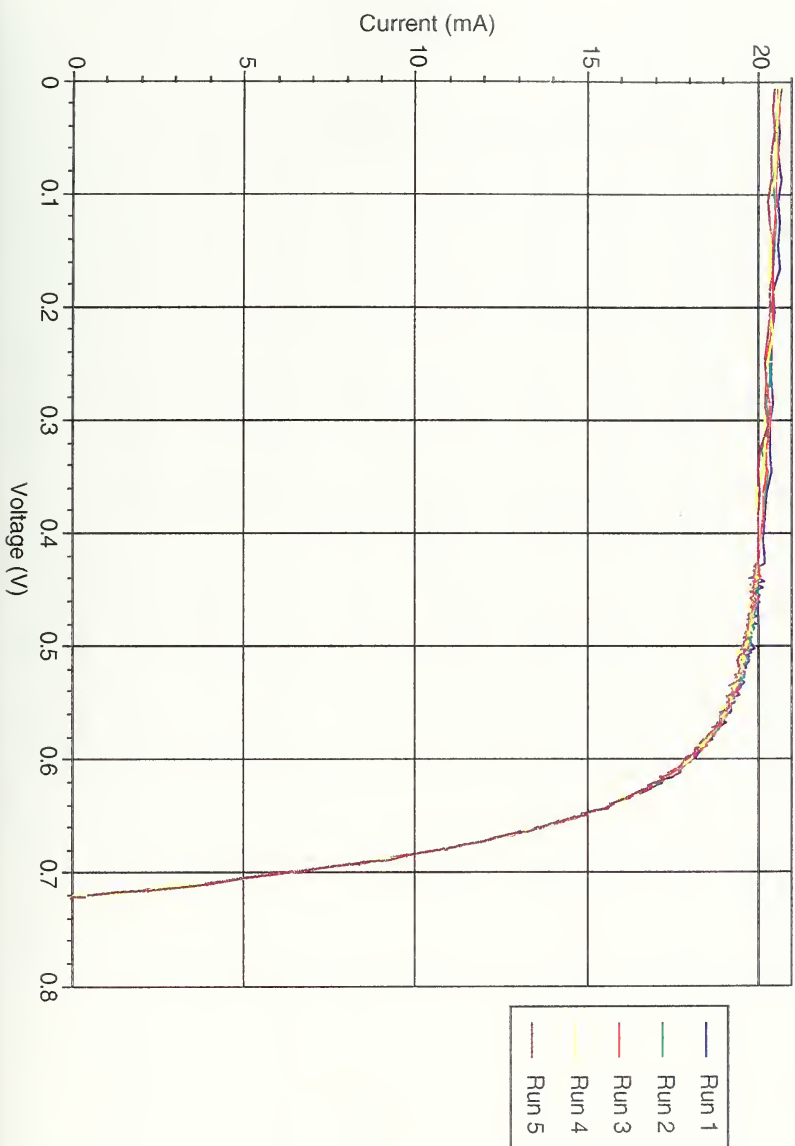


Spire InP/Si pn cell #5803-3324-5

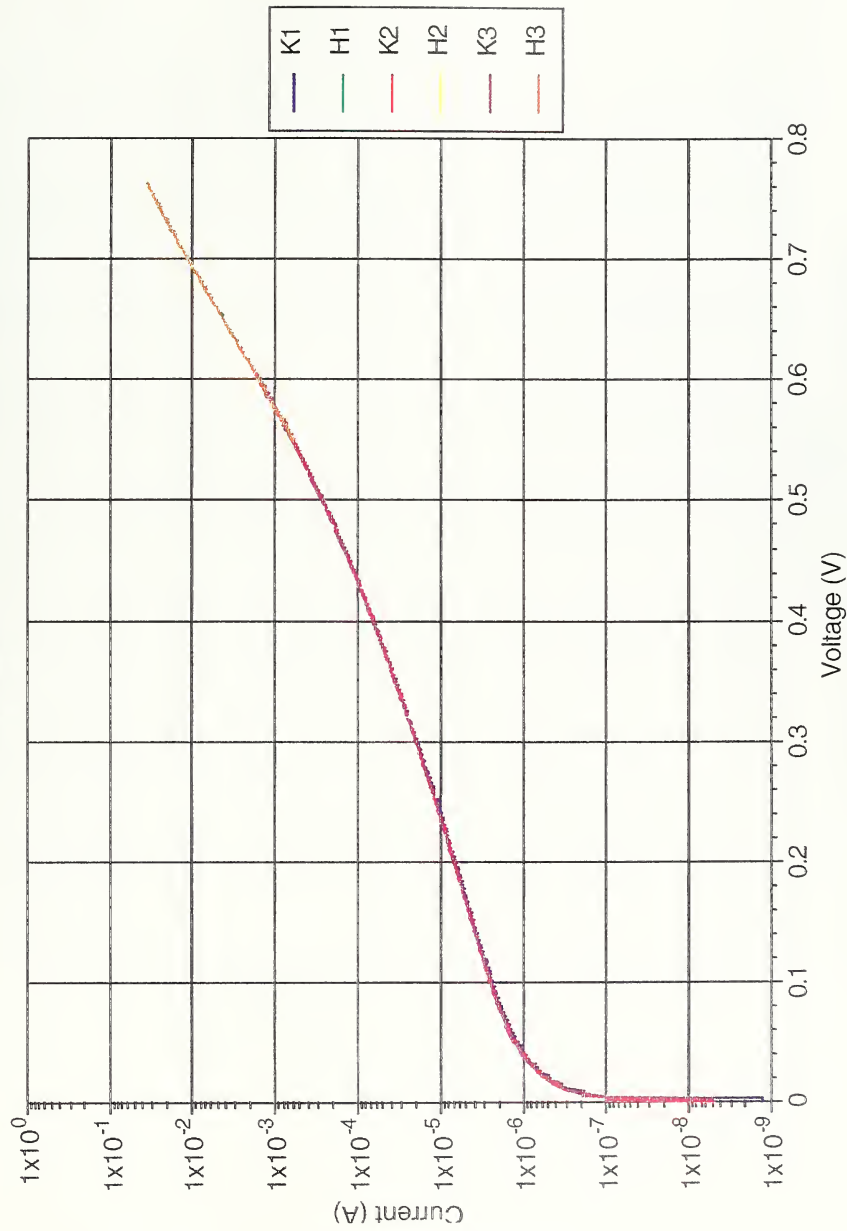
Initial Light IV



Spire InP/Si pn cell #5803-3324-6 BOL Light I-V's

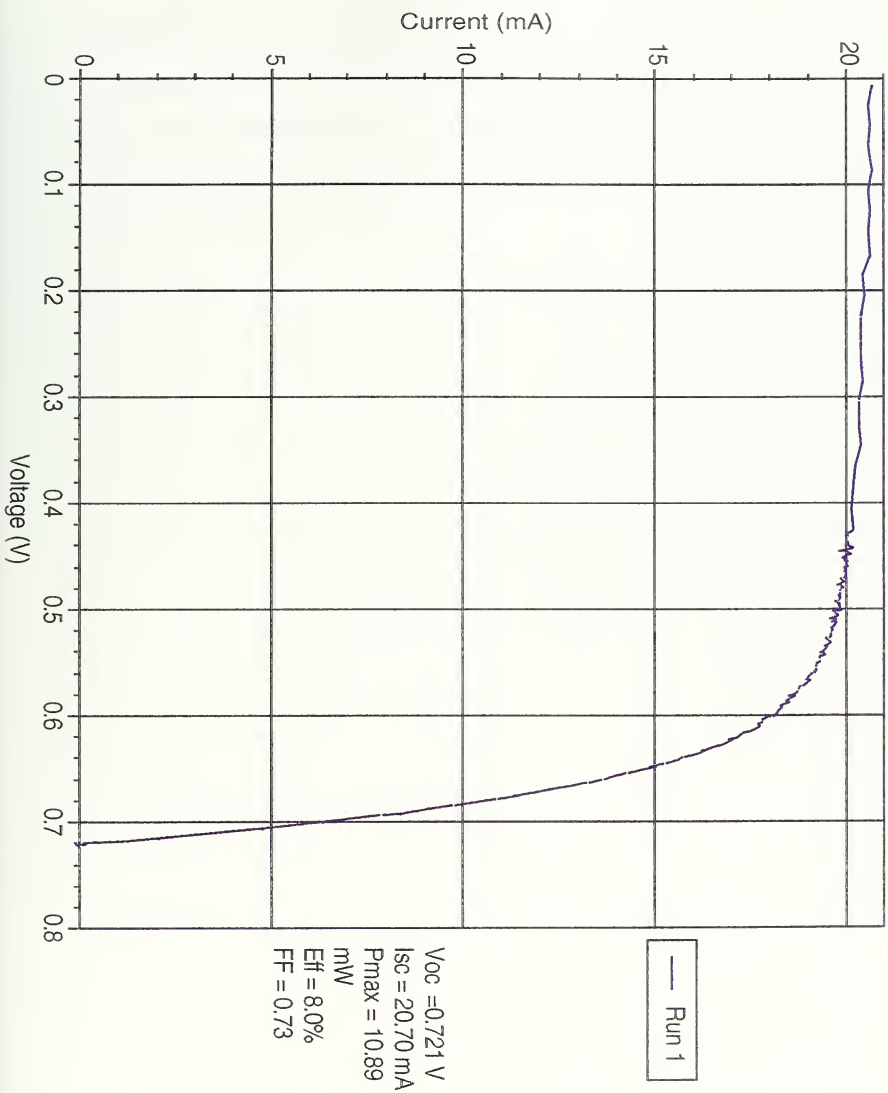


Spire InP/Si pn cell #5803-3324-6
BOL Dark IV's



Spire InP/Si pn cell #5803-3324-6

Initial Light IV



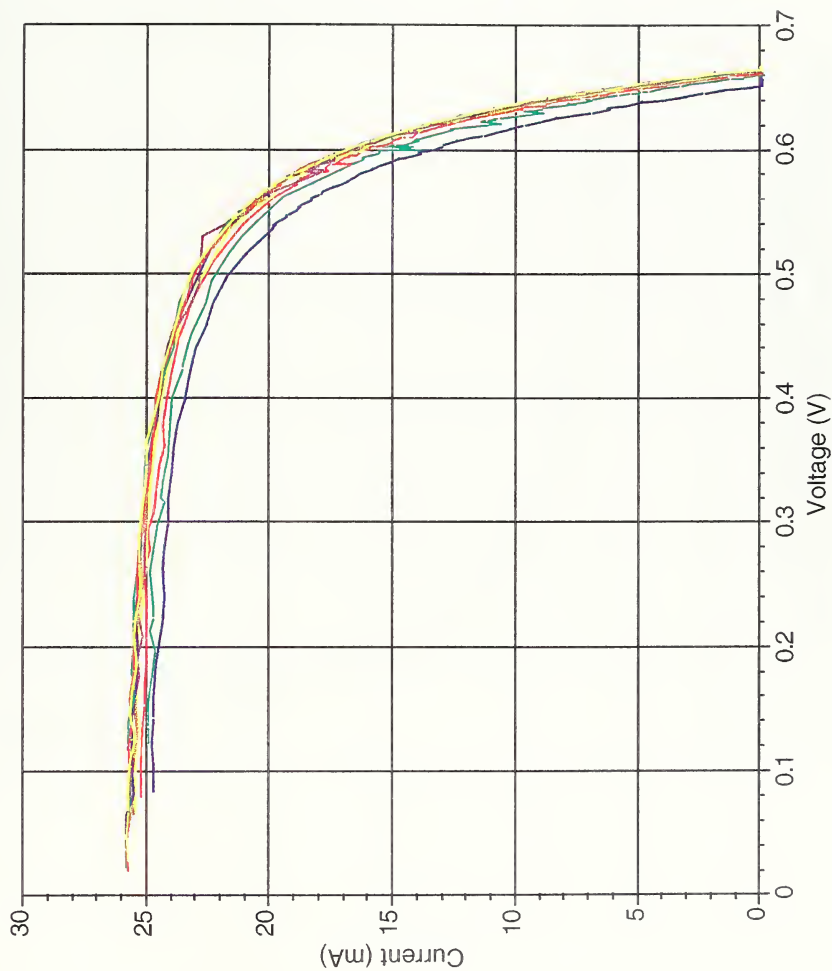
The remainder of this appendix contains a summary tables and graphs of data runs for each annealed solar cell. Data Run 0 is BOL illuminated IV values and is entered at the beginning and end of the table to allow easy comparison of annealing data to BOL data. Also percent degradation from BOL values and percent recovery from the degraded level are presented for each parameter. Illuminated IV, dark IV, and comparison IV data graphs for each cell follow their respective tables.

Spire InP/Si np cell #5803-3318-1

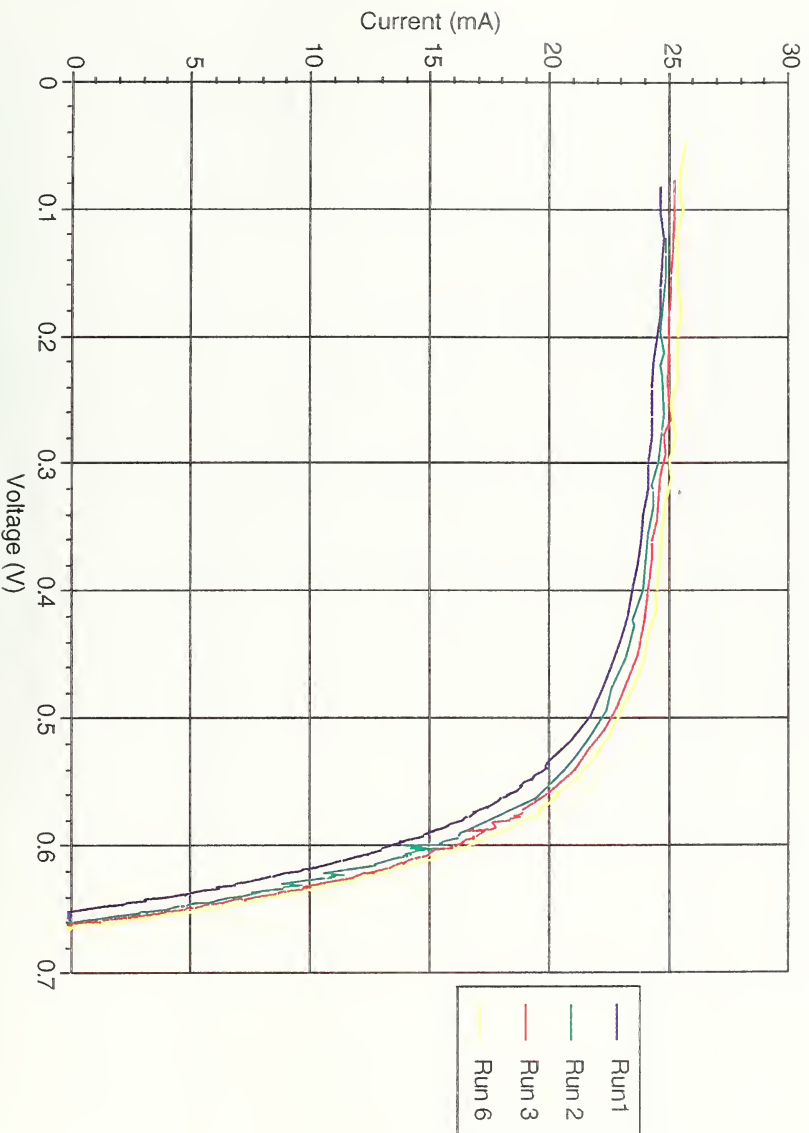
Cell 1	Isc	Voc	Pmax	Eff	FF
0	25.86	0.69	12.0	9.0%	0.681
1	24.77	0.66	10.8	8.0%	0.666
2	24.91	0.66	11.2	8.3%	0.679
4	25.89	0.66	11.3	8.4%	0.666
4	25.62	0.66	12.0	8.9%	0.707
6	25.62	0.66	12.0	8.9%	0.707
6	25.77	0.67	11.6	8.0%	0.679
7	25.81	0.67	11.7	8.6%	0.681
8	25.81	0.67	11.7	8.7%	0.683
9	25.77	0.67	11.7	8.7%	0.682
10	25.82	0.67	11.7	8.7%	0.683
11	25.89	0.67	11.7	8.7%	0.666
12	25.89	0.67	11.8	8.7%	0.681
13	25.77	0.67	11.8	8.7%	0.683
14	25.89	0.67	11.7	8.7%	0.682
15	25.89	0.67	11.8	8.7%	0.682
0	25.86	0.69	12.0	9.0%	0.681
Percent Degradation	4.2%	4.7%	10.7%	10.7%	2.2%
Percent Recovery	103%	33%	72%	72%	104%

Spire InP/Si np cell #5803-3318-1

Post Rad S.S. Light IV's

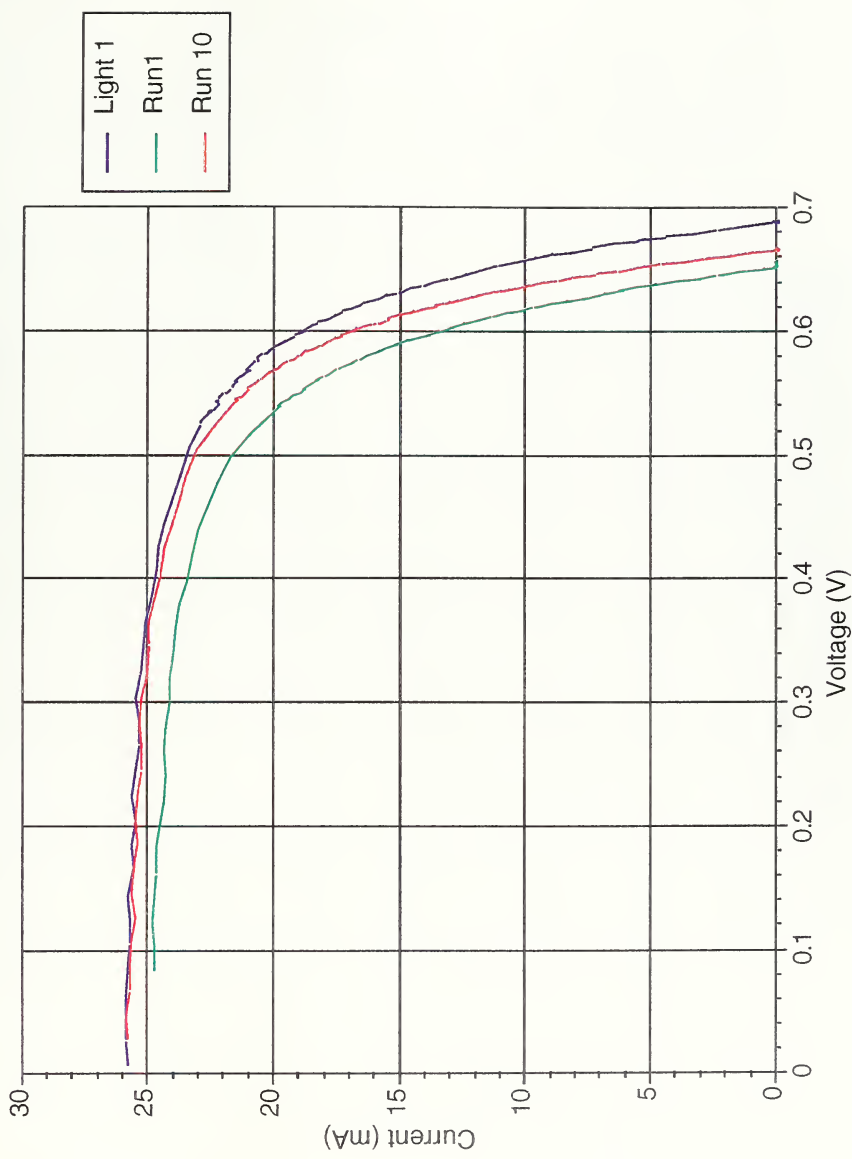


Spire InP/Si np cell #5803-3318-1 Post Rad S.S. Light IV's

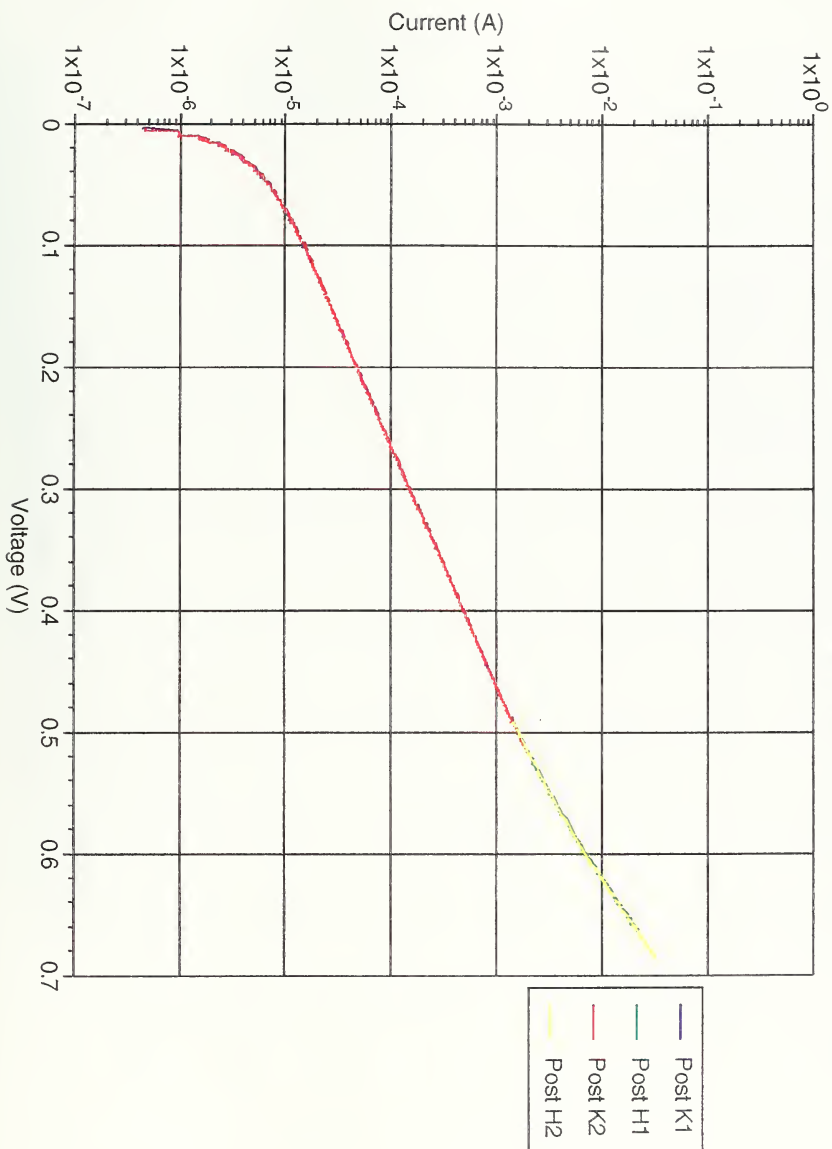


Spire InP/Si np cell #5803-3318-1

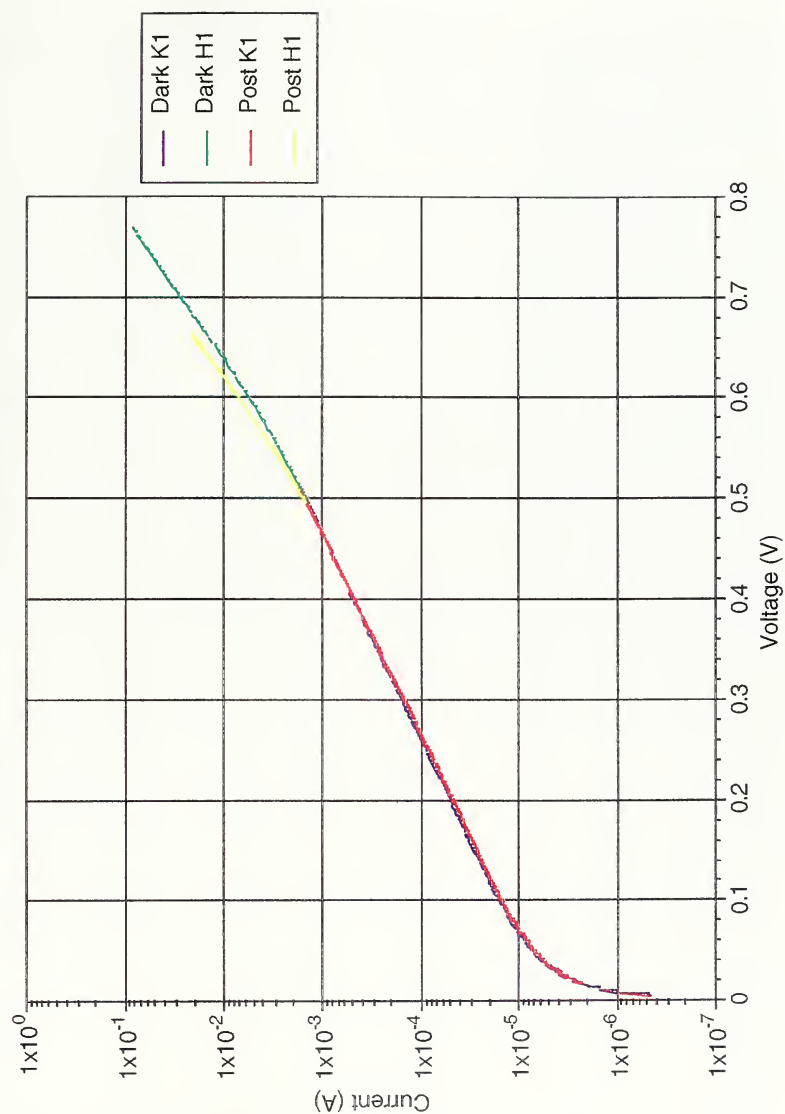
Comparison Light I-V's



Spire InP/Si np cell #5803-3318-1 Post Rad S.S. Annealed Dark IV's



Spire InP/Si np cell #5803-3318-1 Post Rad S.S. Annealed Dark IV's

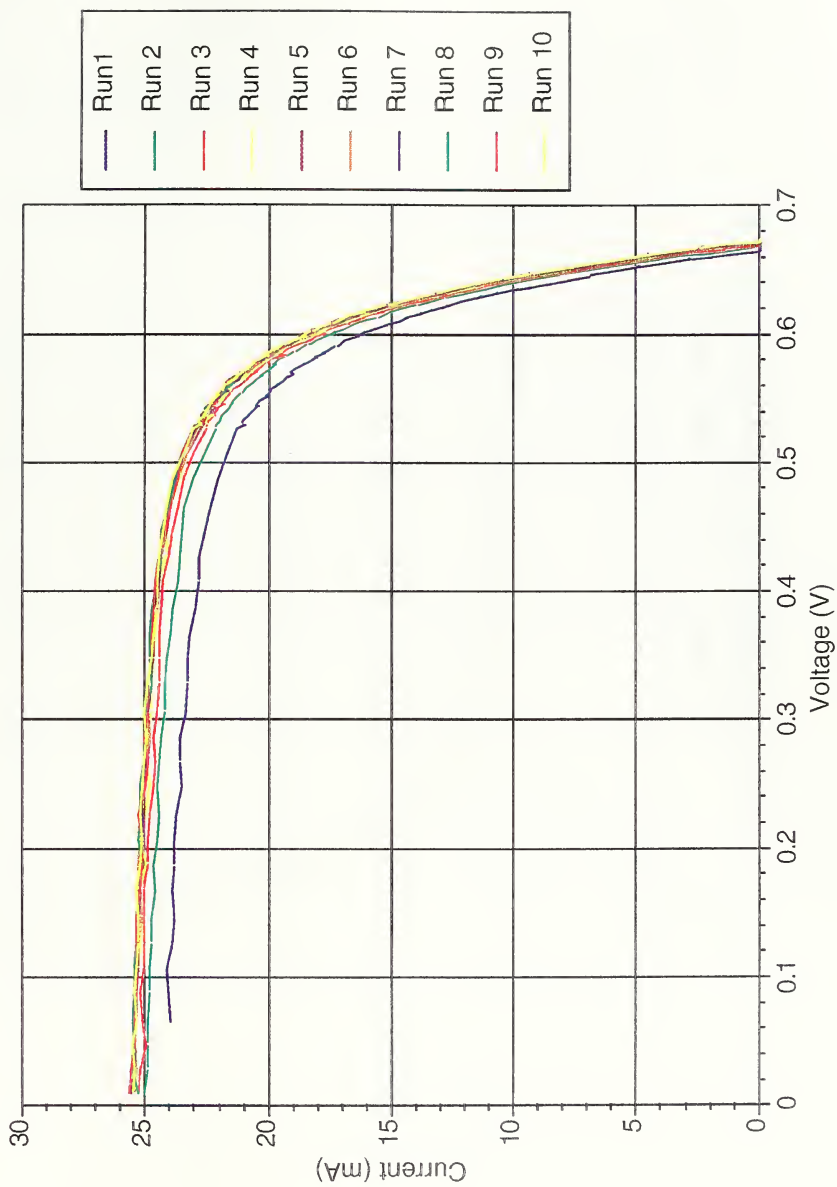


Spire InP/Si np cell #5803-3318-3

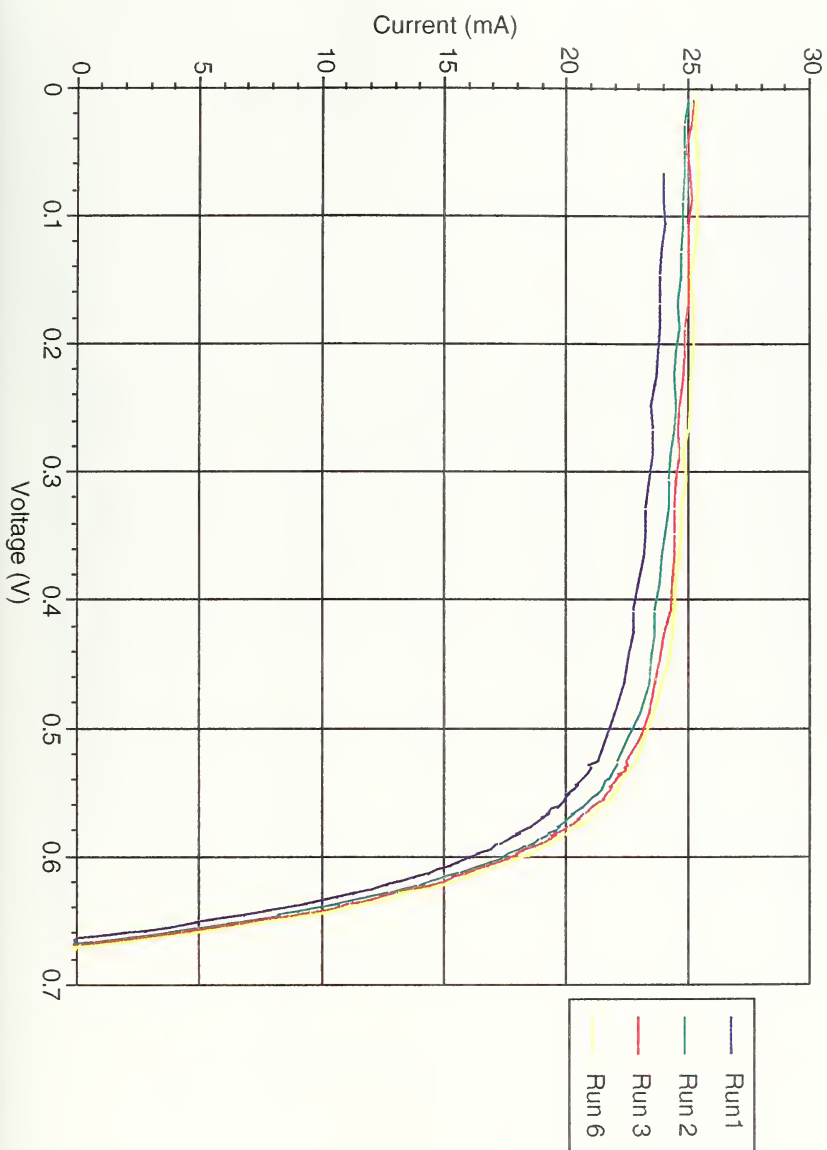
Cell 3	Isc	Voc	Pmax	Eff	FF
0	25.77	0.70	12.9	9.5%	0.711
1	24.08	0.67	11.2	8.3%	0.697
2	25.03	0.67	11.7	8.7%	0.712
4	25.28	0.67	12.3	8.3%	0.710
4	25.41	0.67	12.1	8.3%	0.710
5	25.49	0.67	12.1	9.0%	0.710
6	25.46	0.67	12.2	9.0%	0.710
7	25.54	0.67	12.2	9.0%	0.709
8	25.46	0.67	12.2	9.0%	0.713
9	25.62	0.67	12.2	9.0%	0.711
10	25.46	0.67	12.2	9.0%	0.710
11	25.46	0.67	12.2	9.0%	0.710
12	25.61	0.67	12.3	9.1%	0.713
13	25.61	0.67	12.2	9.0%	0.710
13	25.61	0.67	12.3	9.1%	0.712
15	25.62	0.67	12.2	9.0%	0.710
16	25.50	0.67	12.3	9.1%	0.710
17	25.46	0.67	12.3	9.1%	0.710
18	25.74	0.67	12.3	9.1%	0.708
19	25.65	0.67	12.3	9.1%	0.710
20	25.64	0.67	12.3	9.1%	0.713
0	25.74	0.70	12.9	9.5%	0.711
Percent Degradation	6.6%	5.1%	13.0%	13.0%	2.0%
Percent Recovery	92%	19%	67%	67%	113%

Spire InP/Si np cell #5803-3318-3

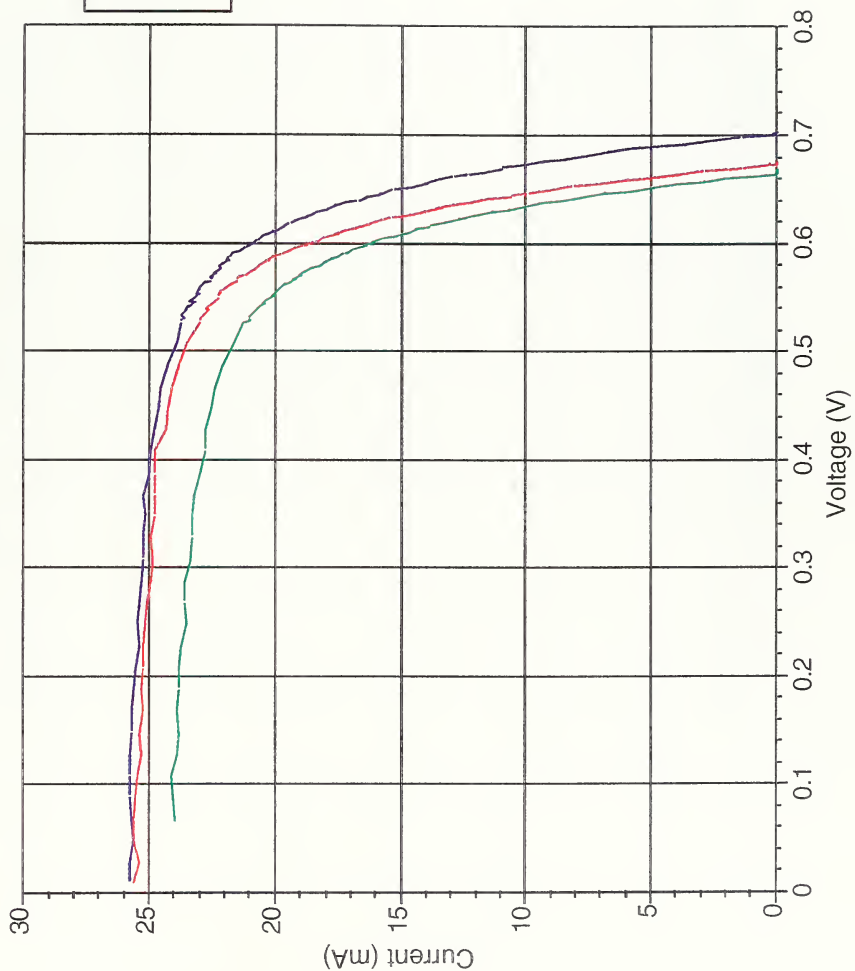
Post Rad S.S. Light IV's



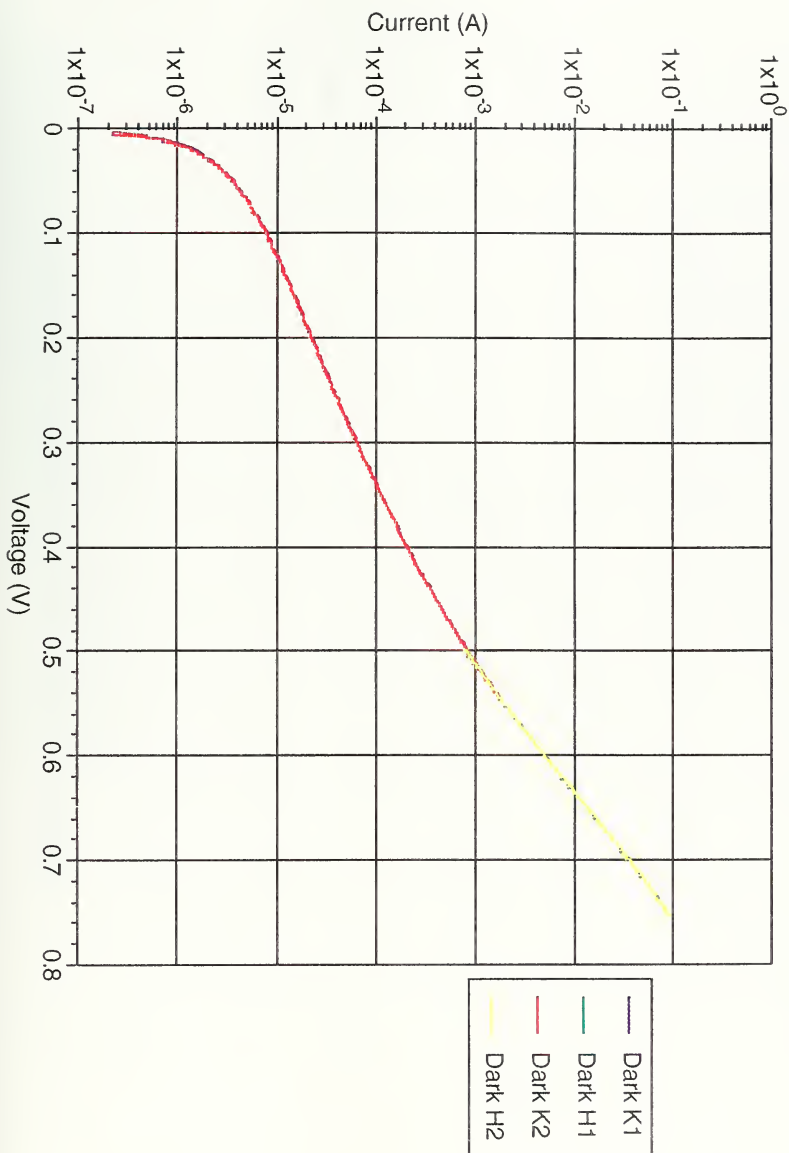
Spire InP/Si np cell #5803-3318-3 Post Rad S.S. Light IV's



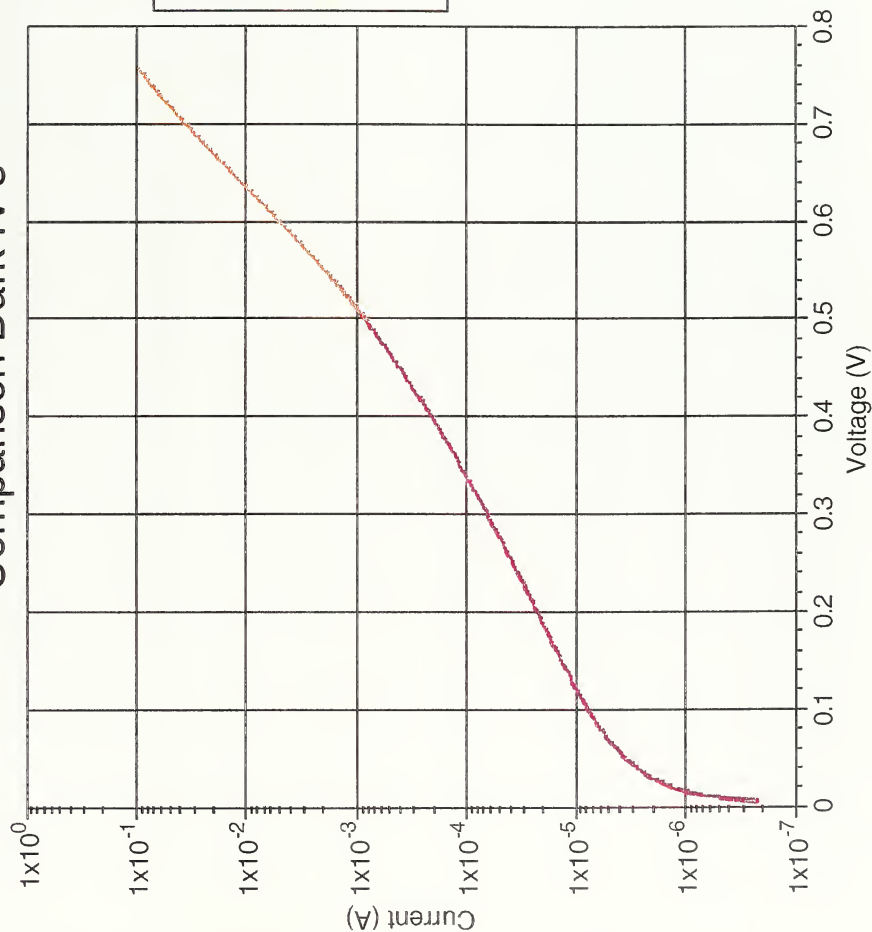
Spire InP/Si np cell #5803-3318-3 Comparison Light I-V's



Spire InP/Si np cell #5803-3318-3 Post Irradiation-S.S. Annealed Dark IV's



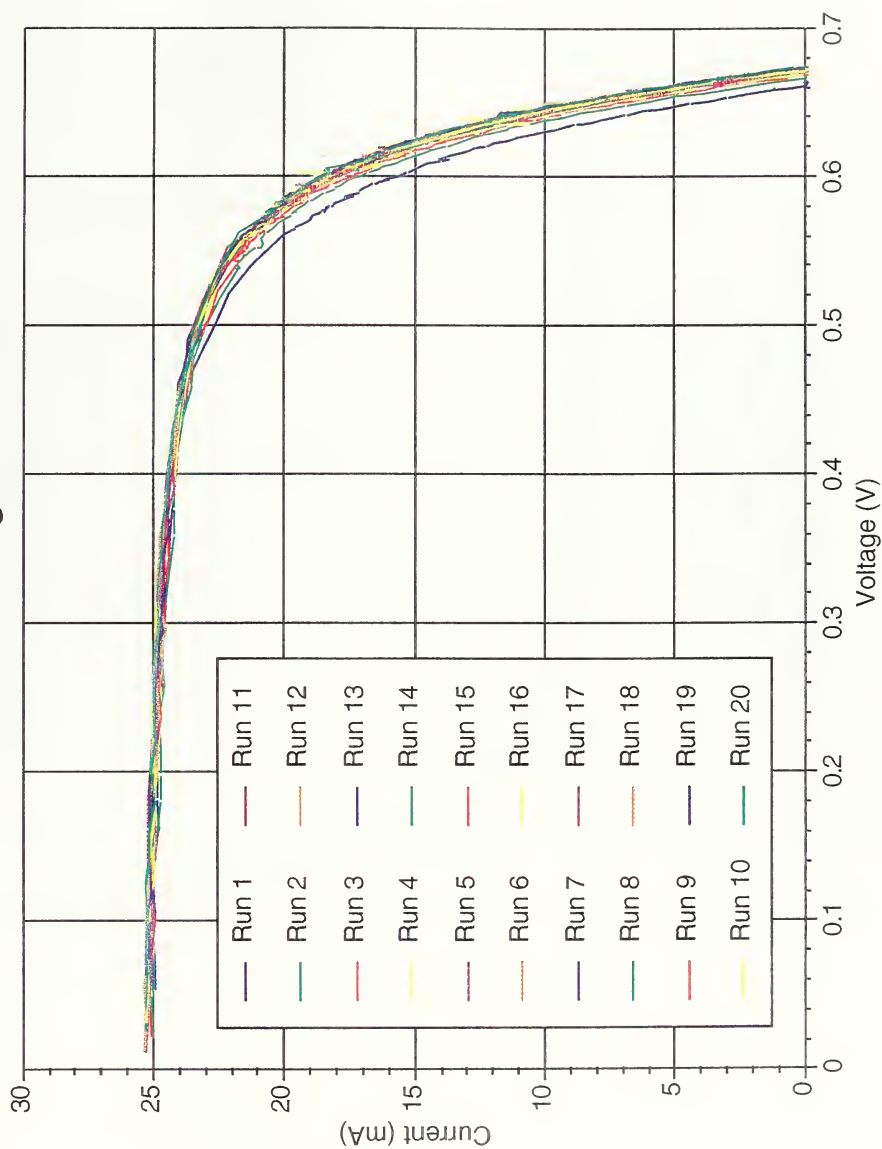
Spire InP/Si np cell #5803-3318-3 Comparison Dark IV's



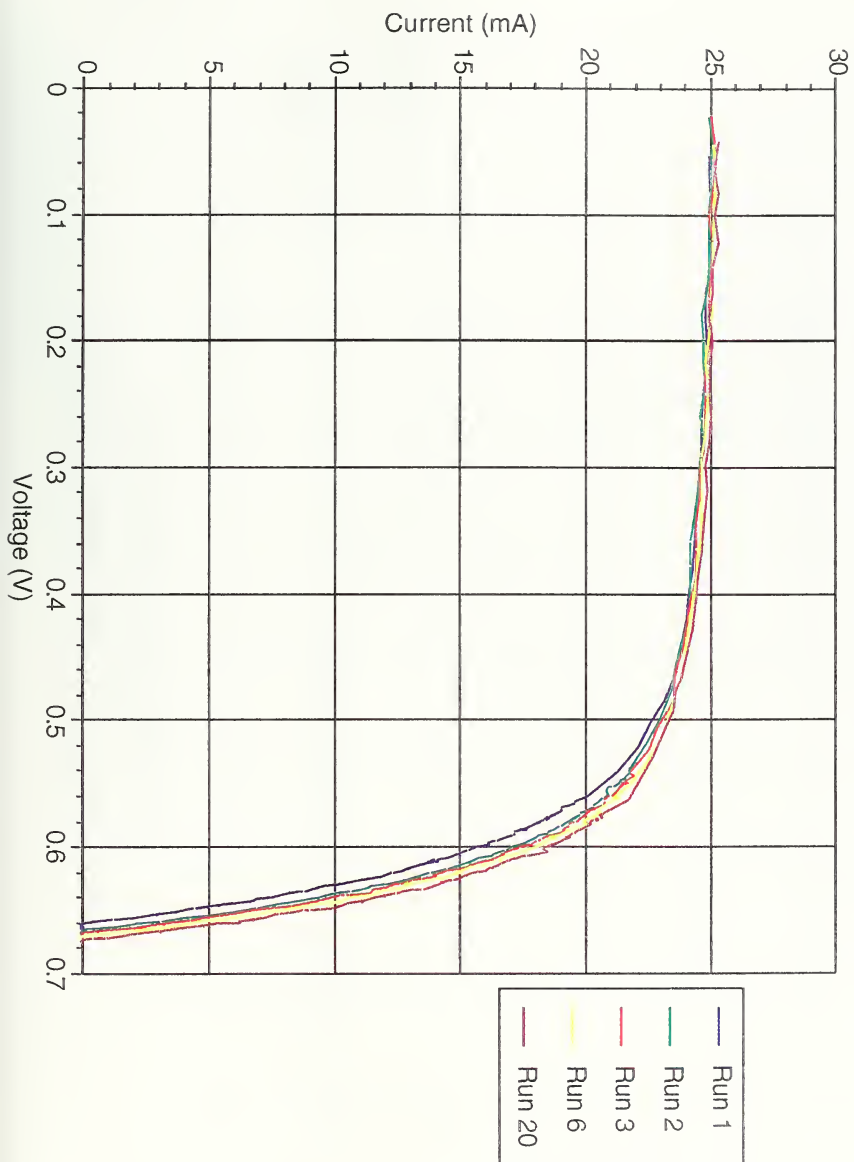
Spire InP/Si np cell #5803-3318-4

Data Run	Isc	Voc	Pmax	Eff	FF
0	26.00	0.71	13.0	9.6%	0.708
1	25.01	0.66	11.5	8.5%	0.695
2	25.08	0.67	11.5	8.7%	0.707
3	25.17	0.67	11.9	8.8%	0.710
4	25.17	0.67	12.0	8.8%	0.710
5	25.19	0.67	12.0	8.9%	0.709
6	25.25	0.67	12.1	8.9%	0.710
7	25.29	0.67	12.0	8.9%	0.710
8	25.29	0.67	12.1	8.9%	0.707
9	25.25	0.67	12.1	8.9%	0.708
15	25.32	0.67	12.1	8.9%	0.709
14	25.31	0.67	12.1	9.0%	0.712
12	25.38	0.67	12.2	9.0%	0.710
13	25.29	0.67	12.2	9.0%	0.710
14	25.31	0.67	12.2	9.0%	0.710
15	25.31	0.67	12.1	8.9%	0.710
15	25.31	0.67	12.1	8.9%	0.710
17	25.32	0.67	12.3	9.1%	0.710
15	25.37	0.67	12.1	9.0%	0.710
19	25.29	0.67	12.1	9.0%	0.713
20	25.29	0.67	12.2	9.0%	0.710
0	26.00	0.71	13.0	9.6%	0.708
Percent Degradation	5.6%	4.9%	11.90%	11.9%	2.1%
Percent Recovery	51%	2%	49%	49%	171%

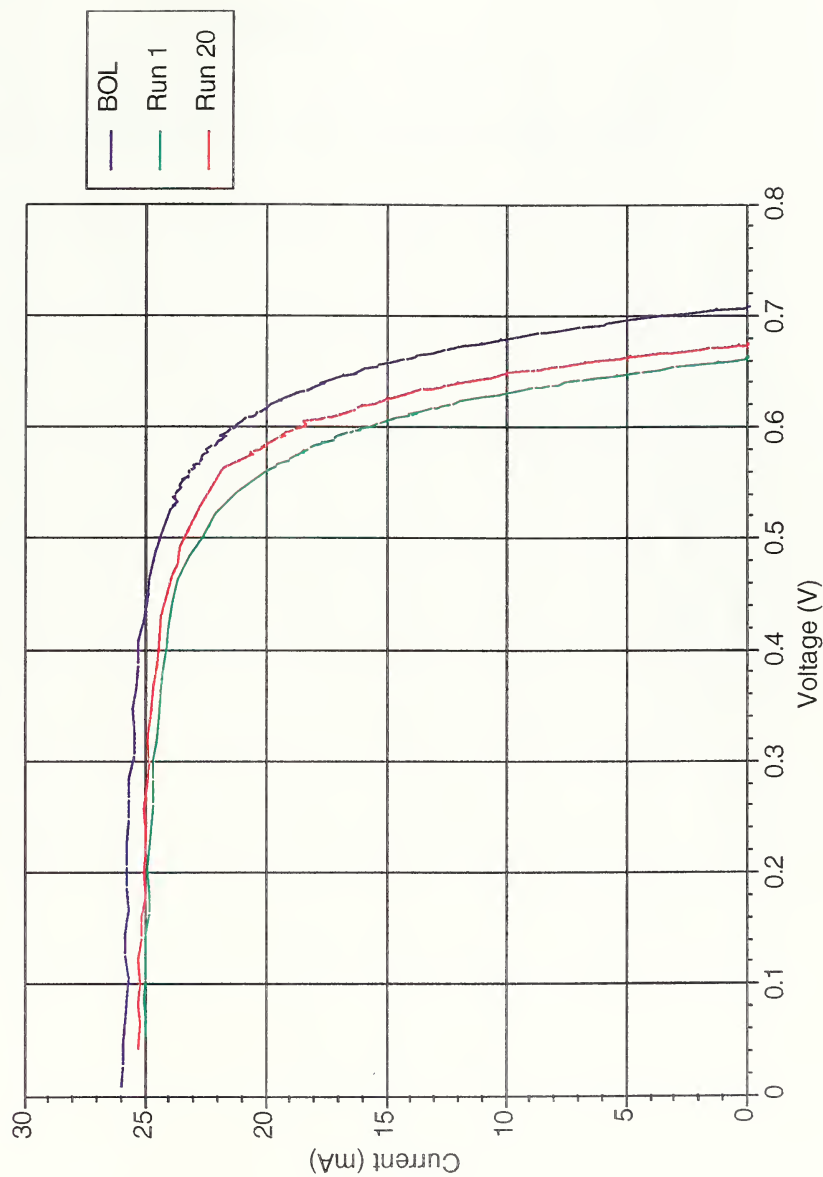
Spire InP/Si np cell #5803-3318-4 Post Laser Light I-V's



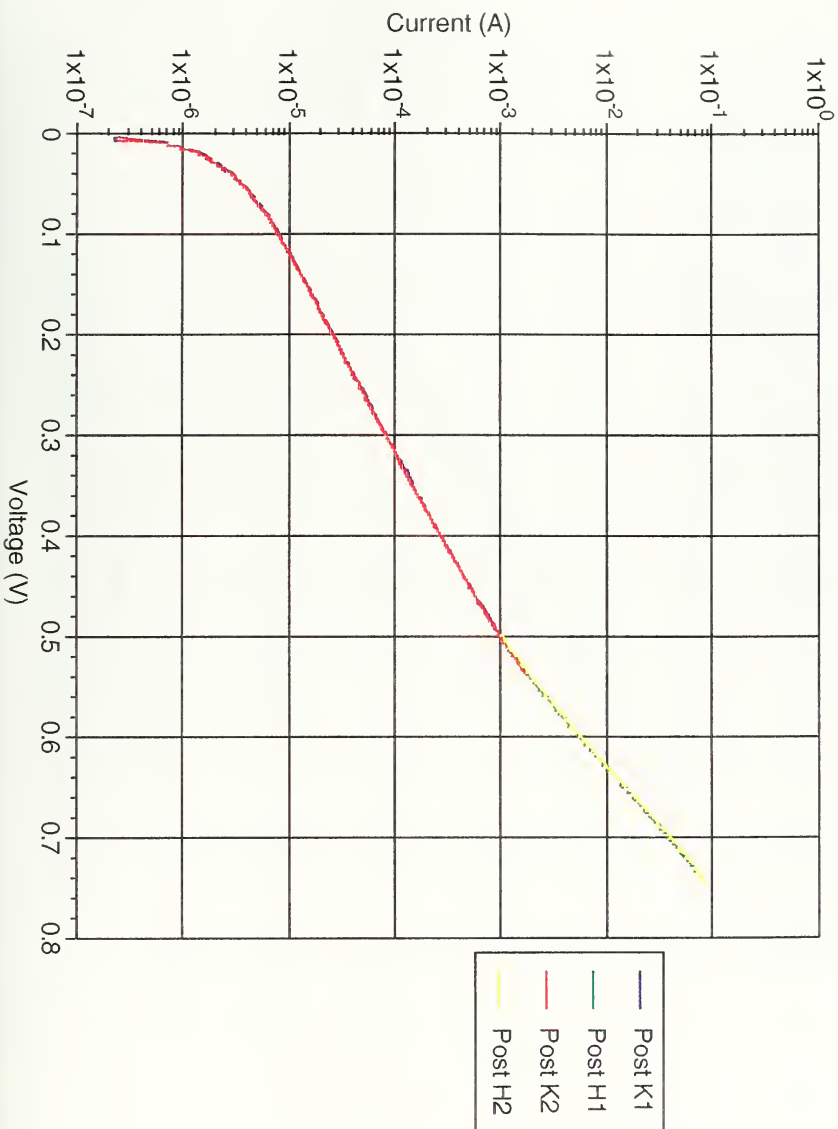
Spire InP/Si np cell #5803-3318-4 Post Laser Light I-V's



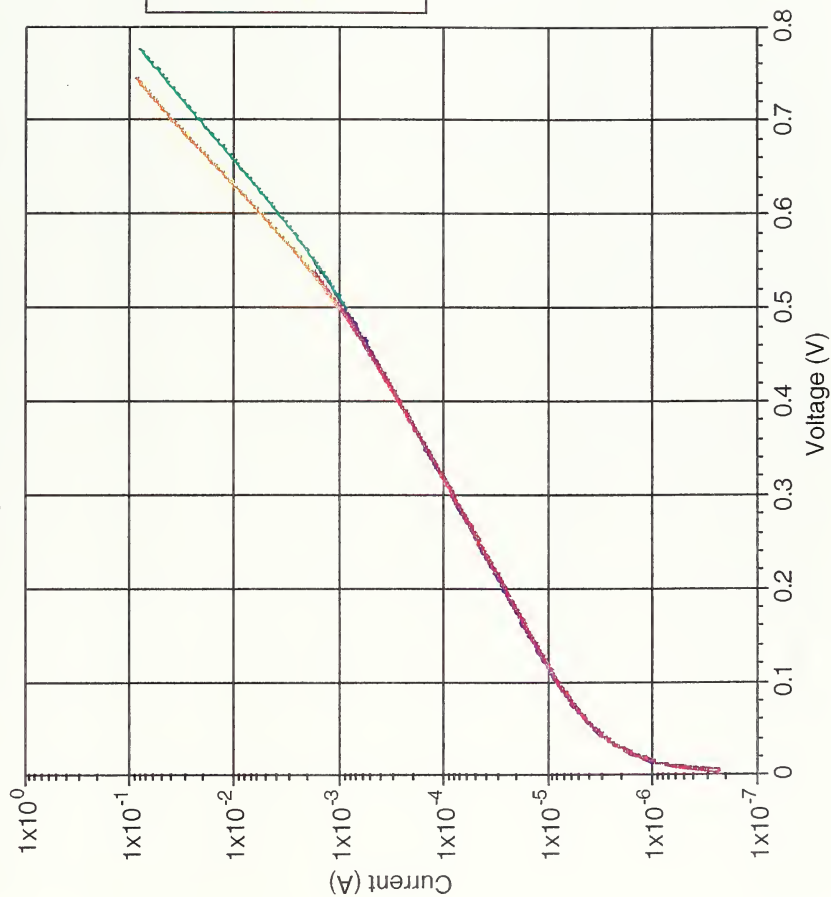
Spire InP/Si np cell #5803-3318-4 Comparison Light I-V's



Spire InP/Si np cell #5803-3318-4 Post Laser Dark IV's



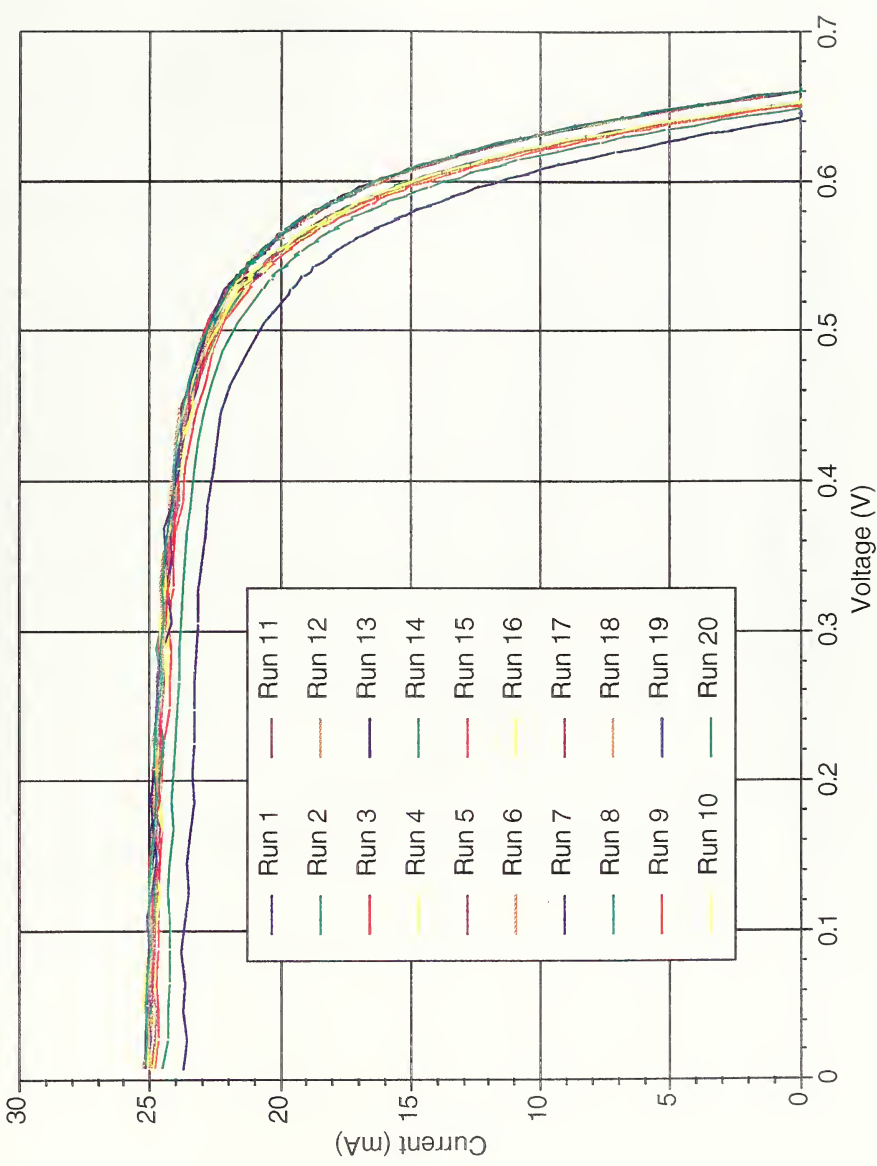
Spire InP/Si np cell #5803-3318-4 Comparison Dark IV's



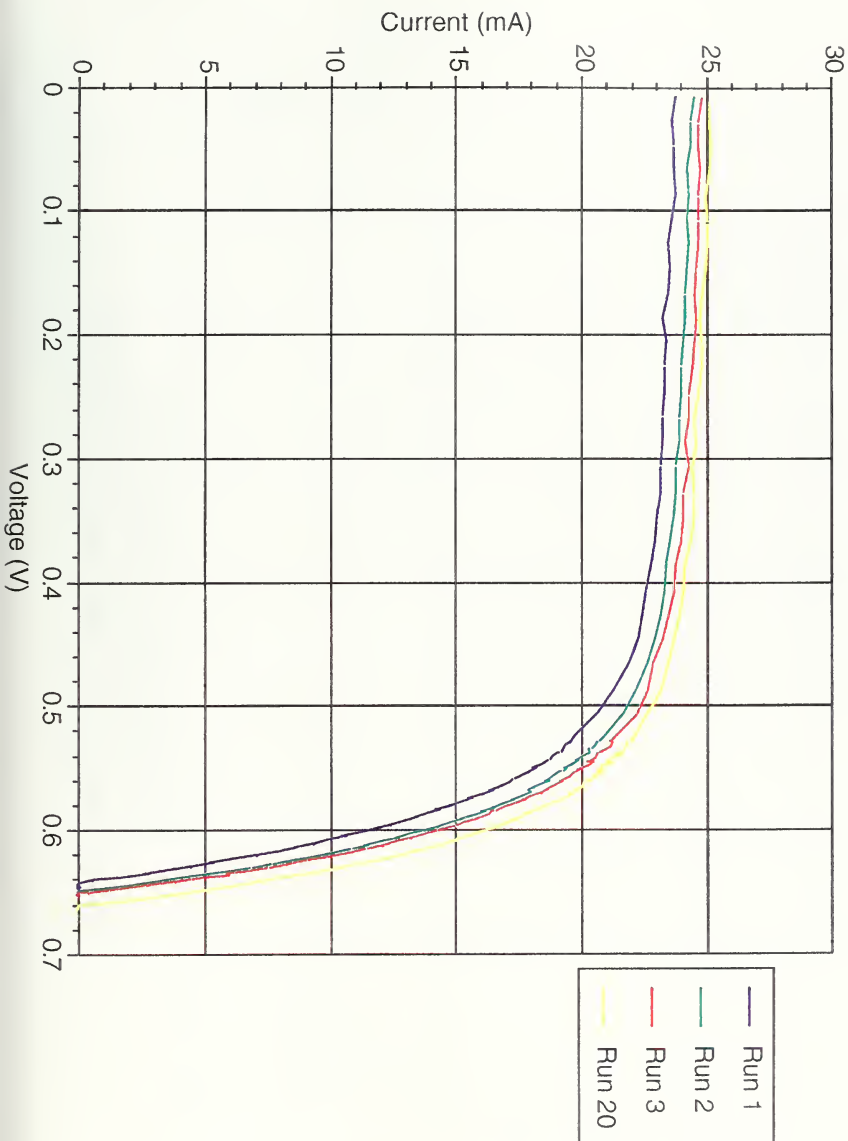
Spire InP/Si np cell #5803-3318-6

Data Run	Isc	Voc	Pmax	Eff	FF
0	25.58	0.69	12.4	9.2%	0.701
1	23.76	0.65	11.4	7.7%	0.696
2	24.39	0.65	10.9	8.1%	0.687
3	24.79	0.65	11.4	8.3%	0.696
4	24.89	0.65	11.3	8.3%	0.696
5	24.92	0.65	11.4	8.4%	0.696
6	25.50	0.65	11.4	8.4%	0.698
7	25.12	0.65	11.4	8.4%	0.694
8	25.50	0.65	11.4	8.5%	0.701
9	25.16	0.65	11.4	8.4%	0.699
10	25.12	0.65	11.4	8.5%	0.697
11	25.20	0.66	11.6	8.6%	0.696
12	25.58	0.66	11.6	8.6%	0.701
13	25.13	0.66	11.6	8.6%	0.701
14	25.13	0.66	11.6	8.6%	0.696
15	25.23	0.66	11.6	8.6%	0.699
16	25.20	0.66	11.6	8.6%	0.697
17	25.04	0.66	11.6	8.6%	0.702
18	25.17	0.66	11.6	8.6%	0.699
19	25.15	0.66	11.4	8.6%	0.702
20	25.15	0.66	11.6	8.6%	0.701
0	25.58	0.69	12.4	9.2%	0.701
Percent Degradation	51%	2%	49%	49%	171%
Percent Recovery	70%	5%	46%	46%	92%

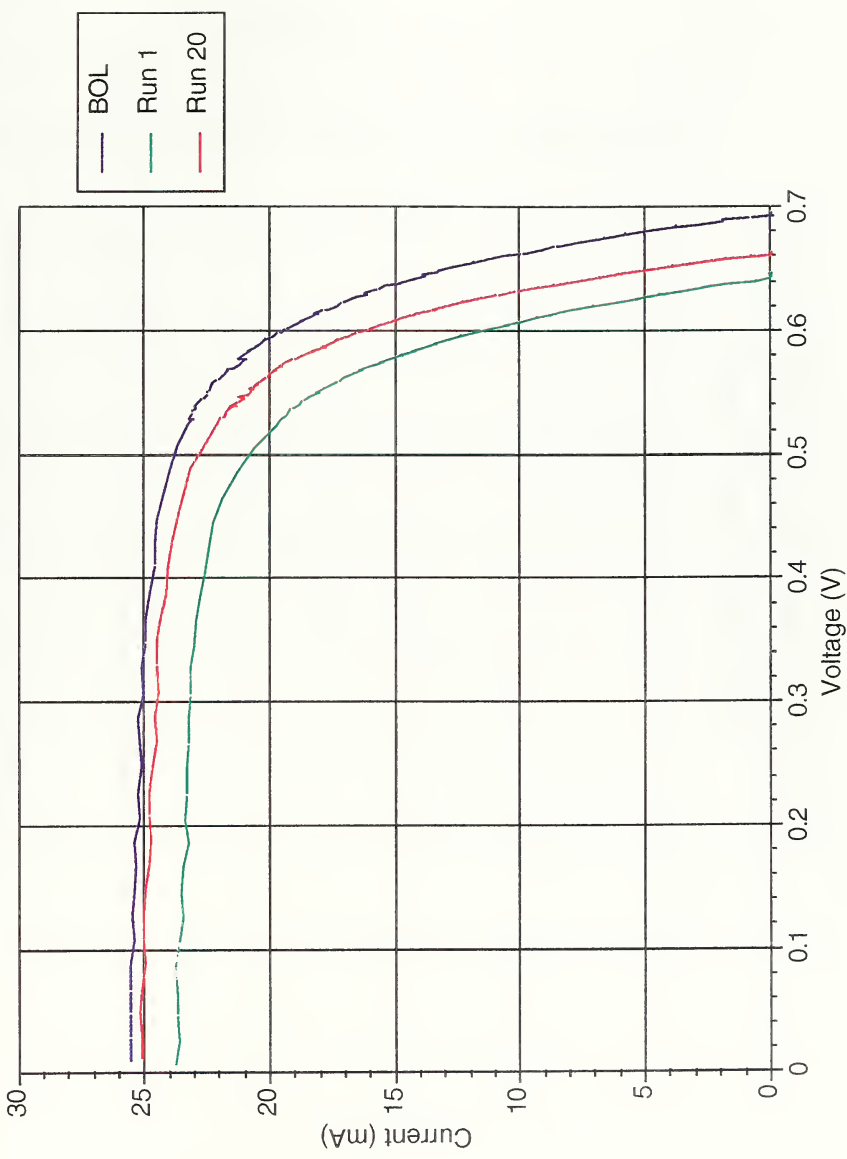
Spire InP/Si np cell #5803-3318-6 Post Laser Light I-V's



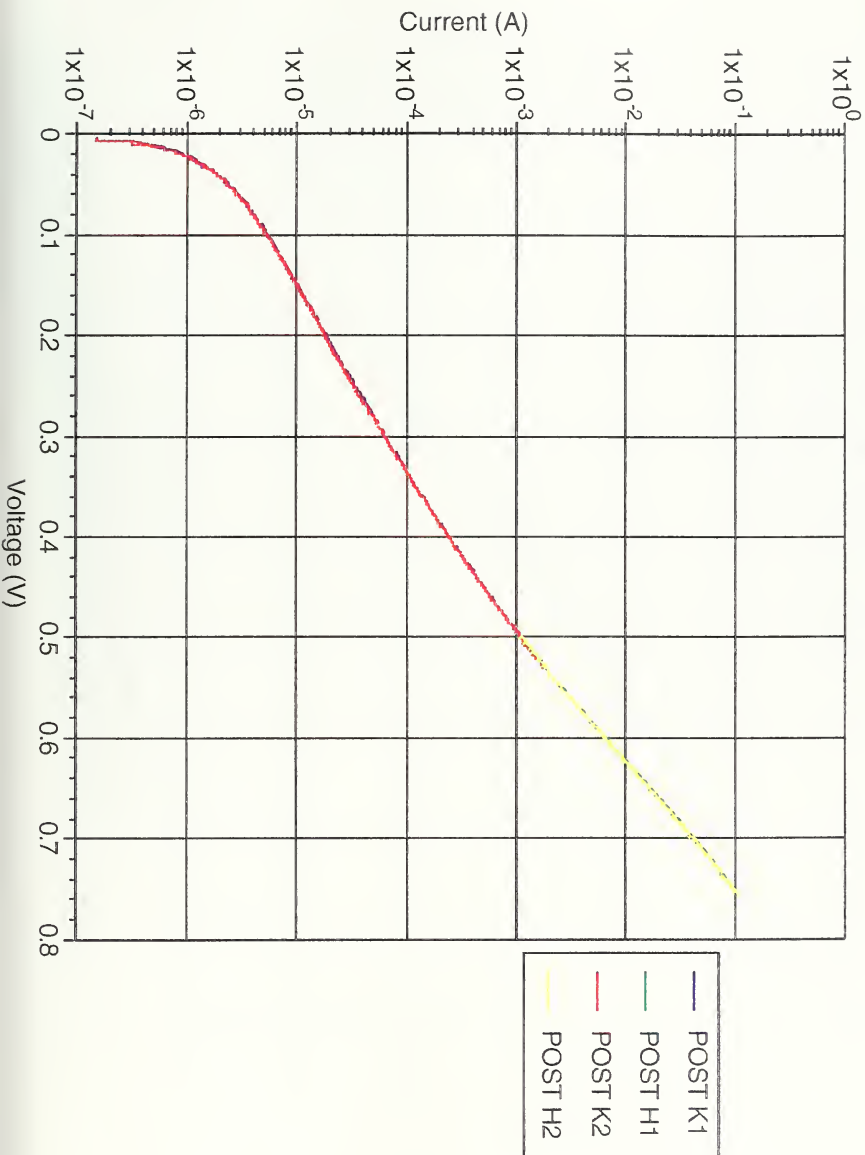
Spire InP/Si np cell #5803-3318-6 Post Laser Light I-V's



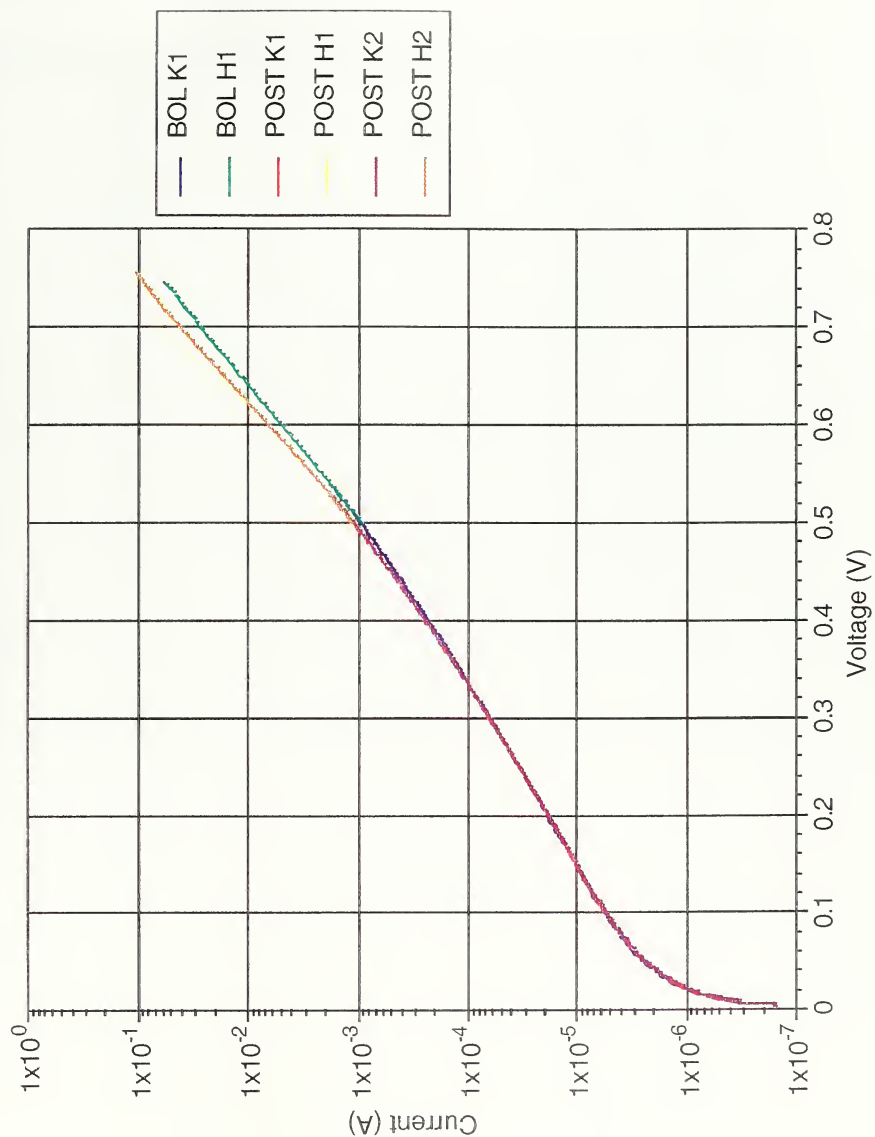
Spire InP/Si np cell #5803-3318-6 Comparison Light I-V's



Spire InP/Si np cell #5803-3318-6 Post Laser Dark IV's



Spire InP/Si np cell #5803-3318-6 Comparison Dark IV's

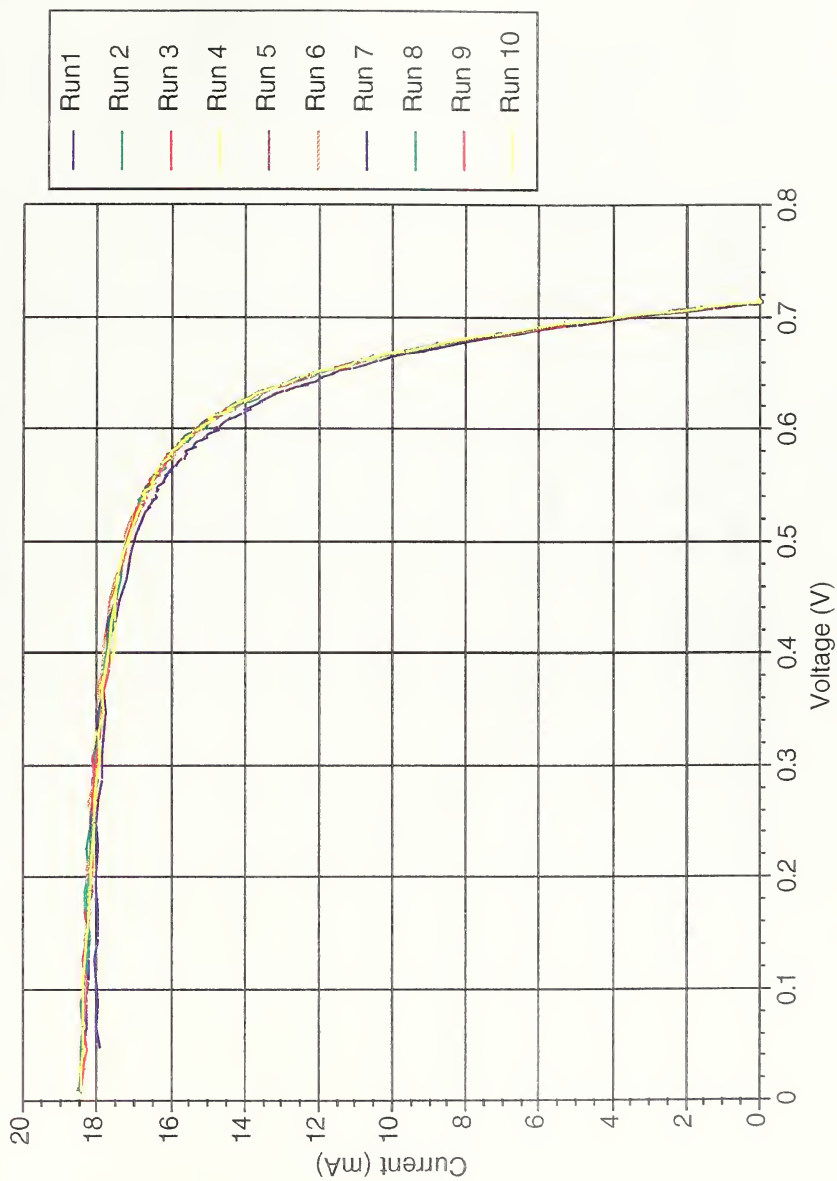


Spire InP/Si pn cell #5803-3324-3

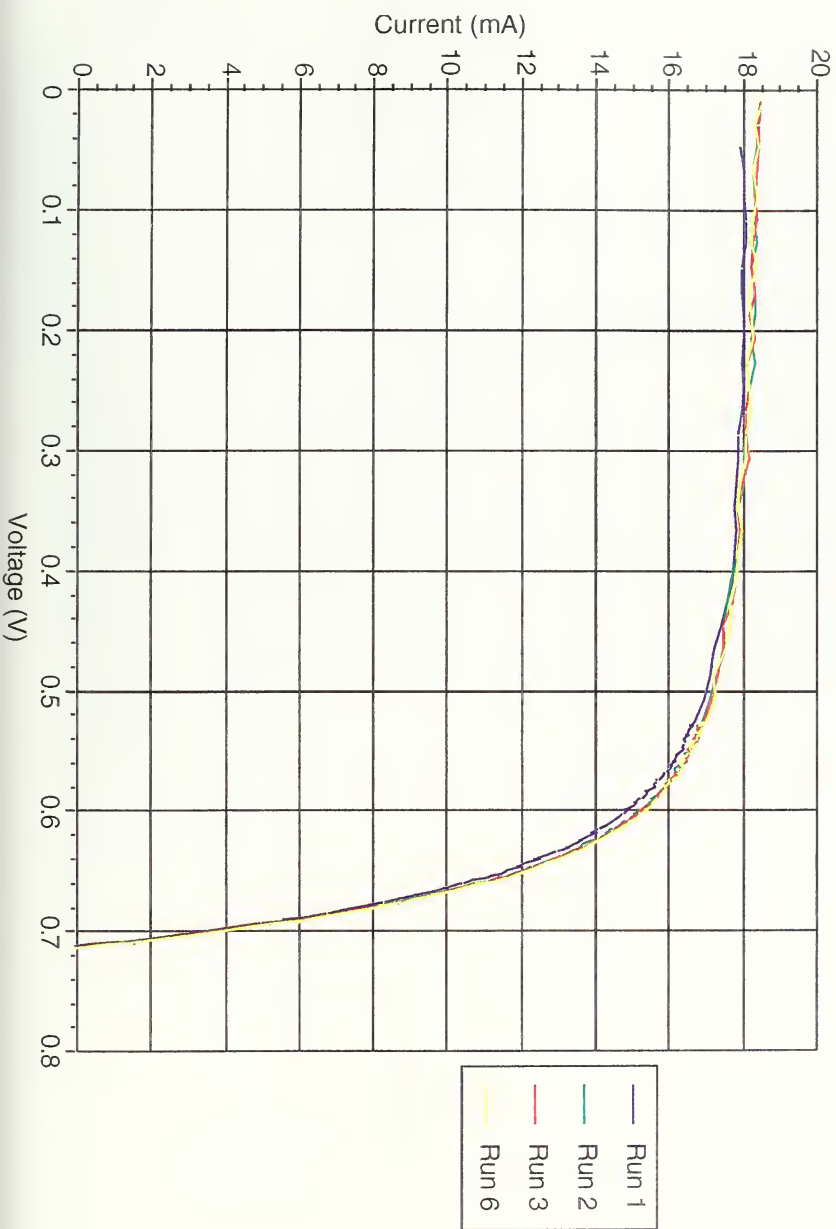
Cell 3	Isc	Voc	Pmax	Eff	FF
0	20.09	0.72	10.4	7.7%	0.716
1	18.08	0.71	9.1	6.7%	0.703
2	18.48	0.71	9.2	6.8%	0.700
3	18.47	0.71	9.3	6.9%	0.703
9	18.47	0.71	9.3	6.8%	0.702
9	18.46	0.71	9.3	6.9%	0.704
6	18.51	0.71	9.3	6.9%	0.702
7	18.00	0.71	9.3	6.9%	0.702
9	18.00	0.71	9.3	6.9%	0.705
9	18.00	0.71	9.3	6.9%	0.707
10	18.42	0.71	9.3	6.9%	0.705
0	20.09	0.72	10.4	7.7%	0.716
Percent Degradation	10.0%	1.3%	12.8%	12.8%	1.9%
Percent Recovery	17%	14%	16%	16%	17%

Spire InP/Si pn cell #5803-3324-3

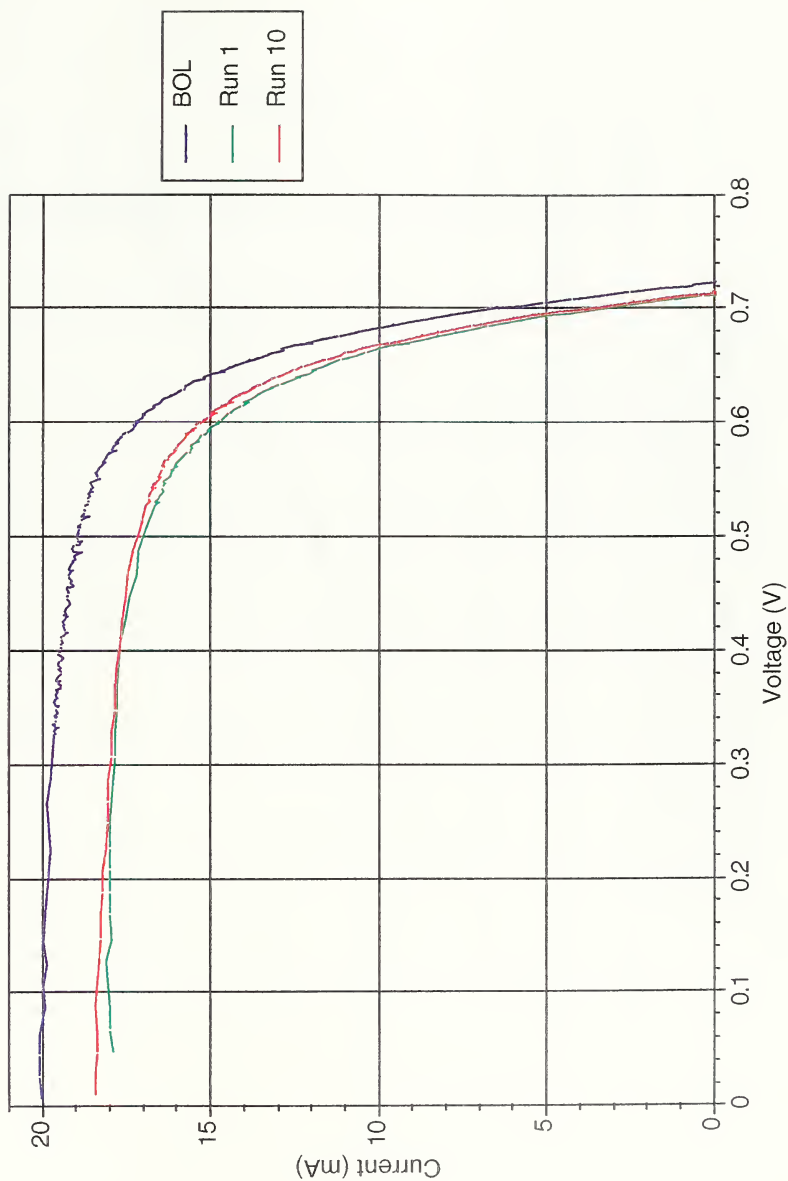
Post Rad S.S. Light I-V's



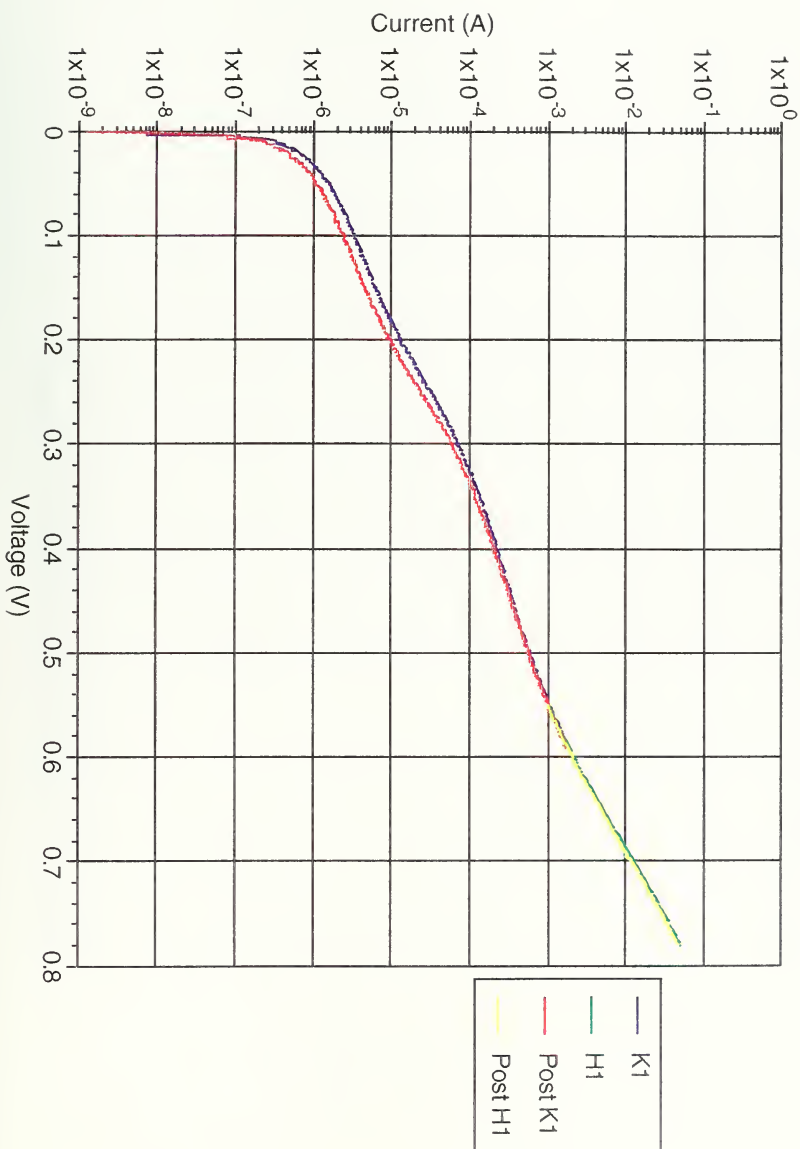
Spire InP/Si pn cell #5803-3324-3 Post Rad S.S. Light I-V's



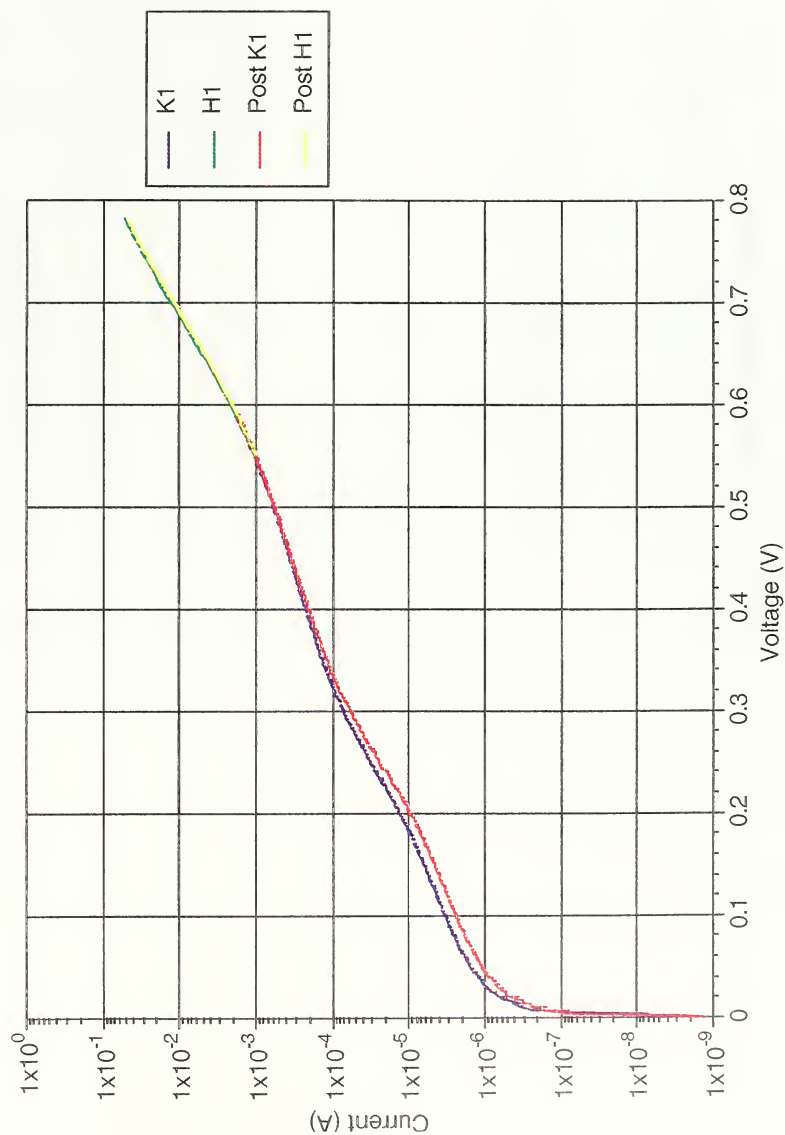
Spire InP/Si pn cell #5803-3324-3 Post Rad S.S. Light IV's



Spire InP/Si pn cell #5803-3324-3 Post Rad S.S. Annealed Dark IV's



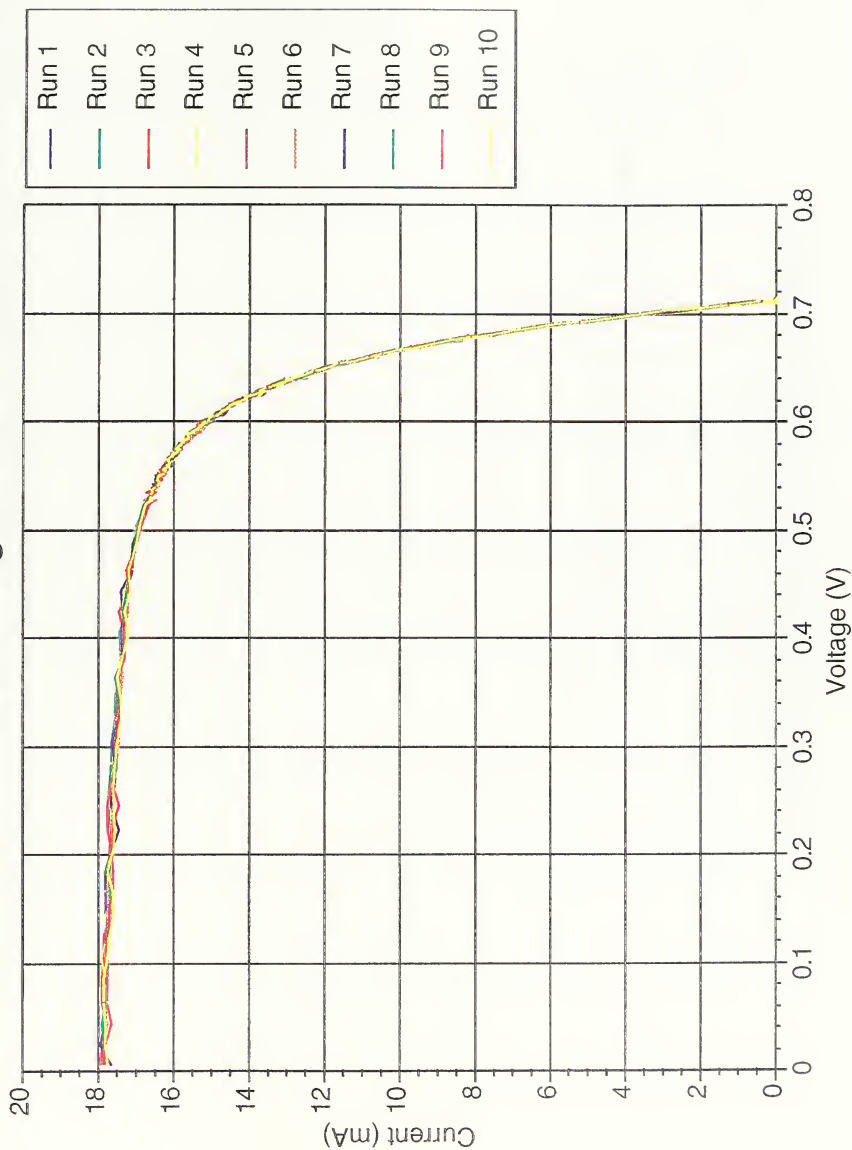
Spire InP/Si pn cell #5803-3324-3 Post Rad-S.S. Annealed Dark IV's



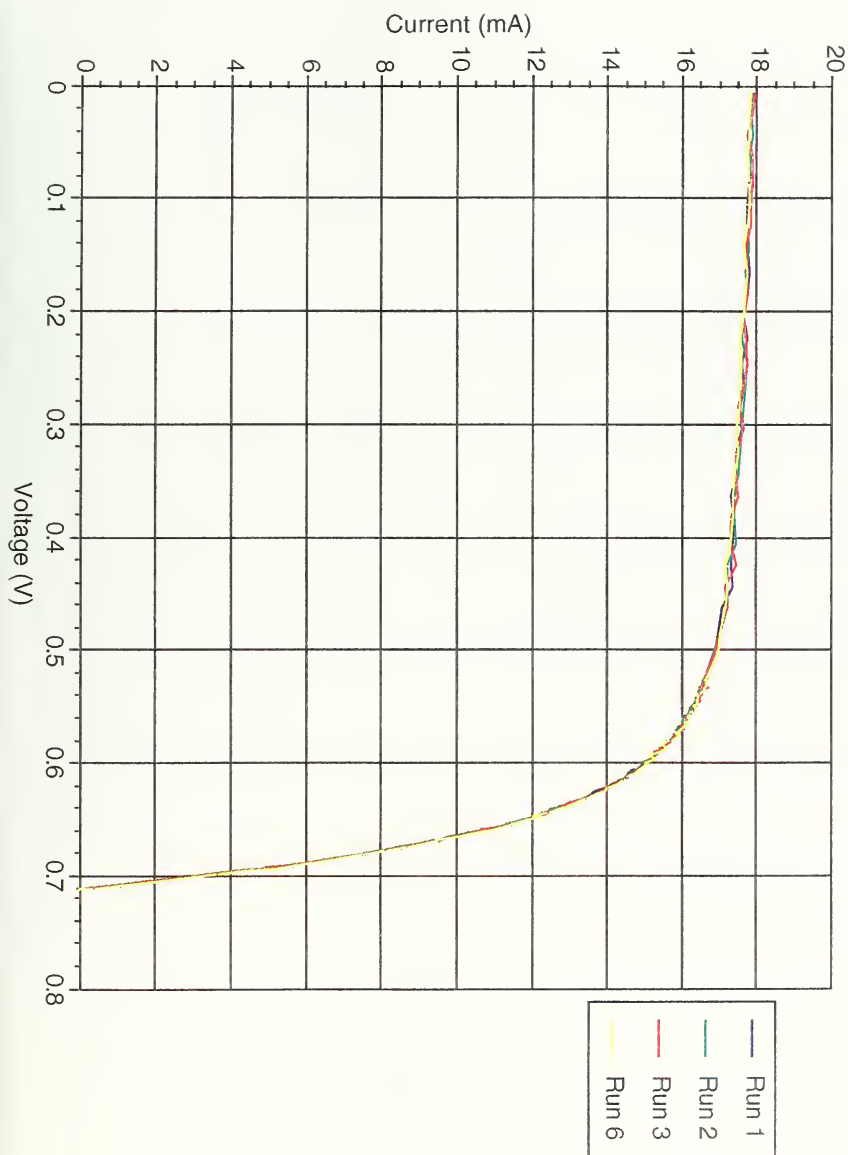
Spire InP/Si pn cell #5803-3324-5

Data Run	Isc	Voc	Pmax	Eff	FF
0	20.05	0.73	10.7	7.9%	0.736
1	17.86	0.71	9.1	6.7%	0.718
2	17.95	0.71	9.2	6.8%	0.720
3	17.95	0.71	9.2	6.8%	0.718
3	17.86	0.71	9.2	6.8%	0.722
5	17.87	0.71	9.2	6.8%	0.718
6	17.82	0.71	9.2	6.8%	0.722
7	17.91	0.71	9.2	6.8%	0.720
8	17.84	0.71	9.2	6.8%	0.723
9	17.84	0.71	9.2	6.8%	0.723
10	17.84	0.71	9.2	6.8%	0.720
0	20.05	0.73	10.7	7.9%	0.736
Percent Degradation	10.0%	1.3%	12.80%	12.8%	1.9%
Percent Recovery	-10%	-51%	-12%	-12%	9%

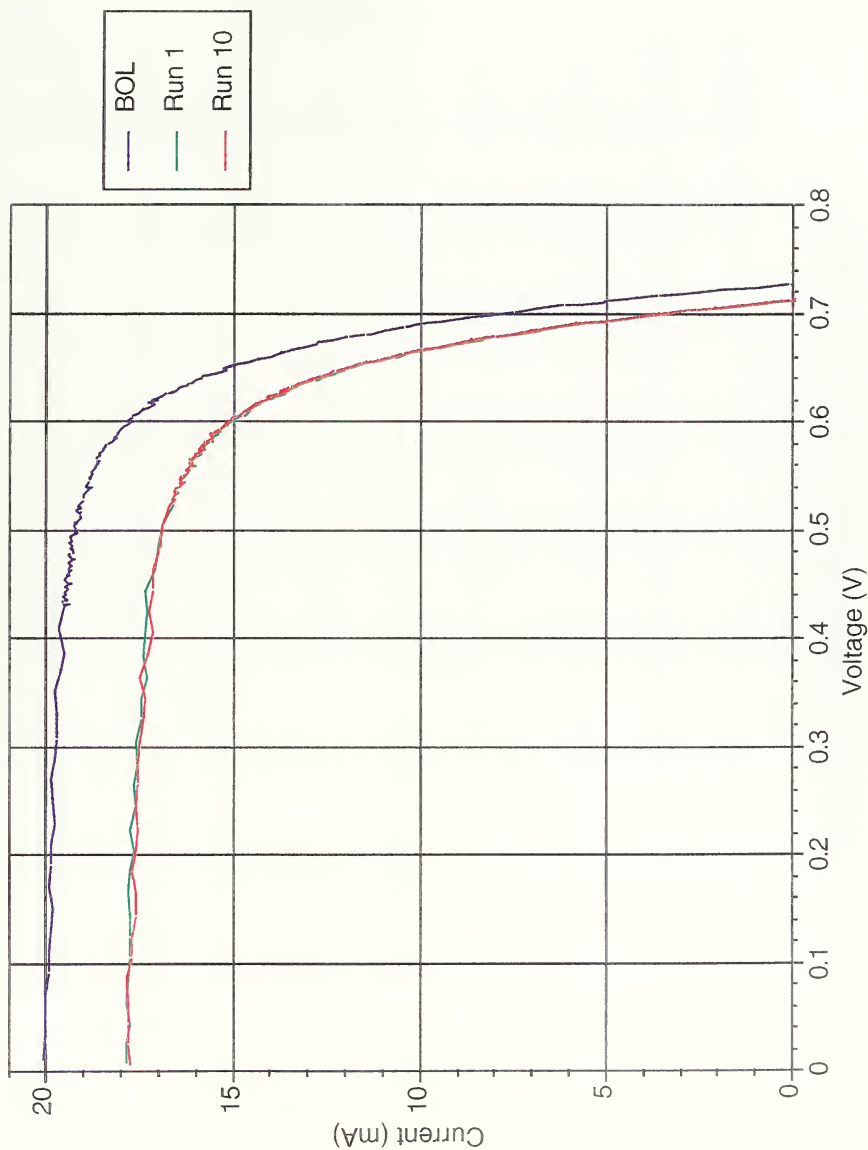
Spire InP/Si pn cell #5803-3324-5 Post Laser Light I-V's



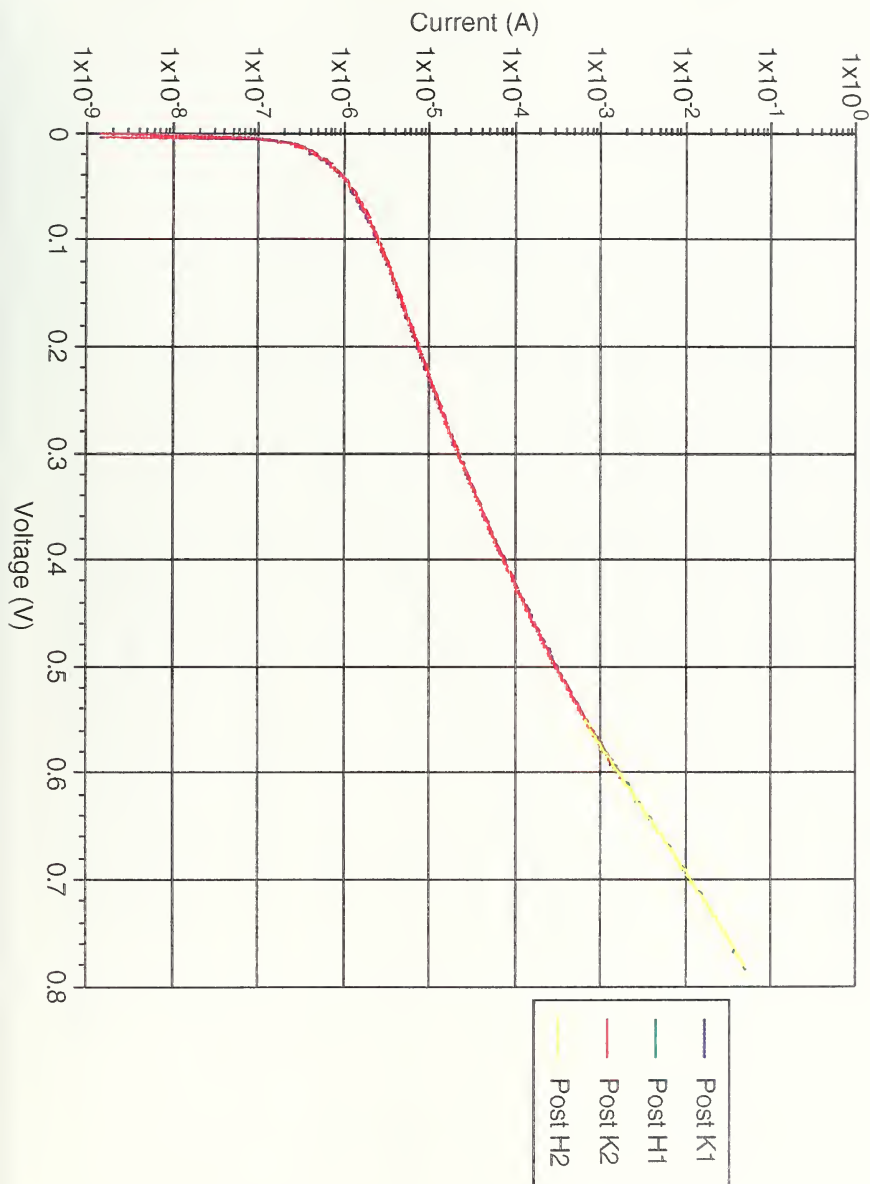
Spire InP/Si pn cell #5803-3324-5 Post Laser Light I-V's



Spire InP/Si pn cell #5803-3324-5 Comparison Light I-V's

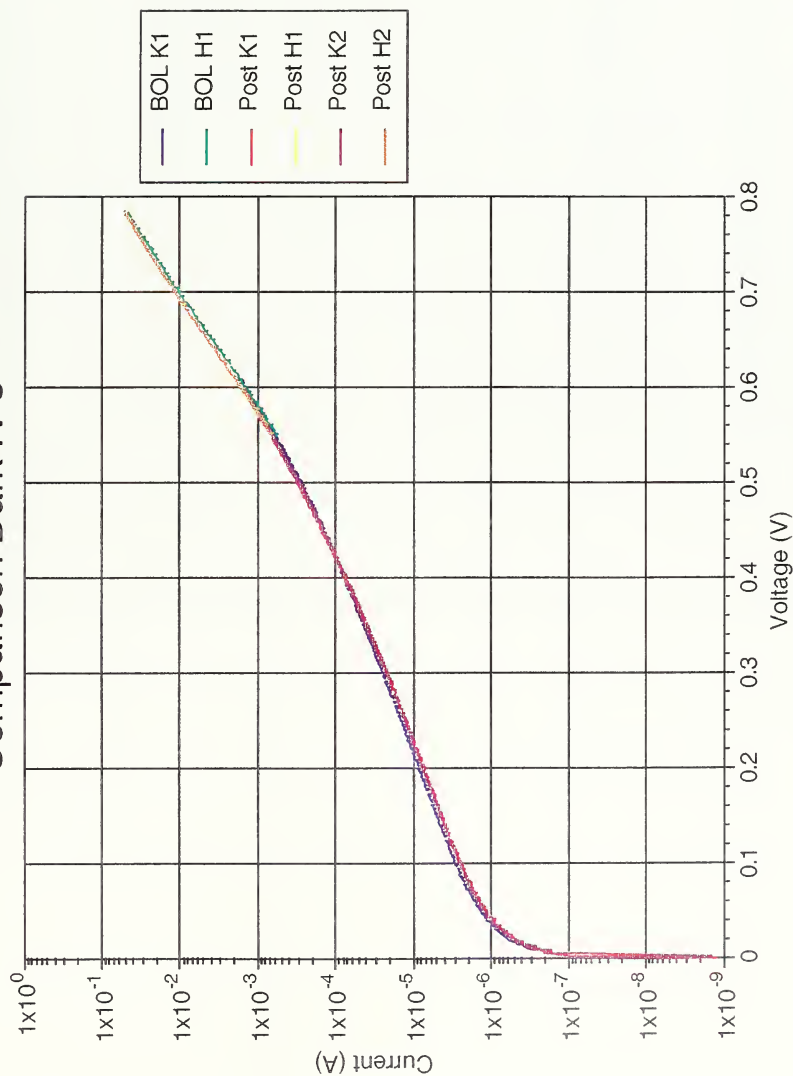


Spire InP/Si pn cell #5803-3324-5 Post Laser Dark IV's



Spire InP/Si pn cell #5803-3324-5

Comparison Dark IV's

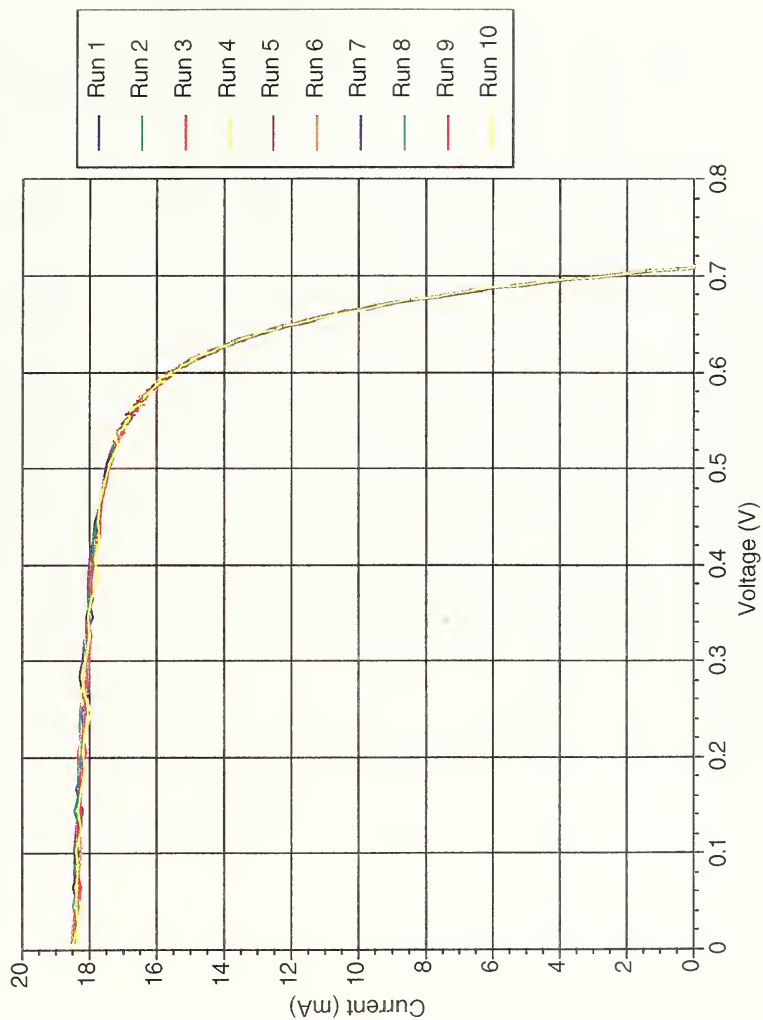


Spire InP/Si pn cell #5803-3324-6

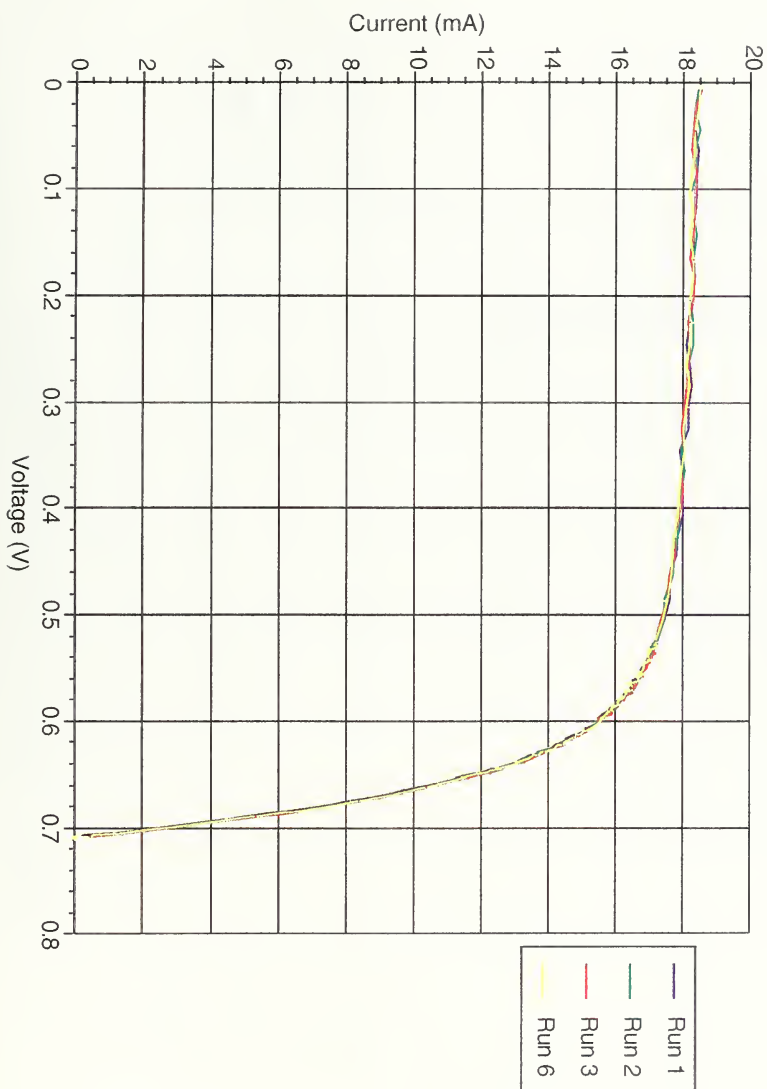
Data Run	Isc	Voc	Pmax	Eff	FF
0	20.70	0.72	10.9	8.0%	0.730
1	18.46	0.71	9.5	7.0%	0.722
2	18.54	0.71	9.5	7.0%	0.721
3	18.55	0.71	9.5	7.0%	0.720
4	18.44	0.71	9.5	7.0%	0.724
5	18.46	0.71	9.5	7.0%	0.721
6	18.54	0.71	9.4	7.0%	0.717
7	18.50	0.71	9.4	7.0%	0.719
8	18.46	0.71	9.5	7.0%	0.722
9	18.44	0.71	9.4	7.0%	0.721
10	18.50	0.71	9.4	7.0%	0.719
0	20.70	0.72	10.9	8.0%	0.730
Assumed Percent Degradation	10.0%	1.3%	12.8%	12.8%	1.9%
Percent Recovery	-6%	-18%	-4%	-4%	20%

Spire InP/Si pn cell #5803-3324-6

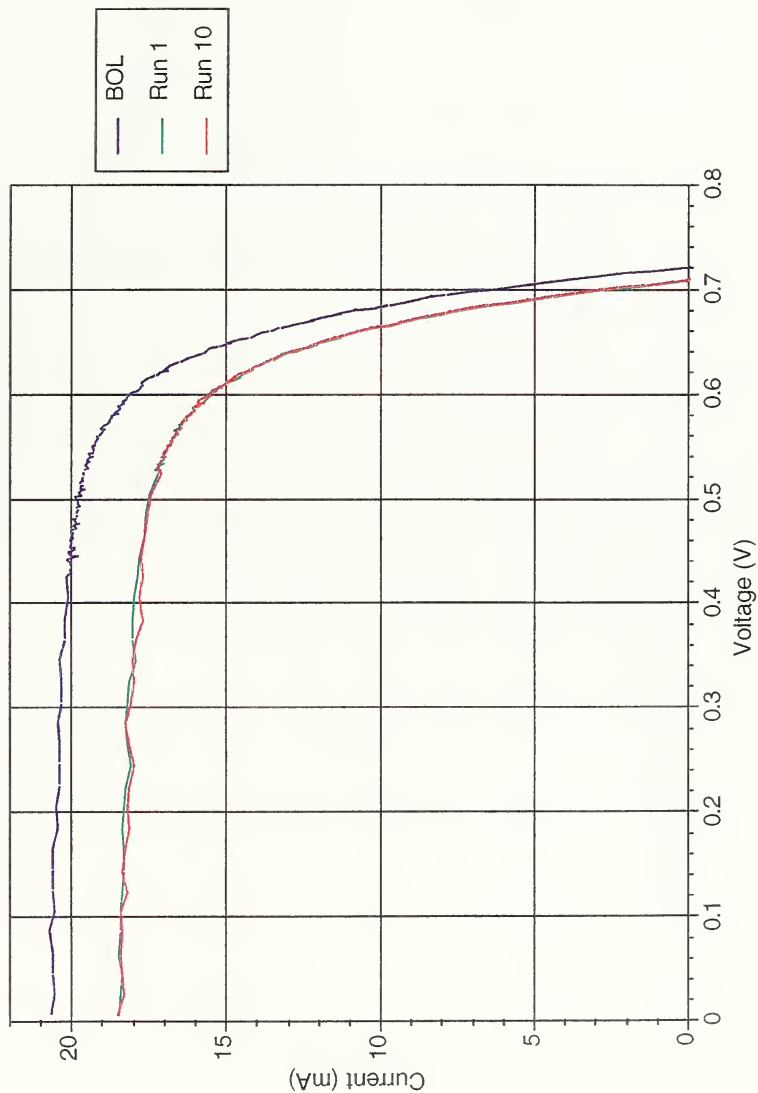
Post Laser Light I-V's



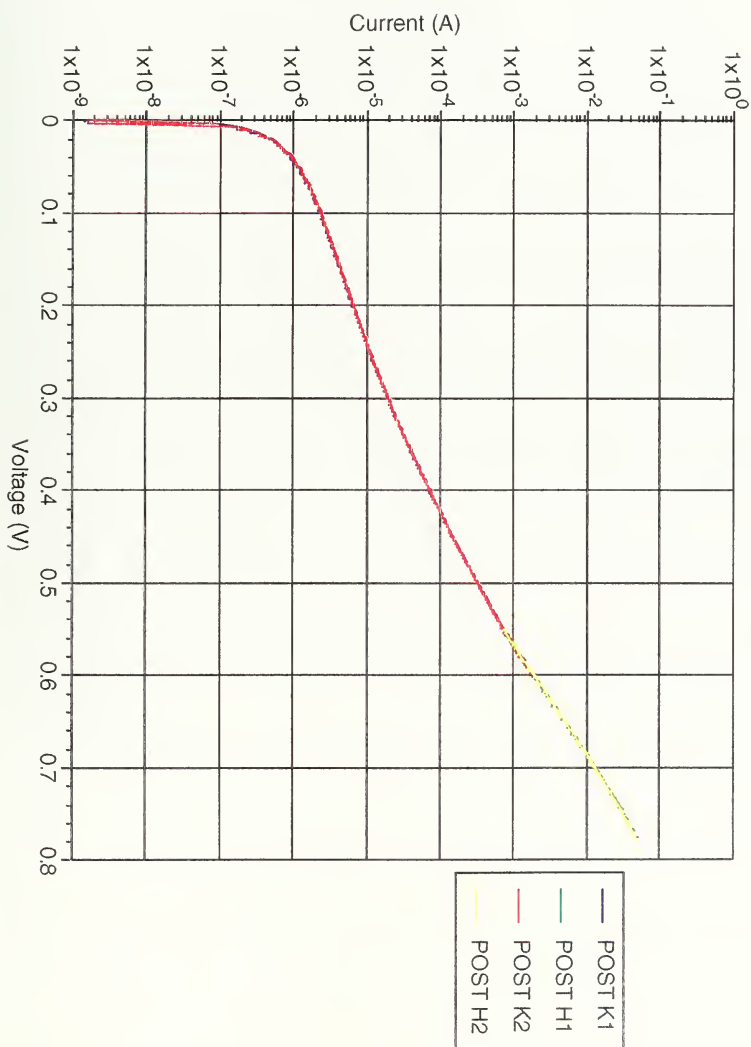
Spire InP/Si pn cell #5803-3324-6 Post Laser Light I-V's



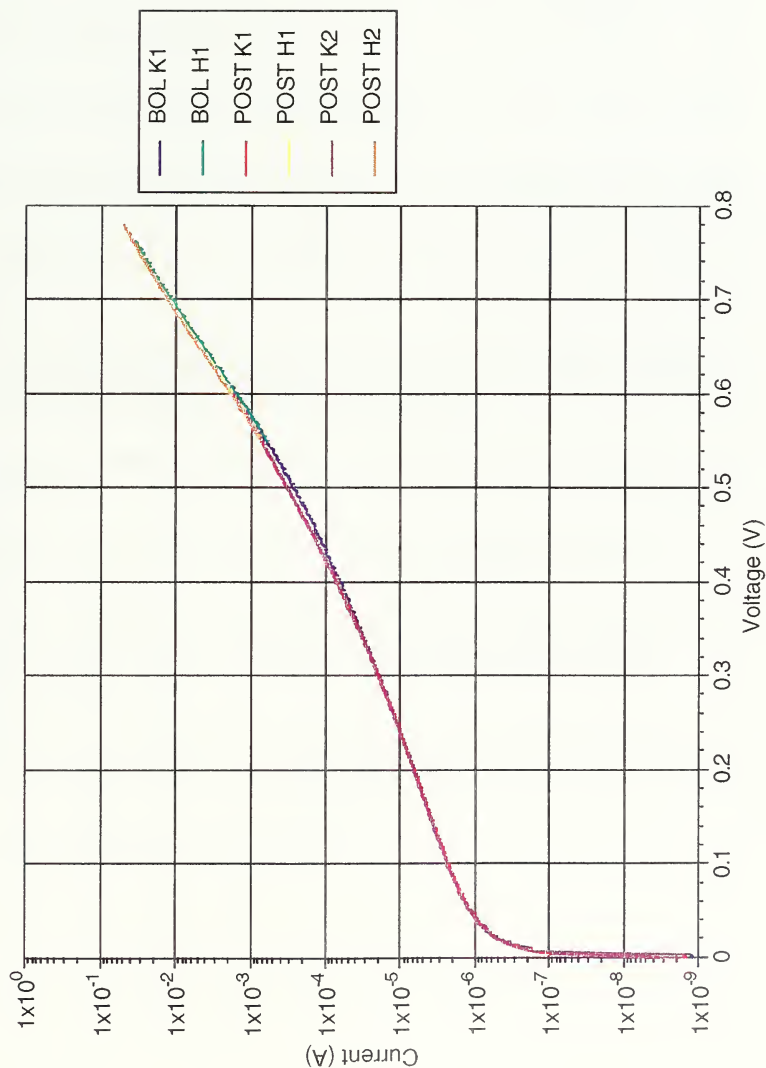
Spire InP/Si pn cell #5803-3324-6 Comparison Light I-V's



Spire InP/Si pn cell #5803-3324-6 Post Laser Dark IV's



Spire InP/Si pn cell #5803-3324-6 Comparison Dark IV's



Combustion Peak 1A
 10/16/21 bu cell #2803-3334-8



LIST OF REFERENCES

1. Wiley J. Larson and James. R. Wertz, *Space Mission Analysis and Design*, Microcosm & Kluwer Academic Publishers, 1992.
2. O. Heinz and R. C. Olsen, *Introduction to the Space Environment*, Naval Postgraduate School Class Notes for PH 2514, 1994 (unpublished).
3. Jet Propulsion Laboratory Publication 82-69, *Solar Cell Radiation Handbook*, Third Edition, by H.Y. Tada, J.R. Carter, Jr., B. E. Anspaugh, R. G. Downing, November 1982.
4. Douglas C. Giancoli, *General Physics*, Prentice-Hall, Englewood Cliffs, New Jersey, 1984.
5. S.J. Wojtczuk, P. Colter, N.H. Karam, G.P. Summers, and R.J. Walters, "Radiation-Hard, Lightweight 12% AM0 BOL InP/Si Solar Cells," *Proc. 25th IEEE Photovoltaic Specialist Conference*, May 13-17, 1996, Washington, DC.
6. Kasturi Lal Chopra and Suhit Ranjan Das, *Thin Film Solar Cells*, Plenum Press, New York, 1983.
7. Martin A. Green, *Solar Cells: Operating Principles, Technology, and Systems Applications*, Prentice Hall, Englewood Cliffs, New Jersey, 1982.
8. C. Chase, "Annealing of Defect Sites in Radiation Damaged Indium Phosphide Solar Cells through Laser Illumination," Master's Thesis, Naval Postgraduate School, Monterey California, 1995.
9. R. Kramer, "Annealing of Radiation Damaged Gallium Arsenide Solar Cells By Laser Illumination," Master's Thesis, Naval Postgraduate School, Monterey California, 1994.
10. Air Force Geophysics Laboratory, *Handbook of Geophysics and the Space Environment*, by Adolph S. Jursa, 1985.
11. Stephen J. Fonash, *Solar Cell Device Physics*, Academic Press, New York, 1981.
12. R. J. Walters, "A Study of the Annealing of Radiation-Induced Defects in InP Solar Cells," Doctorial Dissertation, University of Maryland, Baltimore County, 1994.

13. Thomas J. Pivrotto, *Annealing Radiation Damaged Silicon Solar Cells with a Copper Halide Laser*, Jet Propulsion Laboratory, Pasadena, California.
14. Sherif Michael, *Space Power and Radiation Effects*, Naval Postgraduate School Class Notes for EO 3205, 1994 (unpublished).
15. Frank Larin, *Radiation Effects in Semiconductor Devices*, John Wiley & Sons, Inc., New York, 1968.
16. Sherif Michael, Corinne Cypranowski, and Bruce Anwpaugh, *Forward-Biased Current Annealing Of Radiation Degraded Indium Phosphide And Gallium Arsenide Solar Cells*, Twenty-First IEEE Photovoltaic Specialists Conference, pp. 1178-1183, 1990.
17. H. J. Hovel, *Semiconductors and Semimetals, Volume 11, Solar Cells*, Academic Press, New York, 1975.
18. Thomas F. Clark, "An Experimental Test of Minority Carrier Annealing on Gallium Arsenide Solar Cells Using Forward-Biased Current," Master's Thesis, Naval Postgraduate School, Monterey California, 1986.
19. J. R. Schwank, *Basic Mechanisms of Radiation Effects in the Natural Space Radiation Environment*, IEEE Nuclear and Space Radiation Effects Conference Short Course, July 18, 1994.
20. Corrine Cypranowski, "Power Recovery of Radiation-Damaged Gallium Arsenide and Indium Phosphide Solar Cells," Master's Thesis, Naval Postgraduate School, Monterey California, 1989.
21. Joseph R. Srou and James M. McGarrity, "Radiation Effects on Microelectronics in Space," *Proceeding of the IEEE*, Vol. 76, No. 11, pp. 1443-1469, 1988.
22. E. G. Stassinopoulos and James P. Raymond, "The Space Radiation Environment for Electronics," *Proceeds of the IEEE*, Vol. 76, No. 11, pp. 1423-1441, 1988.
23. R. J. Walters, "DLTS Study of Electron Irradiation Induced Defects in MOCVD Grown n+p InP," Master's Thesis, University of Maryland, Baltimore County, 1994.
24. S. M. Sze, *Physics of Semiconductor Devices*, Second Edition, John Wiley & Sons, Inc., New York, 1981.
25. M. Yamaguchi, C. Uemura, and Akio Yamamoto, "Radiation Damage in InP Single

Crystals and Solar Cells," *Journal of Applied Physics*, 55 (6), 1429, 15 March 1984

26. R. J. Walters, "A Review of Radiation Effects in InP Solar Cells," presented at the Sixth IEEE International Conference on InP and Related Materials, Santa Barbara, CA, March 1994.

27. NATO Team, U.S. Air Force Space Division, NAVSTAR GPS Joint Program Office, *Introduction to NAVSTAR GPS User Equipment*, June 1987.

28. I. Weinberg, C.K. Swartz, R.E. Hart, Jr., and R.L. Statler, *Radiation and Temperature Effects in Gallium Arsenide, Indium Phosphide, and Silicon Solar Cells*, Nineteenth IEEE Photovoltaic Specialists Conference, pp. 548-557, 1987.

29. Geoffrey A. Landis, *Space Power by Ground-Based Laser Illumination*, IEEE AES Systems Magazine, pp. 3-7, November 1991.

INITIAL DISTRIBUTION LIST

	No. Copies
1. Defense Technical Information Center 8725 John J. Kingman Rd., STE 0944 Ft. Belvoir, VA 22060-6218	2
2. Dudley Knox Library Naval Postgraduate School 411 Dyer Rd. Monterey, CA 93943-5101	2
3. Chairman, Code EC Department of Electrical and Computing Engineering Naval Postgraduate School Monterey, CA 93943-5121	1
4. Professor S. Michael, Code EC/Mi Department of Electrical and Computer Engineering Naval Postgraduate School Monterey, CA 93943-5121	4
5. Dr. Robert J. Walters Naval Research Labs Code 6615 4555 Overlook Ave SW Washington D.C. 20375	1
6. LT Lynn L Boyer IV 343 Gumgywamp Rd Groton, CT 06340	1

DUDLEY KNOX LIBRARY
NAVAL POSTGRADUATE SCHOOL
MONTEREY CA 93943-5101

DUDLEY KNOX LIBRARY



3 2768 00323145 7